# Band structure of Heusler Compounds studied by Photoemission and Tunneling Spectroscopy

**Dissertation**
zur Erlangung des Grades

DOKTOR DER NATURWISSENSCHAFTEN

am Fachbereich 08
der Johannes Gutenberg-Universität
in Mainz

**Elena Arbelo Jorge**
geboren in Santa Ursula, Tenerife, Spain

JOHANNES GUTENBERG UNIVERSITÄT MAINZ

Mainz, 2011

"Scientific knowledge is a body of
statements of varying degrees of certainty,
some most uncertain, some nearly sure,
none absolutely certain"

(**R. P. Feynman**)

# Abstract

Heusler compounds are key materials for spintronic applications. They have attracted a lot of interest due to their half-metallic properties predicted by band structure calculations.

The aim of this work is to evaluate experimentally the validity of the predictions of half metallicity by band structure calculations for two specific Heusler compounds, $Co_2FeAl_{0.3}Si_{0.7}$ and $Co_2MnGa$. Two different spectroscopy methods for the analysis of the electronic properties were used: Angular Resolved Ultraviolet Photoemission Spectroscopy (ARUPS) and Tunneling Spectroscopy.

Heusler compounds are prepared as thin films by RF-sputtering in an ultra high vacuum system.

For the characterization of the samples, bulk and surface crystallographic and magnetic properties of $Co_2FeAl_{0.3}Si_{0.7}$ and $Co_2MnGa$ are studied. X-ray and electron diffraction reveal a bulk and surface crossover between two different types of sublattice order (from B2 to $L2_1$) with increasing annealing temperature. X-ray magnetic circular dichroism results show that the magnetic properties in the surface and bulk are identical, although the magnetic moments obtained are 5 % below from the theoretically predicted.

By ARUPS evidence for the validity of the predicted total bulk density of states (DOS) was demonstrated for both Heusler compounds. Additional ARUPS intensity contributions close to the Fermi energy indicates the presence of a specific surface DOS. Moreover, it is demonstrated that the crystallographic order, controlled by annealing, plays an important role on brodening effects of DOS features. Improving order resulted in better defined ARUPS features.

Tunneling magnetoresistance measurements of $Co_2FeAl_{0.3}Si_{0.7}$ and $Co_2MnGa$ based MTJ's result in a $Co_2FeAl_{0.3}Si_{0.7}$ spin polarization of 44 %, which is the highest experimentally obtained value for this compound, although it is lower than the 100 % predicted. For $Co_2MnGa$ no high TMR was achieved.

Unpolarized tunneling spectroscopy reveals contribution of interface states close to the Fermi energy. Additionally magnon excitations due to magnetic impurities at the interface are observed. Such contributions can be the reason of a reduced TMR compared to the theoretical predictions. Nevertheless, for energies close to the Fermi energy and for $Co_2MnGa$, the validity of the band structure calculations is demonstrated with this technique as well.

# Kurzfassung

Heusler-Verbindungen sind wichtige Materialen für Spintronik-Anwendungen. Sie sind wegen ihrer durch Bandstrukturrechnungen vorhergesagten halbmetallischen Eigenschaften von besonderem Interesse.

Ziel dieser Arbeit ist, die Gültigkeit der Vorhersagen der Halbmetallizität durch Bandstrukturrechnungen für zwei spezifische Heusler-Verbindungen, $Co_2FeAl_{0.3}Si_{0.7}$ und $Co_2MnGa$ experimentell zu überprüfen. Für die Analyse der elektronischen Eigenschaften wurden zwei verschiedene Spektroskopie-Methoden verwendet: Winkelaufgelöste UV-Photoelektron-Spektroskopie (ARUPS) und Tunnelspektroskopie.

Die Heusler-Verbindungen werden durch RF-Sputterdeposition als dünne Filme prepariert. Für Tunnelspectroskopie werden magnetische Tunnelkontakte hergestellt.

Um die Spektroskopie-Ergebnisse interpretieren zu können, werden die kristallographischen und magnetischen Eigenschaften von Volumen und Oberfläche der Filme untersucht. Röntgenbeugung und Elektronenbeugung zeigen eine Übergang zwischen zwei Arten von Untergitterordnung (von B2 nach $L2_1$) im Filmvolumen und an der Oberflächen mit zunehmender Temper-Temperatur. Messungen des Röntgen-magnetischen-zirkular-Dikroismus Ergebnisse zeigen, dass die magnetischen Eigenschaften an der Oberfläche und im Volumen identisch sind. Allerdings sind die ermittelten magnetischen Momente um 5 % kleiner als die theoretisch vorhersagen.

Mit ARUPS wird die Gültigkeit der vorhersagten Volumen-Zustandsdichte für beide Heusler-Verbindungen demonstriert. Zusätzliche ARUPS Intensität in der Nähe der Fermi-Energie zeigt das Vorhandensein einer speziellen Oberflächen-Zustandsdichten (DOS) an. Darüber hinaus wird demonstriert, dass die kristallographische Ordnung, die durch Tempern kontrolliert wird, eine wichtige Rolle für Verbreitungseffekte in der Zustandsdichte spielt. Eine Verbesserung der Ordnung ergibt schmaleren Strukturen in der Zustandsdichte.

Tunnelmagnetowiderstands-Messungen an den Kontakten zeigen für $Co_2FeAl_{0.3}Si_{0.7}$ eine Spinpolarisation von 44 %, den höchsten experimentellen Wert für diese Verbindung, obwohl deutlich niedriger als die theoretisch vorhergesagen 100 %. Für $Co_2MnGa$ wird kein hoher TMR erreicht.

Unpolarisierte Tunnelspektroskopie zeigt eine spezielle Grenzfläche-Zustandsdichte in der Nähe der Fermi-Energie. Zusätzlich wurde Beiträge von Magnon-Anregungen aufgrund von magnetische Verunreinigungen an der Grenzfläche beobachten. Solche Beiträge können der Grund für einen verminderten TMR im Vergleich zu den theoretischen Vorhersagen sein. Trotzdem wird die Gültigkeit der Bandstrukturrechnungen in der Nähe der Fermi-Energie für $Co_2MnGa$ auch mit dieser Technik demonstriert.

# Contents

# List of Figures

# Chapter 1

# Introduction

Modern magnetic materials are suitable for advanced developments in different fields of technology, such as automotive industry, aeronautics, robotics, medicine, information technology, etc.

The microscopic origin of the static and dynamic magnetic properties, which make these materials interesting for applications is based on the physics of the electron spin. In this sense, magnetism can be described as a phenomenon which involves spin-dependent interactions between Fermions in a many-electron system provided by exchange and spin-orbit coupling.

With the discovery of the Giant Magneto-Resistance (GMR) effect in 1988 by Albert Fert [1] and Peter Grünberg [2], awarded with the Nobel Prize in Physics in 2007, a new research area based on spin-dependent transport phenomena arose, which combined magnetism with microelectronics: spintronics. Although previously ferromagnet/superconductor tunneling experiments were pioneered by Meservey and Tedrow [3], and initial experiments on magnetic tunneling junctions (MTJ) were performed by Jullière [4] in the 1970s already, it was the GMR effect which awoke a strong interest of the scientific community in this topic.

The GMR effect was observed in thin film structures composed by alternating ferromagnetic and non-magnetic layers. A big change in the resistance depending on the relative magnetic orientation of the adjacent ferromagnetic layers, whether parallel (low resistance) or antiparallel (high resistance) alignment is observed. This effect brought about not only a revolution in the hard disk industry, but

also stimulated new and different fields of research with the aim of understanding the phenomenon, as well as investigating a wide field of magnetic materials that could be suitable for applications in spintronic devices like spin valves [5] for read-head sensors for hard disk drives or magnetic tunneling junctions [18, 19], based on the tunneling magnetoresistance effect (TMR), for Magnetic Random Access Memory (MRAM) [8, 9, 10], both useful for information storage.

TMR is an important spin transport effect between two ferromagnetic layers (electrodes) separated by an insulated barrier which describes the magnetoresistance effect, due to the current flow through the tunneling barrier, which depends strongly on the relative orientation of magnetization of the electrodes and can be changed by an applied magnetic field.

Highly spin polarized ferromagnets, such as dilute magnetic semiconductors (DMS) [11] and half metallic ferromagnets (HMF) [12], are key materials for these technological developments.

DMS are non-magnetic semiconductors, which have been doped with transition metal atoms carrying a high atomic magnetic moment. Its origin of ferromagnetism is explained by the Zener exchange mechanisms and is directly related to the density of the charge carriers. Moreover, their semiconductivity is related to small band gaps which allows interactions with photons (optically induced magnetism). The multifunctional properties make these materials interesting for spintronic devices. They are particularly attractive for spin injection due to the fact that there is no huge conductivity mismatch at the interface between two layers of semiconductor and ferromagnetic material. Nevertheless, many of them have the disadvantage of presenting low Curie temperatures what makes them not suitable for room temperature applications.

HMF are metals with an unusual band structure. At the Fermi energy they have a band gap for one spin band and are metallic for the other, characterizing them by 100% spin polarization. Four types of HMF's have been theoretically predicted: oxide compounds, perovskites, zinc-blende compounds and Heusler alloys [12]. In particular, many Heusler alloys have been considered as potential candidates for showing half metallic properties with a high Curie temperature clearly above room temperature and a relative large band gap at the Fermi e-

nergy [13, 14, 15]. They are materials with the composition $X_2YZ$ and a $L2_1$ crystallographic structure.

In the researching field of finding good half metallic materials and understanding their properties, two main areas have to be considered:

On one hand, there are theoretical calculations and predictions. The advantages of this computational approach are: no samples are needed, non existing materials can be investigated and new materials can be designed. Also new theoretical models are developed and already existing materials can be understood better. Theory is also attempting to predict how stable materials are and what is the chance of realizing them experimentally.

However, the validity of the theoretical predictions is limited. 100 % spin polarization for half metallic ferromagnets is theoretically predicted by first principles calculations in the ideal case where the temperature is T= 0 K and spin-orbital interactions are neglected. In the case of materials like Heusler alloys, where the Curie temperature is quite above room temperature, these assumptions are justified at low temperatures and minor spin-orbit interactions. However, in a more realistic situation, where the material is at room temperature, a direct comparison is no longer reliable. In this case temperature effects should be considered. Furthermore, most of the calculations are based on Density Functional Theory (DFT) in the Local Density (LDA) or Generalized Gradient Approximation (GGA) and it has been demonstrated that these methods underestimate the band gap [16]. The LDA+U approach claims to repair this shortcoming. However, the prediction of U from first principles is still challenging.

On the other hand, there are experimental studies. Unfortunately, there are no direct measurements which demonstrate or prove half metallicity. However, different experimental techniques have been used in order to indirectly prove this special property. The most direct experiment performed by Hanssen et al. in 1986 is called spin-resolved positron annihilation [17] but it resulted in a tedious and expensive method. Also other experiments have been realized: experiments that indirectly measure the spin polarization like magnetic tunneling junctions [18, 19] or point contact Andreev reflection [20, 21]; and experiments that measure the electron energy spectrum like scanning tunneling spectroscopy [22], spin

polarized photoemission [23, 24, 25] and spin polarized inverse photoemission [26]. In the next chapter all these methods will be discussed more in detail. A common characteristic of all these techniques is that the intrinsic half metallicity of a specific compound is not directly measured but the flair of picking up 100 % polarized electrons from a half metallic ferromagnet. In this process electrons cross a surface or interface into some medium where their degree of spin polarization is analysed. As a consequence, now the properties of surfaces and interfaces also play an important role in the spin polarized electrons transport and thus in the measured spin polarization and electron energy spectrum. Hence the significance in experimental work that very high quality materials, where surface properties are as important as bulk, can be produced. Therefore, optimizing growing processes and characterizing samples are of great importance to help to understand the results and limitations. In general, there are many effects that contribute to a reduction of the measured spin polarization and considerable modifications on the electron energy spectrum: the effect of finite temperatures on the electronic, magnonic and phononic states at the interface, the quality of the interface, disorder and defects.

Improved theoretical methods, which include all these contributions and the development of new models to understand better how the half metallic behaviour of different materials is affected by the above mentioned effects, are relevant to interpret better the experimental results. There are theoretical studies about the electronic band structure that analyse separately the influence of different kind of contributions like temperature effects, disorder, doping [27], electron-magnon interactions [28], and surface/interface effects [29, 30, 31] for different Heusler compounds. It has to be remarked that one important difficulty of theoretical predictions remains in the fact that all these contributions affect every Heusler compound in a different way. No general theory can be applied.

Although direct experimental evidence of half metallicity remains challenging and theoretical calculations have to be improved, a combination between experimental studies and theoretical models is nowadays the most powerful tool to investigate half metallic ferromagnets as relevant materials for spintronic devices.

The aim of this work is to evaluate the validity of predictions of half metallicity by band structure calculations for two specific Heusler compounds, $Co_2FeAl_{0.3}Si_{0.7}$

and $Co_2MnGa$, by experimental analysis of the electronic properties by using two different spectroscopy methods: Ultraviolet Photoemission Spectroscopy (UPS) and Tunneling Spectroscopy (TS).

First, an introduction to Density Functional Theory (DFT) and its approximations are shown. Then, the theoretical background of the properties of half metallic ferromagnets, and, in particular, a review of all different predicted properties of these Heusler compounds depending on the influence of doping, disorder and defects are presented. Additionally, information of different existing experimental techniques and their results are discussed and it is shown why UPS and TS are used as experimental techniques in this work. After this, our experimental study on thin films of $Co_2FeAl_{0.3}Si_{0.7}$ and $Co_2MnGa$ is presented.

In order to achieve reliable and understandable results, it is important, as already mentioned, to study the quality of the material depending on the deposition parameters and to achieve an optimization of the preparation process in advance. Here, the preparation methods of the samples are explained, followed by the description and results of the different analysis techniques used for obtaining information about the bulk and surface crystallographic and magnetic properties. For the bulk properties, X-Ray Diffraction (XRD) for crystallographic ordering and Vibrating Sample Magnetometry (VSM) for magnetic properties are used. For the surface properties, the ordering of the surface is analysed by Reflection High Energy Electron Diffraction (RHEED), the morphology is observed by Scanning Tunneling Microscopy (STM), and X-Ray Magnetic Circular Dichroism (XMCD) experiments, where bulk and surface magnetic properties can be compared, are performed. Once the quality of the samples is optimized, a series of samples can be prepared for the final purpose of studying the electronic properties by two different spectroscopic methods. In the case of UPS, the surface occupied electron energy spectrum of the Heusler thin film is directly measured in situ after deposition. In the case of TS, the preparation of MTJ's is carried out. Here the different tunneling barriers normally used in MTJ's and their effects on the tunneling magnetoresistance value is discussed in order to clarify why amorphous $AlO_x$ insulators are used in this work. Moreover, an optimization process of growing $AlO_x$ on top of Heusler thin films is presented. After describing the lithography process used for the patterning of mesa structures, which makes possible to contact bottom and upper electrodes, the transport measurements

are done in a cryostat, where temperature and external magnetic field dependent measurements take place. Later, the results obtained by using the two different spectroscopic methods and discussions about their experimental limitations are put together and compared. Finally, by comparing experimental results with theoretical predictions, conclusions about the electronic properties of the Heusler alloys are presented.

# Chapter 2

# Theoretical background

Potential high spin polarized materials for spintronic applications are the so-called half metallic ferromagnets. In particular, many Heusler alloys have been predicted to be potential half metallic ferromagnets characterized by a high Curie temperature and a large band gap at the Fermi energy.

In this chapter an introduction to the density functional theory and its approximations followed by a theoretical background about the concept of half metallicity and the general properties of Heusler alloys are introduced. Furthermore, particular theoretical predictions by Band Structure Calculations (BSC) for two specific Heusler compounds which are investigated experimentally in this work are presented: $Co_2FeAl_{0.3}Si_{0.7}$ and $Co_2MnGa$. In addition, the predicted influence of doping, disorder and defects on the half metallicity properties of the Heuslers are put forward. Finally, with the aim of justifying the experimental techniques used in this work, an overview of different experimental methods and results for studying the half metallicity of certain Heuslers up to date are shown and discussed.

## 2.1 Density functional theory and approximations

In order to describe important physical aspects of a material in solid state physics, the Schrödinger equation of a many body system has to be solved. Due to the non-possible exact solution of such a very complicate problem, approximations

have to be applied. Density Functional Theory is one of the most popular and versatile quantum mechanical theory used to investigate the electronic structure of many-body systems and binding energy of molecules in condensed matter physics, computational physics and chemistry. It allows to restructure the complexity of the original problem and to express ground-state properties, such as total energies, equilibrium positions and magnetic moments, in terms of the electronic (spin) density of the system, and provides a scheme for calculating them. The short introduction to DFT here presented, is a summary of detailed and deeper explanations which can be found in different sources [32, 33, 34]. The Schrödinger equation for a many body system is expressed as follows:

$$\left[\sum_{i}^{N}\left(-\frac{\hbar^2\nabla_i^2}{2m}+v(\mathbf{r}_i)\right)+\sum_{i<j}U(\mathbf{r}_i,\mathbf{r}_j)\right]\Psi(\mathbf{r}_1,\mathbf{r}_2,\ldots,\mathbf{r}_N)=E\Psi(\mathbf{r}_1,\mathbf{r}_2,\ldots,\mathbf{r}_N) \tag{2.1}$$

where N is the number of electrons, the first term is the sum of the kinetic energy of all N electrons and can be written as an operator:

$$\hat{T}=-\frac{\hbar^2}{2m}\sum_{i}\nabla_i^2 \tag{2.2}$$

The second term is the sum of all electron and nuclei Coulomb interactions between an electron i with position r and a nuclei k with position R:

$$\hat{V}=\sum_{i}v(\mathbf{r}_i)=\sum_{ik}\frac{Q_k q}{|\mathbf{r}_i-\mathbf{R}_k|} \tag{2.3}$$

The third term is the Coulomb electron-electron interaction:

$$\hat{U}=\sum_{i<j}U(\mathbf{r}_i,\mathbf{r}_j)=\sum_{i<j}\frac{q^2}{|\mathbf{r}_i-\mathbf{r}_j|} \tag{2.4}$$

For a system that contains heavy atoms (large atomic number Z), the electrons are accelerated to relativistic velocities. In this case, relativistic effects, obtained by solving the Dirac equation, have to be included. In this case the Hamiltonian would require a Quantum Electro-Dynamic treatment [35]. A relativistic correction would include the following terms: a minimal relativistic correction to the kinetic energy, the Darwin term which modifies the Coulomb interactions and the spin-orbit coupling term as shown in this expression, respectively.

$$\hat{H_0}^{rel}=\sum_{i}^{N}\left\{\left[-\frac{1}{2m_c^2}\left(-\frac{\hbar^2\nabla_i^2}{2m}\right)^2+\frac{e}{8\mu^2}(\Delta\Phi_i)(\mathbf{r}_i)\right]1_2+\frac{e}{2\mu^2\hbar^2}\hat{S}_i[(\nabla\Phi_i(\mathbf{r}_i))\times p_i]\right\} \tag{2.5}$$

where $\Phi_i(\mathbf{r})$ is the sum of both Coulomb interaction potentials (electron-electron and electron-nuclei). The way of solving such a equation in the usual quantum mechanical approach consists in choosing the adequate potential v($\mathbf{r}$), implementing it on the Schrödinger equation, solving it and finally calculating all the observables. Due to the high number of values required to describe the wave function $\Psi$, solving such an equation requires a huge computational effort and it becomes unsolvable for complex systems.

The development of the Density Functional Theory was a powerful alternative to this computational problem and is nowadays the basis of the major electronic band structure calculations in the field of material and molecular science. It reduces the many body problem with 3N coordinates to a single body problem with 3 coordinates by taking as a variable, that defines all other observables, the electronic charge density n($\mathbf{r}$). It is based on the Hohenberg and Kohn theorems [36]:

- **Invertibility:** Every property of an interacting ground state fermion system, such as the ground state energy, is determined by the particle density of the system in its ground state.

$$E = E[n_0] \equiv \langle \Psi_0 | \hat{H} | \Psi_0 \rangle \tag{2.6}$$

- **Variational principle:** For an external potential $v$ it is possible to create a density functional $E_v[n]$ in such a way that the density and the ground state energy correspond to the minimum $E_v[n]$.

The formalism to calculate the ground state energy is now different. The energy as a density functional is expressed as follows:

$$E[n] = T[n] + U[n] + V[n] \tag{2.7}$$

$$V[n] = \int V(r) n(\mathbf{r}) d\mathbf{r} \tag{2.8}$$

The big question here is which expressions have to be used for T[n] and U[n]. At this point one needs reliable approximations for these two terms to begin with.

The different approximations will be discussed later, but let us assume that reliable expressions of these two terms are known. Then, the way of solving the

problem consists in minimizing the energy E[n] with respect to the density n($\mathbf{r}$). From the minimization, the ground state density $n_0(\mathbf{r})$ is obtained and therefore the ground state energy $E[n_0]$.

For the minimization process the expression of the functional energy can be rewritten as a fictitious functional of a non-interacting system:

$$E_s[n] = \langle \Psi_s[n] | T_s[n] + V_s[n] | \Psi_s[n] \rangle \tag{2.9}$$

where $T_s$ is the non interacting kinetic energy and $V_s$ is the external effective potential in which the particles are moving. It obeys the condition that $n_s(\mathbf{r})$=n($\mathbf{r}$) if

$$V_s = V + U + (T - T_s) \tag{2.10}$$

Thus, the problem reduces to solve the Kohn-Sham equations [37] of this non-interacting system.

$$\left[ -\frac{\hbar^2 \nabla^2}{2m} + v(\mathbf{r}) \right] \Phi_i(\mathbf{r}) = \epsilon_i \Phi_i(\mathbf{r}) \tag{2.11}$$

$$n(\mathbf{r}) = n_s(\mathbf{r}) = \sum_i^N f_i |\Phi_i(\mathbf{r})|^2 \tag{2.12}$$

where $f_i$ is the occupation of the i'th orbital and $\Phi_i(\mathbf{r})$ is the i'th Kohn-Sham single particle orbital.

The effective single particle potential can be written as:

$$V_s = V + \int \frac{e^2 n_s(\mathbf{r}')}{|\mathbf{r} - \mathbf{r}'|} d^3 r' + V_{XC}[n_s(\mathbf{r})] \tag{2.13}$$

where the second term is the mean field electron-electron Coulomb interaction (Hartree-energy) and $V_{XC}[n_s(\mathbf{r})]$ is the "exchange-correlation" potential, which is the only term which can not be exactly evaluated as a density function and it can be interpreted as the approximation term needed to correct the errors of the electron-electron Coulomb interaction and the kinetic energy of the non-interacting system.

The way of solving the Kohn-Sham equations is by using iteration methods. First an initial guess of n($\mathbf{r}$) is made to calculate $V_s$. Then the Kohn-Sham equations are solved in order to obtain all wave-functions $\Phi_i(\mathbf{r})$. With the wave-functions expressions a new density n($\mathbf{r}$) is calculated and the same process is repeated until convergence is reached. When the final value of the density is achieved, the eigenvalue of the energy is obtained, as well as all other observables, such as the energy gap, the ionization energy or the electron affinity. Therefore, by using this theory and its approximations, predictions of the electronic properties based on band structure calculations may be possible.

The DFT is formally an exact theory, but in order to be performed in actual applications, approximations to the exchange correlation term has to be used and it is the quality of these approximations what it limits the reliability of the results.

### 2.1.1 Approximations

Depending on the system under study, different approximations and choices can be made on every term of the Kohn-Sham equation in order to solve it.

$$\left[-\frac{\hbar\nabla^2}{2m} + v_{ext}(\mathbf{r}) + v_H(\mathbf{r}) + v_{xc}(\mathbf{r})\right]\Phi_i(\mathbf{r}) = \epsilon_i\Phi_i(\mathbf{r}) \tag{2.14}$$

In this section, each approximation term will be shortly mentioned and for a deeper understanding references are given.

For the kinetic energy term, the expression given in equation 2.14 is the classical term (non-relativistic limit). Alternatively, two other limits can be considered: scalar relativistic (by means of the relativistic kinetic energy operator and other simple relativistic corrections) or relativistic (solving the Dirac's equation, which includes also spin orbit coupling). The relativistic terms are used for systems with large atomic number Z, where the electrons are accelerated to relativistic velocities.

For the so-called external potential, the core electrons (inner electrons with an atomic-like configuration) can be treated in two different ways: explicitly, i.e. all electron calculation, or incorporated, i.e. the external potential is replaced by a pseudopotential which describes the effect of the core electrons and then

the Hartree and Exchange-Correlation terms are evaluated only for the valence electrons (valence density).

The Hartree potential can be obtained by solving the Poisson's differential equation or by integrating the charge density (Thomas-Fermi approximation).

The Exchange-Correlation potential has many choices available. Different approximations will be discussed later.

For most band structure calculations the eigenvalues of the Kohn-Sham equation are considered zero-order approximations to the actual energy spectrum.

The eigenfunctions can be also considered as auxiliary functions generating the density or interpreted as zero-order approximations to quasi-particle wave functions. The Kohn-Sham equation are usually solved by expanding the eigenfunctions in basis functions. There are many different types of basis functions that will be described later, too.

All approximations can be summarized in three different concepts:

1. Finding a good interpretation of the Kohn-Sham eigenvalues and orbitals as physical energies and wave functions.
2. Looking for numerical methods for solving the differential equation by selecting suitable basis functions.
3. Building an expression for the unknown Exchange-Correlation potential which contains all many-body aspects of the problem.

**Basis functions**

The construction of suitable basis functions is of relevance in electronic-structure theory. The different methods can be structured in three different blocks:

- Basis functions which do not depend on energy:
  - **Plane Wave Expansion Method**
    This method is popularly used for solving band structures of specific photonic crystal geometries. It is useful for obtaining solutions of

Maxwell's equations over an inhomogeneuos or periodic geometry [38, 39].

- **Linear Combination of Atomic Orbitals (LCAO)**
  The orbitals are described as linear combinations of basis functions. The basis functions are one electron functions centered on nuclei of the component atoms of the molecule. The atomic orbitals used are typically Slater-type orbitals or Gaussian functions. For more efficient calculation, this method makes use of the symmetry of the molecules and orbitals involved in bonding [40, 41].
- **Orthogonalized Plane Waves (OPW)**
  This method is appropriate to describe metallic crystals or semiconductors. It is a laborious procedure which consists in the selection of functions which are all orthogonal to the eigenfunctions of the core band of the crystal [42].

- Basis functions which depend on energy:
  - **Augmented Plane Waves (APW)**
    In this approximation the potential is assumed to be spherically symmetric within spheres centered at each atomic nucleus and constant in the interstitial region. The Augmented Plane Wave functions are constructed by matching solutions of the Schrödinger equation within each sphere with plane waves solutions in the interstitial region, and linear combinations of these wave functions are then determined by a variational method [43].
  - **Korringa-Kohn-Rostoker (KKR)**
    In this method the properties of the atomic potential and the geometry of the lattice are separated due to a two step calculation method. The first step describes the scattering properties of each scattering center (atom). In the second step, the multiple scattering by all atoms in the lattice is obtained by forcing the incident wave at each center to be the sum of the outgoing waves from all other centers. Its construction improved numerical efficiency. This method is able to describe impurities of the crystal, it is useful for multilayer systems with surfaces, interfaces and multilayers. It can also predict transport properties for diffusive and ballistic transport through junctions [44].

- Linear methods where the energy dependent basis functions are linearized (Taylor expanded) around some fixed reference energy. They are nowadays the most used methods because they can describe more complex and strongly correlated compounds.

  - **Linear Muffin Tin Orbitals (LMTO) and Linear Augmented Plane Waves (LAPW).**
    These two methods are based on the linearization of the KKR and APW methods, respectively. This reduction improves the numerical efficiency. These methods present many advantages: d- and f-metals and atoms with a large number of core states can also be considered. The use of a minimal basis leads to high efficiency and calculations for large unit cells are possible. By comparing the two methods, LAPW is the most generally applicable. It can also describe high energies and open structures. Although LMTO is only used for closely packed structures, due to the Muffin Tin potential approximation, this method is computationally more efficient when d-bands are present [45].

**Approximations to the Exchange-Correlation potential**

- Local functionals:

  - **Local (Spin) Density Approximation (L(S)DA)**
    This approximation considers that the functional depends only on the density at the coordinate where it is evaluated [47]. The most successful local approximation was derived from the homogeneous electron gas (HEG) model:

$$E_{xc}^{LDA}[n] = \int n(\mathbf{r})\epsilon_{xc}^{hom}(n)d\mathbf{r} \tag{2.15}$$

    The kinetic energy is approximated as a non-interacting kinetic energy of an homogeneous system in the Thomas Fermi approximation [46].

    In the Thomas Fermi approximation of an homogeneous system the kinetic energy is defined as

$$t_s^{hom}(n) = \frac{3\hbar^2}{10m}(3\pi^2)^{\frac{2}{3}}n^{\frac{5}{3}} \tag{2.16}$$

where n is constant. For an inhomogeneous system n=n($\mathbf{r}$)

$$t_s(\mathbf{r}) = t_s^{hom}(n(\mathbf{r})) = \frac{3\hbar^2}{10m}(3\pi^2)^{\frac{2}{3}}n(\mathbf{r})^{\frac{5}{3}} \tag{2.17}$$

The total kinetic energy is obtained by integrating the above term over all space

$$T_s^{LDA}[n] = \frac{3\hbar^2}{10m}(3\pi^2)^{\frac{2}{3}}\int n(\mathbf{r})^{\frac{5}{3}}d\mathbf{r} \tag{2.18}$$

The exchange correlation energy can be separated into an exchange part and a correlation part

$$\epsilon_{xc} = \epsilon_x + \epsilon_c \tag{2.19}$$

The exchange energy of the homogeneous electron liquid is known exactly and the LDA exchange energy can be approximated by it

$$E_x^{LDA} = -\frac{3q^2}{4}(\frac{3}{\pi})\frac{1}{3}\int n(\mathbf{r})^{\frac{4}{3}}d\mathbf{r} \tag{2.20}$$

The correlation energy expressions are obtained from parametrizations of Quantum Monte Carlo (QMC) calculations.
In LSDA one density for each spin is used. Spin dependent properties are obtained from calculations.

$$n(r) = n_\uparrow(\mathbf{r}) + n_\downarrow(\mathbf{r}) \tag{2.21}$$

$$E_{xc}^{LSDA}[n_\uparrow, n_\downarrow] = \int n(\mathbf{r})\epsilon_{xc}^{hom}(n_\uparrow, n_\downarrow)d\mathbf{r} \tag{2.22}$$

– **Local (Spin) Density Approximation plus Exchange Coulomb Parameter U (L(S)DA+U)**
There are some systems, such as transition metals or rare-earth metal compounds, where the LDA approximation is not successful. The LDA+U approximation is successful in describing long-range ordered insulating states of correlated electronic systems. It is able to correct and improve properties of these systems such as energy gaps, magnetic moments and interatomic exchange parameters [48].

This method consists of making a separation into two subsystems: one subsystem consists of the localized d- or f-electrons contribution, for which Coulomb d-d interactions, described by Hubbard's model, should be taken into account by a term $\frac{1}{2}U\sum_{i\neq j} n_i n_j$ as in a mean field approximation. $n_i$ are d-orbital occupancies. The other consists of a delocalized s,p-electrons contribution which could be described by using an orbital-independent one-electron potential, like LDA.

The total energy functional will be described as follows

$$E^{L(S)DA+U} = E_{LDA} - UN(N-1)/2 + \frac{1}{2}U\sum_{i\neq j} n_i n_j \qquad (2.23)$$

where the first term describes the s,p-electrons obtained from LDA, the last term is the correction that describes the Coulomb d-d interaction from Hubbard's model [49], and the second term is the interaction between the two subsystems. U is the so called Coulomb exchange parameter and it is defined as the energy separation between upper and lower Hubbard bands.

- Semilocal functionals:
  - **Generalized Gradient Approximation (GGA)**
    A real system is spatially inhomogeneous, i.e. it has varying density $n(\mathbf{r})$. Therefore, it is useful to include the information on the rate of this variation in the functional. This is made in the GGA method by describing the functional as general functions of the density $n(\mathbf{r})$ and its gradient $\nabla n(\mathbf{r})$ [53, 54].

$$E_{xc}^{GGA}[n] = \int f(n(\mathbf{r}), \nabla n(\mathbf{r}))d\mathbf{r} \qquad (2.24)$$

- Non-local functionals:
  - **Hybrids**
    In quantum chemistry the most used functionals are based on hybrid functionals [55]. The general principle consists in mixing a fraction of exchange from Hartree-Fock theory with exchange and correlation

from GGA semilocal exchange. It is a semi-empirical method because it uses parameters that are determined from fitting functional predictions obtained by GGA with experimental results.
This approximation improves many molecular properties, such as atomization energies, bond lengths and vibration frequencies.

- **Meta Generalized Gradient Approximation (Meta-GGA)**
  This approach also includes as functional of the exchange correlation energy the Kohn-Sham kinetic-energy density [56]

$$\tau(\mathbf{r}) = \frac{\hbar^2}{2m} \sum_i |\nabla \Phi_i(\mathbf{r})|^2 \tag{2.25}$$

- **Self Interaction Corrections (SIC)**
  In DFT the Coulomb interaction is the same as in Hartree-Fock, but the exchange term is an approximation. Thus, the cancellation of the self-interaction (one electron interacts with its own mean-field) in Coulomb and exchange terms is incomplete. SIC tries to solve this problem by substracting orbital by orbital, the contribution that Hartree and exchange correlation functionals would make if there was only one electron in the system [57].

- **Optimized Effective Potential (OEP) and Optimized Potential Models (OPM)**
  These two approaches are used to be able to minimize the energy obtained by using the orbital functionals mentioned above. The energy in this case depends implicitly on the density via the orbital functionals. Therefore, approximations have to be done in order to be able to calculate its derivative with respect to the density for minimization. In the case of the kinetic energy the indirect approach is obtained by following the Kohn-Sham scheme. OEP [58] or OPM [59] are the methods used to obtained the indirect scheme of the exchange correlation energy.

- **Local (Spin) Density Approximation plus Dynamical Mean Field Theory (L(S)DA+DMFT)**
  L(S)DA+U is not able to describe all strongly correlated systems because it does not contain true many-body physics. For example, this approximation fails when describing strongly correlated paramagnetic states or Mott

metal-insulator transitions.

In this sense, a new and promising method was developed in 1989, which is able to capture the many-body nature of the electron-electron interaction: the LDA+DMFT approximation [50, 51, 52]. It contains the frecuency dependence of the self-energy and is able to describe strongly correlated systems, like paramagnetic metals, Mott metal-insulator transition, doping of the Mott insulator. It can determine phase diagrams, calculate thermodynamic properties, one-particle functions and response functions, like competition of the spin, charge and orbital order.

The idea is basically using the LDA band structure calculation as input and then introduce the missing electronic correlations by DMFT. In this approximation the dynamics at a given site is seen as an interaction of the degrees of freedom at this site with an external bath created by all other degrees of freedom on other sites. Thus, this mean field theory reduces the many degrees of freedom of the many-body problem by a single-site effective problem with less degrees of freedom.

The benefit of this method is that quantum fluctuations are included which result in a finite lifetime of the electronic states.

DMFT has demonstrated to be a powerful method which is able to solve and improve many of the problems inherent to strongly correlated systems which L(S)DA+U was not able to predict.

Most band structure calculations found in literature are based on Density Functional Theory (DFT) in the Local Density (LDA) or Generalized Gradient Approximation (GGA). Nevertheless, the development of LDA+DMFT and its recent applications on different strongly correlated materials, have shown how this new approximation fits much better than L(S)DA with experimental results, not only qualitatively but also quantitatively [60].

In order to show the differences between the two approximations a comparison of the band structure calculation of the transition metal ferromagnet Fe by

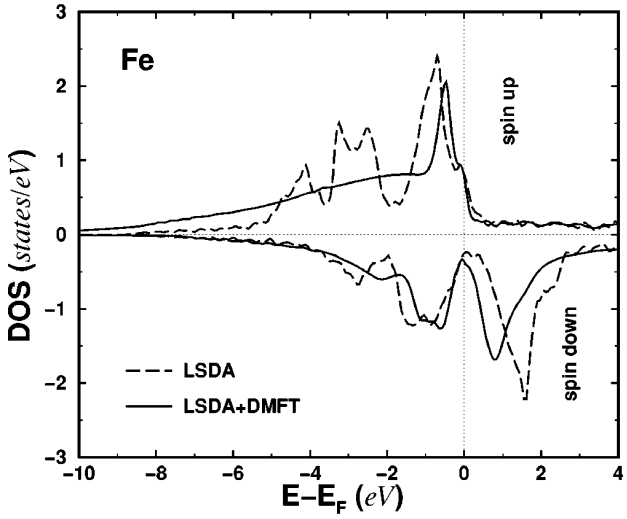


**Figure 2.1:** *The LSDA (dashed line) and the LSDA+DMFT (solid line) densities of states for bcc Fe [61].*

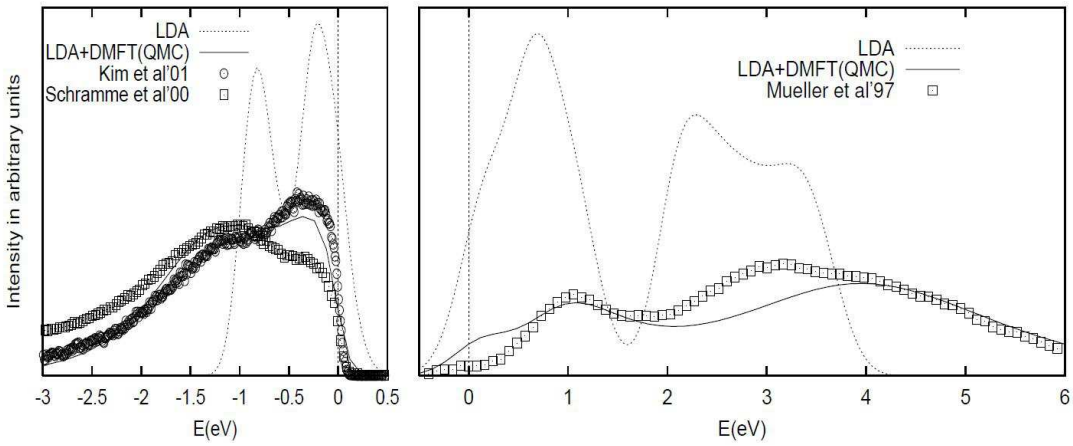


**Figure 2.2:** *Comparison of the LDA+DMFT spectrum below (left figure) and above (right figure) the Fermi energy with the LDA spectrum and the experimental spectrum (left: photoemission spectrum; right: X-ray absorption spectrum) [51].*

using LSDA and LSDA+DMFT [61] is shown in figure 2.1. Because of the finite lifetime, a smearing of the DOS features is clearly observed in LSDA+DMFT.

An example of experimental photoemission and absorption spectrocopy matching with these two approximations (LDA and LDA+DMFT) is shown in figure 2.2 for the transition metal oxide $V_2O_3$ [51]. While experiments differ strongly from LDA predictions, LDA+DMFT is able to reproduce experimental results qualitatively and quantitavely.

## 2.2 Half metallic ferromagnets

Half metallic ferromagnets are highly spin polarized materials due to an unusual band structure: they behave as metals for one spin channel and as semiconductors (or insulators) for the other spin channel due to the presence of a gap in the density of states (DOS) at the Fermi energy. This means that in the ideal case these materials have only one spin channel for conduction giving rise to an ideal spin polarization of 100 %.

In order to visualize this concept a comparison of the spin dependent density of states as a function of the energy between paramagnetic, conventional ferromagnetic and half metallic ferromagnetic materials and the definition of spin polarization are shown with a simple sketch in figure 2.3.

In a paramagnetic material the DOS of the spin down electrons is the same as those of the spin up electrons at the Fermi energy, i.e. there is the same number of electrons with spin up and spin down resulting in zero spin polarization. In a conventional ferromagnet the DOS of one spin channel (whether up or down) is lower than the other at the Fermi energy, causing a non-zero spin polarization. In a half metallic ferromagnet there is no DOS in one of the spin channels, all the electrons have the same spin direction at the Fermi energy giving rise to a spin polarization of 100 %.

This new concept was introduced in 1983 by Groot et al. [64]. They report this new and unusual half metallic behaviour based on theoretical studies of the spin dependent (majority $\uparrow$ or minority $\downarrow$) band structure with the Augmented-Spherical-Wave-Method of the two Heusler compounds NiMnSb and PtMnSb. A

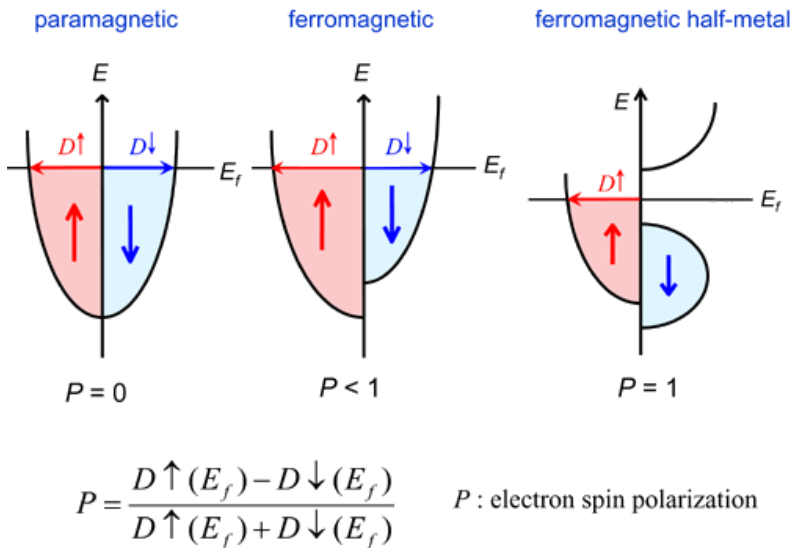


**Figure 2.3:** *Densities of states of paramagnetic, ferromagnetic and ferromagnetic half metal materials and definition of spin polarization [63].*

great interest to understand this property and try to demonstrate it experimentally stirred up.

Later on, many other compounds were predicted to be half metals, for instance, many other Heusler compounds like $Co_2MnZ$ (Z=Si,Ge) [65, 29], CoMnSb [66], $Co_2Cr_{1-x}Fe_xAl$ [29, 67], oxide compounds like $CrO_2$ [68], perovskites like $La_{0.7}Sr_{0.3}MnO_3$ [69] or zinc blende compounds like MnAs [70].

100 % spin polarized materials can be obtained by means of ferromagnetic materials that have no unpolarized s,p states at the Fermi energy or by intermetallic covalent compounds through hybridization between the electrons of different atoms [81].

Spin resolved band structure calculations within LSDA and LDA+DMFT of the half Heusler NiMnSb are shown in figure 2.4 as examples of half metallic ferromagnets [71]. The majority band is referred to the DOS of electrons with spin up and the minority band to the DOS of electrons with spin down. At the Fermi energy there is DOS in the majority band, whereas in the minority band no states are present.

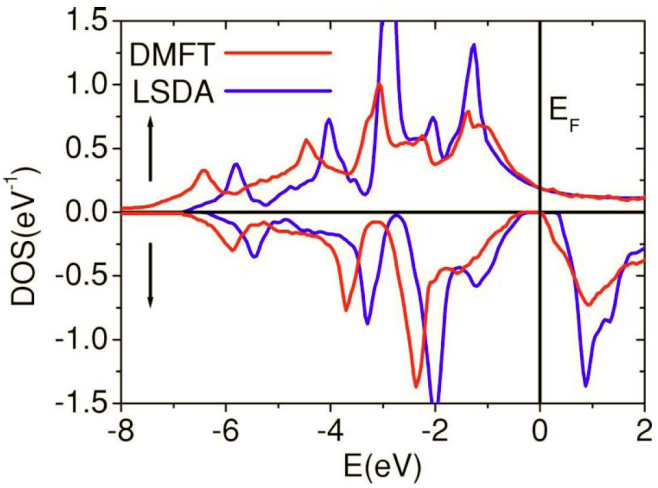


**Figure 2.4:** *Density of states for HMF NiMnSb in LSDA scheme (blue line) and in LDA+DMFT scheme (red line) at T=300 K [71].*

## 2.3 Heusler Compounds

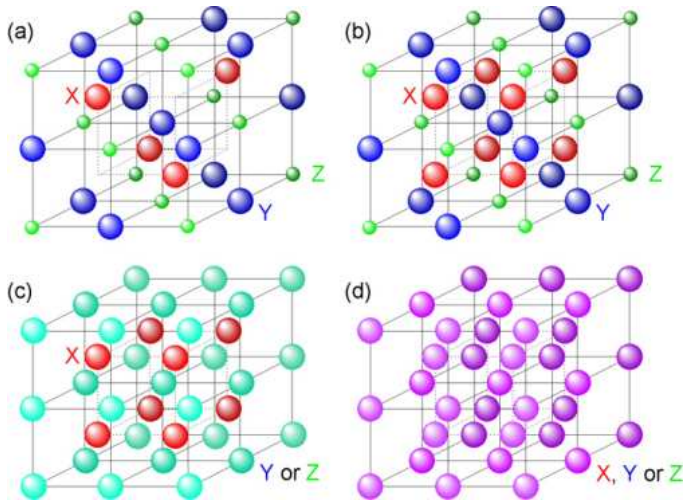


**Figure 2.5:** *Crystalline structures of Heusler compounds [82]. (a) is a $C1_b$ crystallographic structure with a XYZ composition. (b) is fully ordered $L2_1$ structure with a $X_2YZ$ composition. (c) is a B2 structure with Y-Z disorder. (d) is an A2 structure with X-Y and X-Z disorder.*

In particular, Heusler compounds [62] are potential candidates for showing half metallic properties [13, 14, 15] with a high Curie temperature above room

temperature and a large band gap at the Fermi energy. They belong to a group of ternary intermetallics and are categorized in two distinct groups depending on their crystalline structure:

- **Heusler alloys**: with a $X_2YZ$ composition in a $L2_1$ crystallographic structure which is formed by four face-centered-cubic (fcc) sublattices occupied by three kinds of atoms (X,Y and Z). The two fcc sublattices of the X atoms combine to a simple cubic sublattice (e.g., $Co_2MnGe$, $Co_2MnSi$ [65, 77] and many other $Co_2$-based Heusler alloys [78], $Fe_2MnSi$ [79], $Rh_2MnGa$ [80])(figure 2.5 (b)).
- **Half Heusler alloys**: with a XYZ composition in a $C1_b$ crystallographic structure. It is formed by removing one of the X sites of the Heusler structure (e.g., NiMnSb, FeMnSb, CoMnSb [81]) (figure 2.5 (a)).

X is a transition metal like Co, Cu, Fe, Pt or Ni; Y is a transition or rare earth metal while Z is a semiconductor or non magnetic metal and denotes an sp element of the groups III-V of the periodic table like Al, Sn, Sb, Ge, Si or Ga.

Concerning crystallographic disorder, Heusler alloys with a $L2_1$ structure transform into the B2 structure (figure 2.5 (c)) when the Y and Z atoms mix their sites (Y-Z disorder) and eventually occupy their sites absolutely at random. Moreover, they form an A2 structure (figure 2.5 (d)) when there is disorder on all sites. Another kind of disorder is the so-called $DO_3$ which consists on random distribution between atoms on the X and Y positions.

A possible origin of the gap in Heusler compounds (see figure 2.4 for NiMnSb as an example) is discussed by Galanakis et al. through hybridization between states close to the Fermi energy [81].

For the case of half-Heusler alloys, like NiMnSb, the gap is originated by the strong hybridization between the d-states of the two transition metals (Ni, Mn). This hybridization results in fully bonding states in the valence band and empty antibonding states in the conduction band. Thus, an energy gap is generated and the Fermi energy lays within the gap as can be seen in figure 2.6 (a). The sp-states of Sb do not affect the DOS of the Fermi energy and are not responsible for the existence of the minority gap due to the fact that these states lay deeper. Nevertheless, it has been demonstrated that the sp-elements are decisive for the

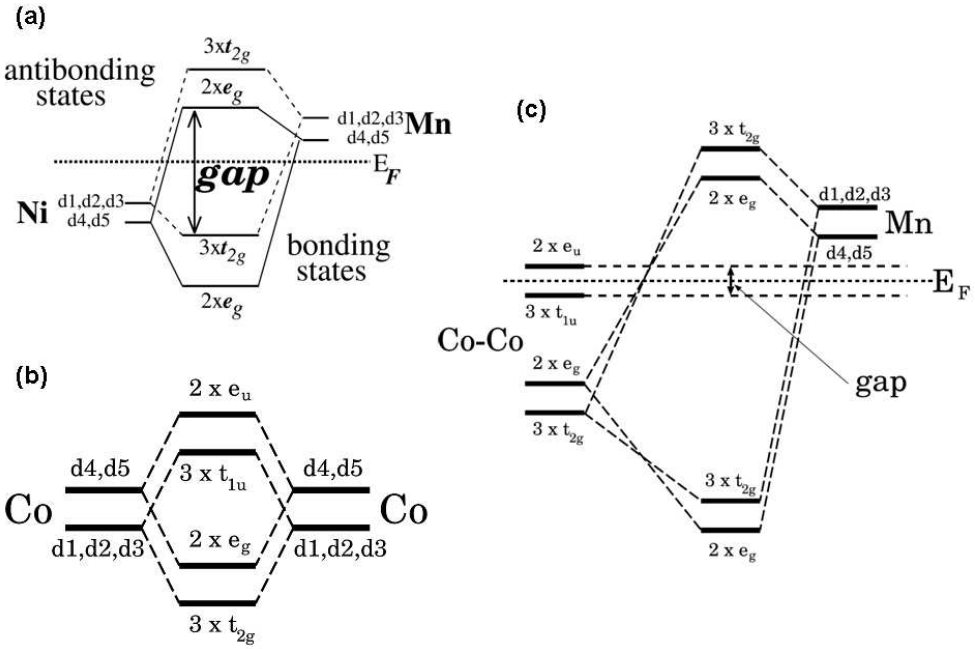


**Figure 2.6:** *Illustration of the origin of the gap in Heusler compounds through hybridization [81]. (a) is an example of Ni-Mn hybridization for the half-Heusler case. (b) and (c) show the hybridization between Co-Co atoms and between the resulting states with the Mn, respectively. d1, d2 and d3 denote the $d_{x,y}$, $d_{yx}$ and $d_{zx}$ $t_{2g}$ orbitals, respectively, and d4, d5 for the $d_{z^2}$, $d_{x^2-y^2}$ $e_g$ orbitals. The numbers in front of the orbitals indicate the degeneracy of each orbital.*

structural stability of the half-Heusler compounds [15]. Replacing one sp-element by another shifts the Fermi energy, and it can move of the gap.

For Heusler alloys, like $Co_2MnZ$, things are more complicated. Two hybridization processes have to be taken into account. Firstly, hybridization between the Co-Co d-states is relevant here due to the closer distance between each Co atom than in the half-Heusler case. It is the origin of bonding hybrids and antibonding orbitals ((b) in figure 2.6). Secondly, the hybridization between the Co-Co orbitals with the Mn d-orbitals creates a doubly degenerate bonding state that is very low in energy and an antibonding one that is unoccupied and above the Fermi level ((c) in figure 2.6). In this case, the real gap size is determined by the Co-Co interaction. The sp-states act in the same way as for half-Heuslers.

The magnetic moment of half metallic Heusler ferromagnets can be described by the "Slater Pauling rule" [83, 84]. This rule relates the total moment of the Heusler alloy $M_t$ with the total number of valence electrons per unit cell $Z_t$. It neglects the small orbital moments of the Heusler compounds.

$$M_t = Z_t - 18 \quad \text{for half-Heusler compounds} \tag{2.26}$$

$$M_t = Z_t - 24 \quad \text{for Heusler compounds} \tag{2.27}$$

The total number of electrons is the sum of the total number of spin-up and spin-down electrons whereas the total moment is the difference.

$$Z_t = N_\uparrow + N_\downarrow \tag{2.28}$$

$$M_t = N_\uparrow - N_\downarrow \Rightarrow M_t = Z_t - 2N_\downarrow \tag{2.29}$$

The number 18 for the half-Heusler compounds originates from the 9 fully occupied minority bands while for the Heusler compound the number 24 is because there are 12 electrons per unit cell in the minority band.

The two different Slater Pauling diagrams are shown in figure 2.7. The left one refers to the half-Heuslers and the right one to the Heuslers. Both diagrams show the comparison of the Slater-Pauling prediction with calculated magnetic moments within LDA in connection with the FSKKR (Full-potential Screened KKR). The full dots are referred to those compounds that, by theoretical calculations, show half-metallicity. However, the open dots, which do not follow the

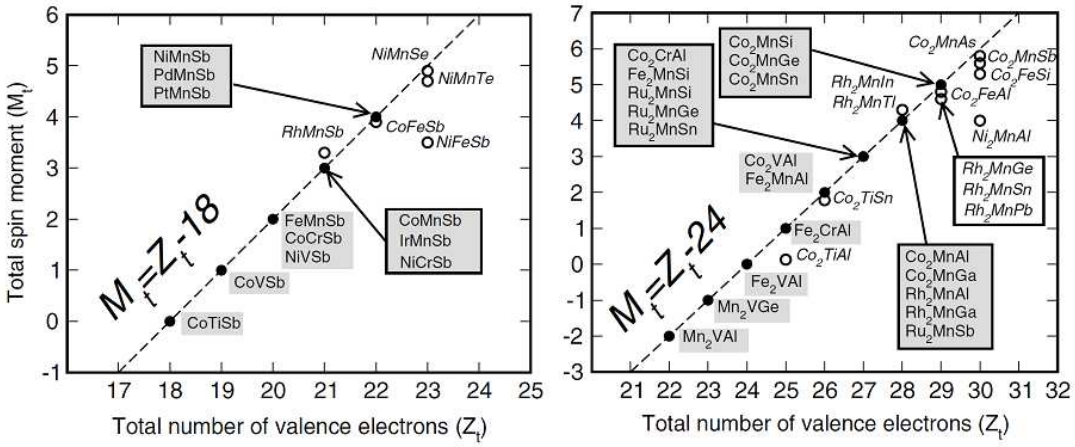


**Figure 2.7:** *Slater-Pauling behaviour for Half-Heusler (left) and Heusler compounds (right)[81]. The dashed line refers to the Slater-Pauling behaviour. The full dots are half-metallic predicted Heusler compounds calculated by LDA with the FSKKR and the open dots are the non-half metallic ones.*

Slater-Pauling rule, where predicted non-half metals.

An important aspect to discuss is the relevance of electronic correlations. Heusler alloys contain d electrons at the Fermi energy. Consequently, electronic correlations should not be neglected. Most of the band structure calculations for Heusler compounds, which can be found in literature, make use of LDA, LDA+U or GGA approximations, which do not describe strong correlations properly. However there has been some experimental evidence of strong correlation effects in some Heusler alloys which these approximations can not explain: the presence of non-quasiparticle states [74, 76].

Non-quasiparticle (NQP) states originate from spin-polaron processes forming a superposition of conduction electron excitations and virtual magnon excitations. They are a many body effect which is characteristic for half metallic ferromagnets and caused by dynamical electron correlations within the half-metallic band gap [72, 12]. They appear above the Fermi level for half metals with a gap in the minority band, while for the case of a band gap in the majority band they appear below the Fermi energy [73]. The spectral weight of NQP states increases when temperature rises and their tail crosses the Fermi energy. Therefore they may strongly influence the temperature dependence of the spin polarization in

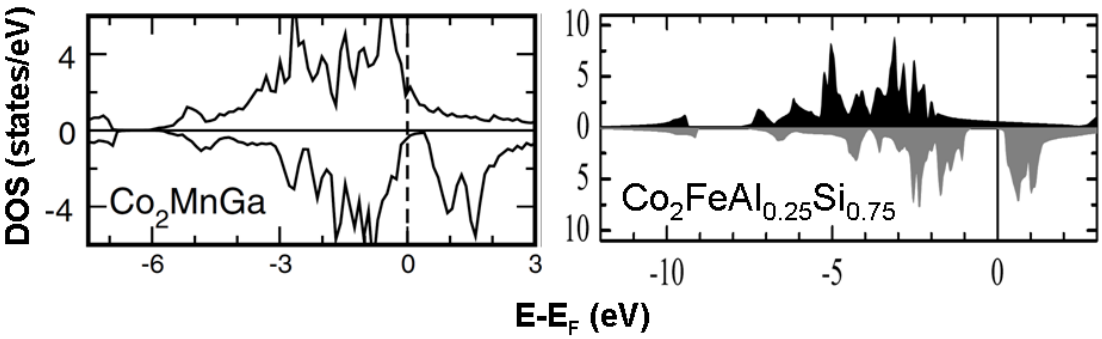


**Figure 2.8:** *Spin-resolved DOS for $Co_2FeAl_{0.25}Si_{0.75}$ calculated by LDA+U with the FLAPW (right) [85] and $Co_2MnGa$ calculated by LDA with the FSKKR (left) [81].*

half metals if correlations are strong as observed by Chioncel et al. [74] for the Heusler compound $Co_2MnSi$.

NQP states have been predicted in other Heuslers like NiMnSb [71] and FeMnSb [75] by LDA+DMFT and experimental techniques to detect them are suggested [71]. Examples of experimentally observed NQP states are published in [74] ($Co_2MnSi$) and [76] ($Co_2FeAl$ and $Mn_2VAl$). For such an effect, LDA+DMFT has demonstrated to be a powerful tool to explain its origin theoretically.

Taking into account its good agreement with experimental results, LDA+ DMFT seems to be the most powerful technique which takes strong correlation effects into account.

In this work, the DOS of the Heusler compounds $Co_2FeAl_{0.3}Si_{0.7}$ and $Co_2MnGa$ were experimentally investigated. The theoretical predictions for the electronic and magnetic properties are based on LDA+U with the FLAPW (Full-potential LAPW) [85] and on LDA with the FSKKR (Full-potential Screened KKR) [81] approximations, respectively.

The spin resolved band structure calculations for a perfect $L2_1$ structure are shown in figure 2.8, right for $Co_2FeAl_{0.25}Si_{0.75}$ and left for $Co_2MnGa$. Their

predicted magnetic moments are 5.75 $\mu_B$/f.u. and 4.05 $\mu_B$/f.u., respectively. Although, as can be seen in figure 2.8 left, $Co_2MnGa$ is not really a half metal (at the Fermi energy a small DOS contribution at the minority band is present), this material is important for our experimental investigations because strong changes of the DOS features take place close to the Fermi energy. Hence, it would facilitate the detection of DOS features experimentally. This argument will be explained in chapter 6, about tunneling spectroscopy.

In the following subsections, a review on different aspects that could modify the DOS and could affect half-metallicity in Heusler compounds are presented.

### 2.3.1 Effect of lattice parameter changes

Studies of the pressure dependence on $Co_2MnSi$, $Co_2MnGe$ and $Co_2MnSn$ [86] revealed that the minority gap increases with compression and the Fermi energy shifts closer to the conduction band. However, for changes of $\pm$ 2 % of the lattice constant half metallicity is conserved and the total moment remains constant, since the Fermi energy stays within the gap. Unfortunately, no corresponding study on $Co_2FeAl_{0.3}Si_{0.7}$ and $Co_2MnGa$ was carried out.

### 2.3.2 Temperature dependence of the spin polarization

Experimental investigations on different Heusler compounds observed indirectly, through TMR measurements, a reduction of the spin polarization when temperature is increased. In the case of $Co_2MnSi$ [87, 88] the authors proposed that such a reduction could be due to spin-flip processes due to magnetic impurities at the Heusler-insulator interface. Another possibility would be the loss of half metallicity with increasing temperature. Moreover, our investigations of this phenomena on $Co_2Cr_{0.6}Fe_{0.4}Al$ and $Co_2CrAl$ Heusler alloys revealed that although the TMR decreases with increasing temperature, no reduction of the magnetic moments at the Heusler-insulator interface is observed [89]. LDA+DMFT explains this behaviour in terms of the already mentioned non-quasiparticle states [71, 75].

### 2.3.3 Spin-Orbit coupling

Although it was demonstrated that in the presence of Spin-Orbit coupling (SOC) the polarization at the Fermi energy is reduced, its value is still high. For weak

SOC materials the spin polarization is close to 100 %. However for half metallic ferromagnets with heavy elements the SOC influence is stronger and it should not be neglected [90, 91].

### 2.3.4 Effect of disorder

The effect of disorder on the half metallic properties of Heusler compounds is an aspect studied by several groups and on different Heusler alloys. It has been demonstrated that the effects of disorder depend on the Heusler compound under study. Disorder is an important issue to study because, although theory predicts half metallicity for perfect $L2_1$ or $C1_b$ structures, experimentally no perfect order growth can be achieved. For this reason, it is important to investigate how disorder would affect half metallicity in each particular case.

$Co_2FeAl_{0.3}Si_{0.7}$ is a quaternary Heusler alloy which is obtained by doping the primary $Co_2FeSi$ Heusler compound with Al atoms. Disorder effects in $Co_2FeSi$ were theoretically studied by Gercsi and Hono [92]. The influence of disorder on the DOS is plotted in figure 2.9.

BSC based on GGA+U predict changes on the DOS features when some percent of disorder is induced. As far as these changes are not present close to the Fermi energy and do not affect the energy gap, the half metallicity is conserved. However, as can be observed in figure 2.9, 25 % of B2 order already originates states close to the Fermi energy in the minority conduction band. In the case of $DO_3$ disorder, the gap becomes very small and the Fermi energy is now close to the minority valence band. For A2 disorder, the situation even makes the spin polarization to reverse its sign. No gap is present any more and there is more DOS in the minority band than in the majority, hence a negative spin polarization is predicted in this case. This analysis reveals that this compound is quite sensitive to disorder effects and the loss of half metallicity could be easily achieved.

To the best of our knowledge, no BSC of $Co_2MnGa$ depending on crystallographic disorder has been published. Even so, one would expect that disorder would not improve the non-half metallic behaviour of this Heusler compound. In any case, it could decrease the spin polarization.

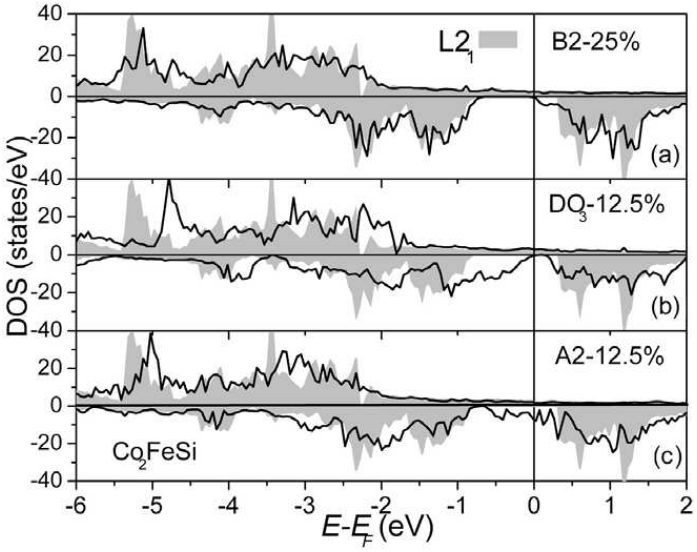


**Figure 2.9:** *Spin-resolved DOS for different types of disorder in $Co_2FeSi$. The perfect $L2_1$ ordered phase is shown in grey for comparison. (a) is the total DOS with 25 % B2 disordered phase, (b) corresponds to the total DOS with 12.5 % $DO_3$ disordered phase and (c) shows the total DOS with 12.5 % A2 disordered phase [92].*

### 2.3.5 Effect of doping

Investigating the effects of doping in Heuslers, help to find improvements on material properties such as half metallicity, magnetic moment and Curie temperature. In the case of $Co_2FeSi$ it was found that by doping with Al atoms, the band structure does not change, but a shift of the Fermi energy within the gap occurs. This effect can be observed in figure 2.10. The Fermi energy is close to the minority valence band edge when 100 % of Al atoms occupied the Z position and no Si is considered. With reducing the Al concentration and increasing the Si one, a gradual shift into the minority conduction band takes place. One would expect that the $Co_2FeSi_{0.5}Al_{0.5}$ is the ideal half metallic composition because the Fermi energy is situated exactly in the middle of the gap. However, in figure 2.11, the dependence of the total energy of the crystal structure on alloying concentration and disorder demonstrates that, for such a composition, the $L2_1$ phase is less stable than the partly B2 or $DO_3$ disordered phases. Although, for these two types of disorders the compound would stay half metal, they are not explained by band structure calculations. Therefore, in order to compare theoretical pre-

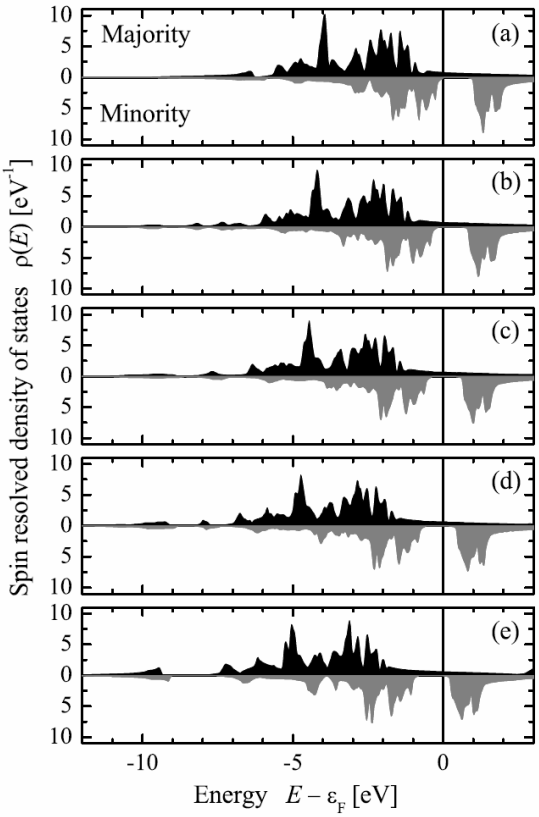


**Figure 2.10:** *Spin-resolved DOS of $Co_2FeAl_{1-x}Si_x$ for different Si concentrations. The graphs from (a) to (e) show the DOS with increasing amount of Si for x = 0, 0.25, 0.5, 0.75 and 1 [85].*

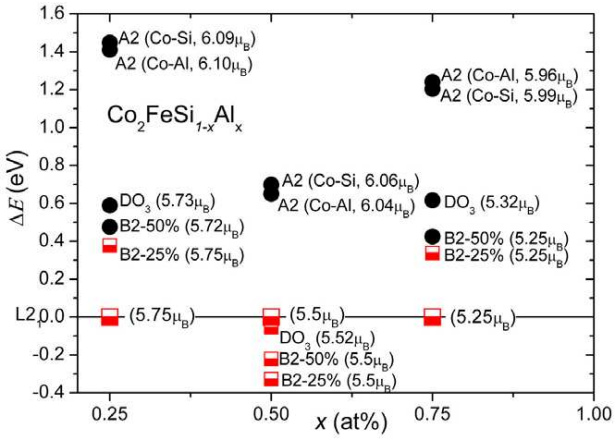


**Figure 2.11:** *The effect of alloying (x is Al concentration) and the effect of various disorders for the half-metallicity in $Co_2FeAl_{1-x}Si_x$ alloys compared by their difference in total energy. The half-filled squares represent P=1, while full circles indicate decreased spin polarization (P<1) as a result of the calculations. For 0.25 % and 0.75 % Al concentration, $L2_1$ phase was found to be the most stable comparing the total energies [92].*

dictions with experiment, a compound with the presence of $L2_1$ order is needed. Taking this into account, together with both considerations, energy stability and position of the Fermi energy within the gap, $Co_2FeAl_{0.3}Si_{0.7}$ composition can be considered a good candidate for the study of half metallicity.

For $Co_2MnGa$ no improvement of half metallicity by doping with Cr or Fe atoms was predicted [93].

### 2.3.6 Defects and impurities

Defects and impurities effect spin polarization measurements indirectly because they effect the conductivity values in tunneling transport. They make the detection of a high spin polarized material and therefore the demonstration of half metallicity difficult. A theoretical study was done by Vedyayev et al. [94]. They made an analysis of how impurities and defects originate scattering and spin-flip processes at the metal/insulator interface of magnetic tunneling junctions. They concluded that interfacial roughness can either increase or decrease the conductance and magnetoresistance. In contrast, magnon scattering always increases the conductivity and decreases the magnetoresistance amplitude up to a point

where it can eventually become negative. Consequently non-reliable value of the spin polarization would be measured.

## 2.4 Experimental techniques to determine half metallicity

There are different methods to indirectly determine the spin polarization of materials. In general, they can be classified as follows:

- Photoemission spectroscopy, used to determine the spin dependent density of states at the Fermi level.
- Tunneling spectroscopy, used to determine the spin dependent currents in a spin transport device.

Additionally, a bulk sensitive technique to determine the spin polarization by means of the direct probe of the bulk density of states is the so-called spin resolved positron annihilation.

In order to have a basic idea of each of these techniques, a short description is given in this section. For a deeper understanding of each method some references are given. Finally, different reasons for the use of photoemission spectroscopy and tunneling spectroscopy on Magnetic Tunneling Junctions in this work are discussed.

### 2.4.1 Spin-resolved positron-annihilation

This method is claimed to be the most direct one to probe bulk density of states. Nevertheless, its interpretation is not always clear and sample preparation can be tedious, expensive or demanding.

The general positron-annihilation experiment consists, as its name indicates, in the annihilation of positrons with electrons in the solid. This effect takes place after a thermalization process. The positrons slow down to thermal energies because, after impinging on the solid, they penetrate losing energy by excitation and ionization of atoms. After thermalization, two gamma-rays are emitted in opposite directions that contain energy and momentum information of the

positron-electron pair.

The positron beam possesses an average polarization along the beam axis. The annihilation takes place only between a positron and electron with opposite spins. Therefore a spin dependent distribution of the annihilation probability depending on the angle of emission (angular correlation) can be measured by applying a magnetic field parallel or antiparallel to the positron polarization. The sum and difference of these two spin-dependent distributions are related to the two spin-dependent electronic density of states. Accordingly by mapping and comparing experimental and theoretical distributions, one can directly see if the material shows the same density of states as theoretically predicted [95, 96].

Although this method seems to be ideal for the study of the electronic structures, it was discovered that some annihilation parameters in the relation between measured angular distribution and density of states are sensitive to lattice imperfections, because the positron may be trapped in crystal defects until annihilation. In fact, this method is nowadays mainly used to study crystal defects [97].

### 2.4.2 Spin polarized (inverse) photoemission

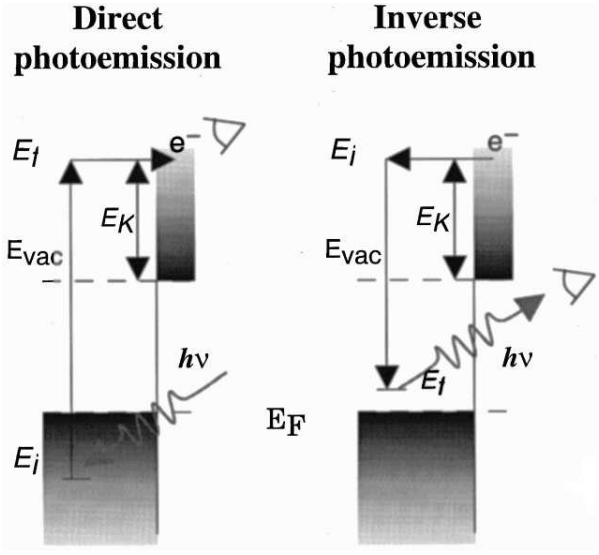


**Figure 2.12:** *Schematic representation of the excitations involved in direct (left) and inverse (right) photoemission [103].*

In general, all photoemission spectroscopy methods are interesting in studying the nature of the electronic states of a solid. They provide information about the band structure of the solid.

Experimentally, electromagnetic radiation is impinging on the surface under investigation. If the energy of the photons is sufficiently high, some electrons will be emitted. Once outside the solid their properties can be measured in terms of kinetic energy, emission angles $\theta$ and $\phi$, and spin. In fact, what it is usually done is a scan of the electron-energy-distribution spectrum for fixed emission angles or integrated over the total half space, see figure 2.12 left.

From the observation of the excited states of the system, one can get information about the initial states. This interpretation in terms of the initial states is not trivial and different models have been developed in order to get reliable and consistent interpretations: three step model and one step model [98, 99].

The physical aspects under study in photoemission are limited by the used photon energy. The classification depending on their photon energy range is:

- Ultra-violet Photoemission Spectroscopy (UPS) $\rightarrow 5 < \mathrm{E} < 100$ eV
- Soft X-ray Photoemission Spectroscopy (SXPS) $\rightarrow 100 < \mathrm{E} < 1000$ eV
- X-ray Photoemission Spectroscopy (XPS) $\rightarrow \mathrm{E} > 1000$ eV
- Hard X-ray Photoemission Spectroscopy (HAXPES) $\rightarrow 6 < \mathrm{E} < 10$ keV

With photoemission spectroscopy, information about the valence band structure of a solid can be obtained. Due to its low energy range, UPS is surface sensitive with an usually penetration depth of 10-15 Å. With XPS the chemical composition can be determined. HAXPES is bulk sensitive due to its high energy range. Thus, the deepest possible information is achieved.

In spin-polarized photoemission, the DOS of a material is mapped for each spin direction. This is achieved by the implementation of a spin polarimeter in the detector, which allows to separate intensity contributions depending on the spin direction [100].

In the case of inverse photoemission spectroscopy, the unoccupied electronic structure of thin film surfaces is studied. Information about the DOS above the Fermi energy is obtained. The process is now inversed compared with normal photoemission spectroscopy. An electron beam of a well defined energy is directed at the sample. The electrons coupled to high unoccupied states decay to low unoccupied states, emitting photons in the decay process which are detected, giving rise to a spectrum which relates the photon intensity with the incident electron energy, see figure 2.12 right. Typical energies used are below 20 eV, hence the small penetration depth allows to get only surface information [101, 102].

### 2.4.3 Tunneling spectroscopy

- **Point contact Andreev reflection**

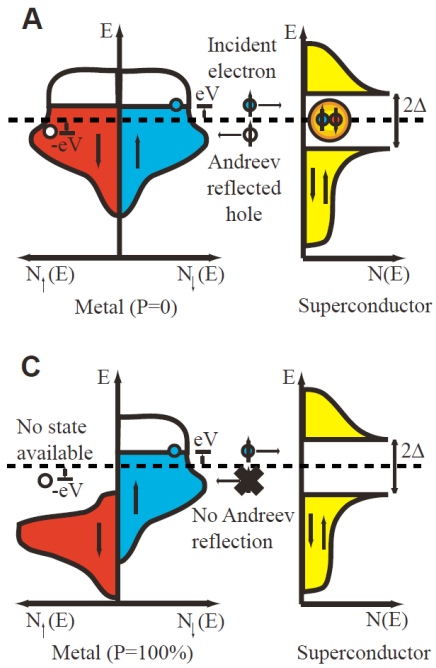


**Figure 2.13:** *Schematic representation of the Andreev reflection process for P=0 (upper part) and for P=100 % (lower part). The solid circles denote electrons and the open ones denote holes [104].*

Andreev reflection is a charge transfer process, which consists in the conversion of normal current in a supercurrent. Such a process takes place at

the interface between a normal state material and a superconductor. The effect is investigated on metallic point contact between two materials.

The general process can be described as follows:
An electron from the normal state material comes into contact with the interface. When the energy is lower than the energy gap of the superconductor, the incident electron forms a Cooper pair in the superconductor with the reflection of a hole with opposite spin and momentum. To form the Cooper pair in the superconductor, the same should happen with an electron with opposite spin, originating the supercurrent. This coherent process is sensitive to the relative electronic spin DOS or polarization at the Fermi energy. The process can be schematically observed in the upper part of figure 2.13.

In the case of a half-metallic ferromagnet, where only one spin band is occupied by the conduction electrons, no Andreev reflection process can take place, because the state for the back travelling hole does not exist (no Cooper pairs can be formed) as shown schematically in the lower part of figure 2.13.

Experimentally this is observed by measuring the conductance through the point contact. In the case of a metal whose polarization is zero, the conductance ideally doubles its intensity when the applied voltage is below the gap energy per electron charge. For half-metals whose polarization is 1, the Andreev reflection is blocked. Only single-particle states contribute to the conductance. Hence the conductance ideally becomes zero in this case when the voltage applied is below the gap energy per electron charge [104].

The relation between conductance and polarization is obtained from the adaptation of the BTK (Blonder-Tinkham-Klapwijk) theory for conventional Andreev reflection to systems where the polarization is not zero and improving the model by taking into account the effect of having non-ideal contacts. The final expression relation which better describes the system resulted in a function where the conductance is not only dependent on the polarization, but also on many other parameters such as the interface

strength Z (which gives the probability for penetration of the interface, Z=0 and Z=1 indicates 100 % and 0 % probability, respectively), the energy gap and critical temperature (which are tip pressure dependent), the parallel conductivity $G_p$ and the series resistance $R_s$ (they are due to scattering process from the tip area) [105]. Such a high number of fit parameters makes the reliability of the conclusions concerning spin polarization questionable as already demonstrated by our group [106].

- **Via Magnetic Tunneling Junction (MTJ)**

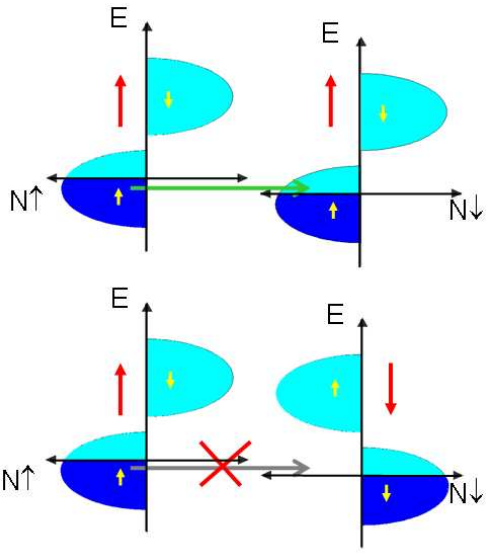


**Figure 2.14:** *Schematic representation of the tunneling process between two half-metallic ferromagnets for parallel (upper part) and antiparallel (lower part) configuration. In the parallel configuration, at the Fermi energy the electrons of both electrodes have the same spin direction, thus tunneling is allowed (low resistance). In the antiparallel configuration, the electrons of each electrode have opposite spin, thus tunneling is forbidden (high resistance).*

A MTJ is a magnetic device which is formed by two ferromagnetic materials separated by an insulating barrier. Due to tunneling effect, if a voltage is applied, a current can flow between both ferromagnets. The resistance will differ depending on the relative orientation of the magnetization of the electrodes, which is high for parallel configuration and low for antiparallel configuration, in the case where the energy gap is in the minority band.

This change in the magnetoresistance is spin polarization dependent. A simplifying sketch is shown in figure 2.14.

By applying Jullière model [4], the spin polarization of both electrodes can be indirectly obtained from the tunneling magnetoresistance (TMR) as follows:

$$TMR = \frac{R_{ap} - R_p}{R_p} = \frac{2P_1P_2}{1 - P_1P_2} \tag{2.30}$$

where $R_{ap/p}$ is the resistance in the antiparallel and parallel configuration respectively, and $P_{1/2}$ is the spin polarization of each ferromagnet.

In this simple model the barrier is treated as a passive element, it has no influence on the spin polarization of the tunneling current. The model assumes that the spin is conserved during the tunneling process and the tunneling probability is proportional to the DOS of the ferromagnets. Therefore, the spin polarization of the tunnelling current is directly related with the spin polarization of the ferromagnets.

Although it is a simple model, Jullière model can be applied for junctions with $Al_2O_3$ barriers and to combination of different ferromagnets giving consistent results. The spin polarization also would fit with Meservey and Tedrow values in their previous Ferromagnet/Insulator/Superconductor contact measurements. Theoretical calculations demonstrate that considering models of very disordered barriers, the TMR is in agreement with Jullière's formula.

Nonetheless, such a simple model is not able to explain the temperature and bias voltage dependence of the TMR ratio. Moreover, when epitaxial barriers are considered, such a model is not longer valid.

In order to have reliable results, the interface quality is of relevant importance. High quality interfaces without disorder, oxidation or impurities are needed to get the highest possible TMR value. Therefore controlling the sample, surface and interface quality is important when using this method.

By tunneling spectroscopy on MTJ, the DOS close to the Fermi energy can be observed indirectly. In tunneling spectroscopy the tunneling conductance dI/dV between the two ferromagnetic materials is measured. Although the conductance is proportional to the DOS of both ferromagnetic materials, there are other factors which contribute to the measured tunneling current. The conductance is strongly influenced by the barrier (if it grows epitaxial or amorphous, its thickness, roughness at the interface and defects). Consequently, information about the DOS of the ferromagnets can only be obtained if contributions of the barrier to the tunneling current are known. This will be discussed more in detail in chapter 6.

- **Scanning Tunneling Spectroscopy (STS)**
  STS makes use of the same quantum tunneling concept as discussed above. The tunneling current is measured by means of a Scanning Tunneling Microscope (STM) which is a technique also used to image surfaces.

  A conducting tip is brought very near to a metallic or semiconducting surface, and a bias voltage between the two allows electrons to tunnel through the vacuum between them.

  Information about the Local Density of States (LDOS) of the sample can be obtained by the resulting tunneling current as a function of the bias voltage and the tip position. A unique aspect of this technique is that information about DOS features of very small areas with $\approx$ 5Å diameter is achieved, which makes this method very useful to detect local changes of the DOS features at the surface.

  It requires sophisticated electronics, excellent vibration control, sharp tips and extremely clean and stable surfaces [107].

The aim of this work, as already mentioned in the introduction, is to evaluate the validity of predictions of half metallicity by band structure calculations for two specific Heusler compounds, $Co_2FeAl_{0.3}Si_{0.7}$ and $Co_2MnGa$, by experimental analysis of the electronic properties. Such a study is done by means of UPS and

Tunneling Spectroscopy via MTJ's.

The reasons why these two methods are used, are exposed here:
Previous works on thin films of half-metallic Heusler compounds as base electrodes on MTJ's in order to get high TMR values to demonstrate the half-metallicity have been unsuccessful, no high spin polarization could be concluded by making use of MTJ devices with the Heusler alloy as bottom electrode and amorphous $Al_2O_3$ barrier [183]. An optimization of the preparation and sample quality improved the results, but the values still remain low compared with theoretical predictions [108]. In order to find out the possible reasons which do not allow to get a higher TMR value, an experimental analysis of the band structure of these Heusler compounds which are prepared as thin films for MTJ's should be done. In this sense, tunneling spectroscopy on MTJ's is a nice option to understand the effects of the barrier shape and deformation on the tunneling current. Additionally, it is necessary to investigate which contribution to the tunneling current is due to the DOS of the half-metallic ferromagnet in the device and finally to study whether such a contribution could be observed at all. Moreover the shape of the spectra compared to simulations can give an idea of possible extra contributions not taken into account (like scattering and spin-flip processes due to impurities or roughness at the surface) in an ideal tunneling current calculation, where only contribution of the barrier shape and DOS contribute to the tunneling process.

An important aspect that influences the spin polarization is having different properties on the surface compared with the bulk. The tunneling process takes place at the interface between Heusler compound and insulator, thus it is important that half-metallicity is preserved at the surface region as well. Differences between surface and bulk mean having a different band structure at the surface which could result in a loss of half-metallicity. In order to investigate this aspect, in-situ UPS measurements directly after deposition of the Heusler thin films and annealing give important information concerning surface DOS features close to the Fermi energy. These features can be compared with theoretical predictions in order to know if half-metallicity is present. Moreover, analysis of how disorder effects electronic properties can be also studied.

# Chapter 3

# Preparation

In this work two different sort of samples are prepared. One sort consists of samples for analysis and characterization and the other consists of samples for the preparation of magnetic tunneling junctions (MTJ). This chapter focuses on the preparation of the samples for analysis and characterization. In Chapter 6, where the work on tunneling spectroscopy is shown, the preparation of MTJ will be described in detail. For a more specific and deeper explanation of the techniques, the reasons of the specific parameters, the optimization of growing, etc, the reader is referred to the PhD work of C. Herbort [108].

The samples for analysis and characterization consist of a simple stack of layers where the thin films of the Heusler compounds grow epitaxially on top of a MgO substrate with a MgO buffer layer. After surface analysis and photoemission spectroscopy measurements, the sample is protected with a thin metal layer like Al, Ag or Au for ex-situ characterization.

## 3.1 Deposition system

In this work the samples were prepared in a deposition system composed of several independently pumped chambers (figure 3.1). It consists of a molecular beam epitaxy (MBE) system, two different sputtering chambers (sputtering chamber A and sputtering chamber B), an analysis chamber for scanning tunneling microscopy (STM) and ultraviolet photoemission spectroscopy (UPS), a load-lock chamber and a transfer chamber.

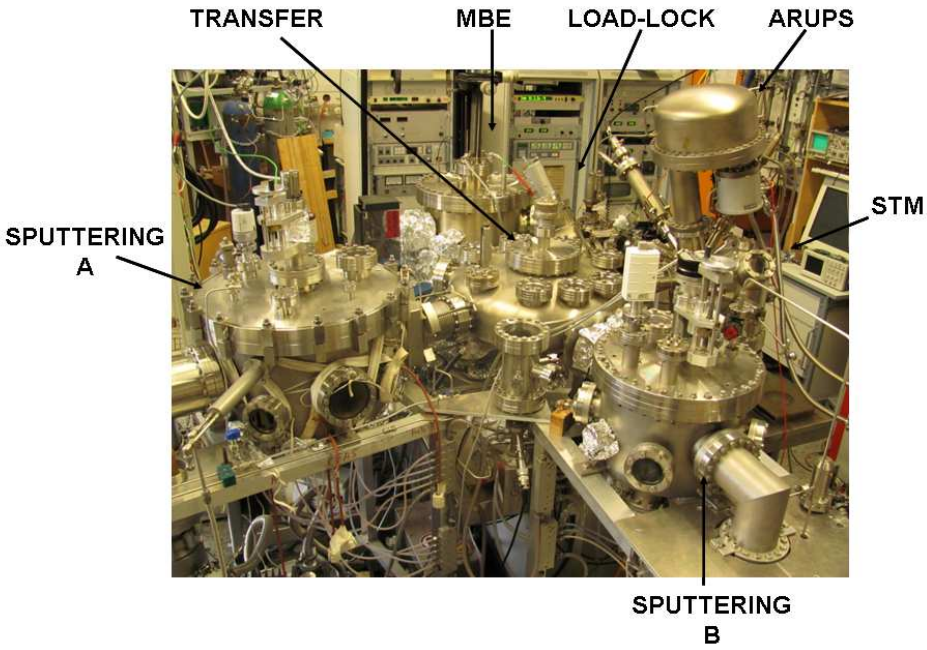


**Figure 3.1:** *Deposition system.*

The load-lock chamber is equipped with a carousel for six samples. With a transfer mechanism the sample is moved to the corresponding chambers.

In the MBE, with base pressure of $\approx 10^{-10}$ mbar, MgO buffer layers are deposited by electron beam evaporation. It has a four pocket e-beam evaporator equipped with the following materials: Al, MgO, Fe and Cr. The annealing process is also done here. The MBE possesses a *RHEED*[*] and a *LEED*[†] system which are used to study the crystallographic order and morphology of the film surface.

The depositions of different materials are performed in the sputtering chambers A and B. In both chambers the sample is placed in a holder fixed on a rotating

[*]Reflection high-energy electron diffraction (RHEED) is a technique used to characterize the surface of crystalline materials that relies on the diffraction of high-energy electrons. The energies are between 5-100 keV and the angle between the incident electron beam direction and the film surface is smaller than 5° [115].

[†]Low energy electron diffraction (LEED) is also surface sensitive, it achieves surface sensitivity by means of low energy electrons. These energies are below 1 keV and the beam incident direction is perpendicular to the surface [116].

disc which allows to move the sample to the appropriate cathode. The distance between cathode and sample for the deposition can be adjusted. For the deposition of the samples Argon gas with a 99.9999 % purity has been used. Chamber A has five sputtering cathodes with five different target materials: MnFe, Ag, CoFe, Au, and the Heusler under study at that moment ($Co_2FeAl_{0.3}Si_{0.7}$ in our case). A liquid nitrogen cold trap was used during deposition to improve the base pressure of the chamber and to remove water as contaminant. With the trap the base pressure is of the order of $10^{-9}$ mbar. Chamber B has three sputtering cathodes with Al, Mg and another Heusler material ($Co_2MnGa$ in our case) as deposition materials and one plasma oxidation cathode where the Mg-Al tunneling barriers are oxidized. The base pressure in this chamber is of the order of $10^{-9}$ mbar.

The surface topology of the films can be studied by STM in the analysis chamber as well as the electronic states by UPS. The pressure in this chamber is usually $\approx 10^{-10}$ mbar.

The pressure of the transfer chamber is in the range of $\approx 10^{-10}$ mbar.

## 3.2 Deposition Techniques

### 3.2.1 Molecular Beam Epitaxy

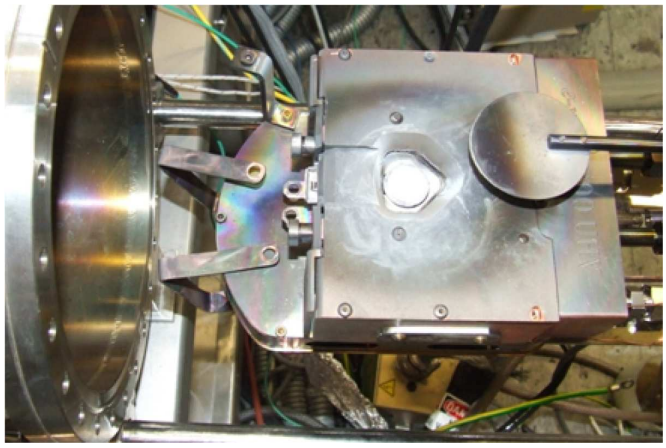

**Figure 3.2:** *Photo of the Electron Beam Evaporator with MgO in the crucible.*

This is an experimental technique to grow very thin epitaxial single crystals

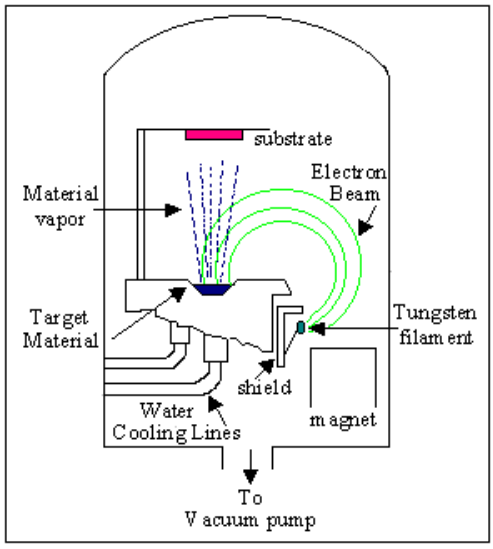


**Figure 3.3:** *Sketch of electron beam evaporation process [110].*

with as few impurities as possible. Appropriate substrate-film interaction allow the epitaxial growth. In order to reduce impurity levels as a consequence of the low deposition rate, an ultra-high vacuum (UHV) system is required (P=$10^{-10}$ mbar). The deposition is based on vacuum evaporation by which directed neutral thermal atomic and molecular beams impinge on a heated substrate under ultra-high vacuum conditions. Due to the long mean free path of the atoms, during the evaporation they do not interact with each other until they arrive to the substrate. This technique allows very good control of the layer thickness and even growth of monolayers is achieved, as well as more complicate structures with different layers of different materials [109]. The evaporation process can be done by Electron Beam Evaporation.

In this method a focused high energy electron beam is directed to the crucible, where the material for depositing is placed (see photo in figure 3.2). Due to the high energy of the electrons, the material melts and evaporates. The evaporated atoms condense on the surface of the substrate (see figure 3.3). Usually the substrate is heated to increase adatom motion.

The creation of an electron beam is due to a white hot Tungsten filament which acts as a cathode. By a high voltage the electrons are accelerated. In order to focus and control the beam trajectory, the use of magnetic field is required.

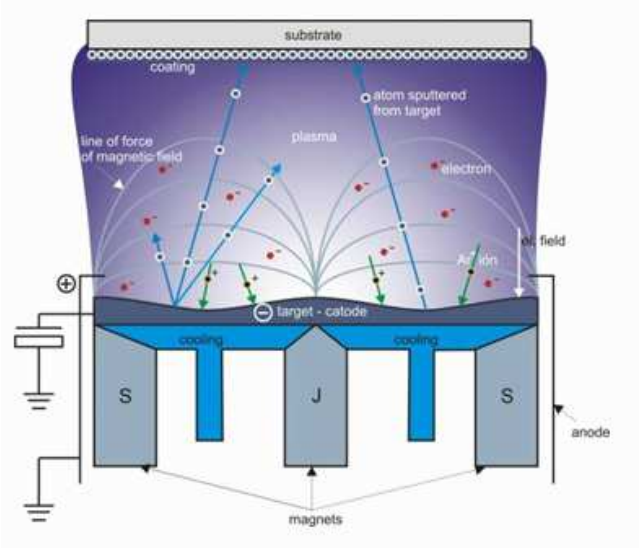


**Figure 3.4:** *Sketch of sputtering process [113].*

### 3.2.2 Sputtering

Sputtering is a process by which atoms are ejected from a solid target material due to the bombardment of the target by energetic ions. It is commonly used for thin-film deposition, etching and analytical techniques [112]. The ejection is produced by the momentum exchange, due to the collisions between the ions and the atoms of the material. It is a very efficient technique to deposit epitaxial complex system, where the composition on the substrate in principle remains the same as in the target.

Experimentally, the process consists of the following:
The cathode, on which the target material is positioned, is situated inside an ultra-high vacuum chamber in an Argon atmosphere (p≈0.1 mbar). The substrate situated face to face with the target and the chamber walls act as anodes. When a bias voltage is applied, electrons are accelerated away from the cathode and interact with the outer electron shell of the neutral gas atoms (Argon in this case), giving rise to an ionisation process. The Argon ions (positive charge) will be attracted by the cathode and they will collide with the atoms at the surface of the target. When the energy of the collision is higher than the bonding energies between the atoms in the solid, then the atoms are ejected out of the surface.

The ejected atoms are not in thermodynamical equilibrium. Thus, they tend to condensate when they get in contact with any surface. Consequently, the material is deposited on the substrate, as well as on the whole chamber wall. An scheme of the process can be observed in figure 3.4.

There are different factors that influence the sputtering efficiency: the energy and mass of the impinging ions, as well as the mass of the atoms in the solid target and their bonding energies.

In order to optimize the sputtering process for each specific material, different techniques are available in order to change the plasma properties, e.g. by changing pressure inside the vacuum chamber where the process takes place producing an increase in the element specific diffusion length in the Ar atmosphere, and hence a significantly increase on the ionization efficiency; or by making use of an alternative radiofrecuency current (RF-sputtering); or by the use of magnetic fields; or by the application of a bias potential to the target.

When the sputtering is done from multicomponent targets, the surface composition changes initially but eventually compensates the different sputtering yields of the elements. In order to achieve the right stoichiometry on the substrate the distance between target and substrate plays an important role. The diffusion length is element specific and if substrate is too far away from target, some elements would not reach the substrate while others would. Therefore no stoichiometric film will be deposited on the substrate. In an intermediate position all elements would arrive to the substrate and due to RF-current the Ar ions can also collide with the deposited atoms and a re-sputtering from the film takes place. This re-sputtering from the film can be an advantage of RF-sputtering because it improves the surface quality and crystallographic order. At the appropriate distance all deposited atoms at the surface which are more energetically unstable, which typically corresponds to atoms which do not bond to form the right stoichiometry, would be easily re-sputter. Consequently a better surface quality and a close matching of the film composition to that of the target material is achieved [114]. If substrate is placed too close to the target, the density of atoms sputtered and re-sputtered from the deposited film increase and control of surface quality and stoichiometry becomes more dificult.

The magnets allow to use low pressures. The magnetic field catches the secondary electrons close to the target. They follow the magnetic flux lines path. Hence, the ionization density increases close to the target and not in the whole chamber volume. The sputtering Ar-ion current density in that region increases and the resulting plasma can be kept at low pressures. The sputtered atoms have neutral charge, so they are not affected by the magnetic field.

The main difference between both deposition methods, MBE and sputtering, is basically the energy of the material flux reaching the substrate, E<1 eV for evaporation and E<100 eV for sputtering, and the different conditions of evaporating material.

## 3.3 Preparation procedure

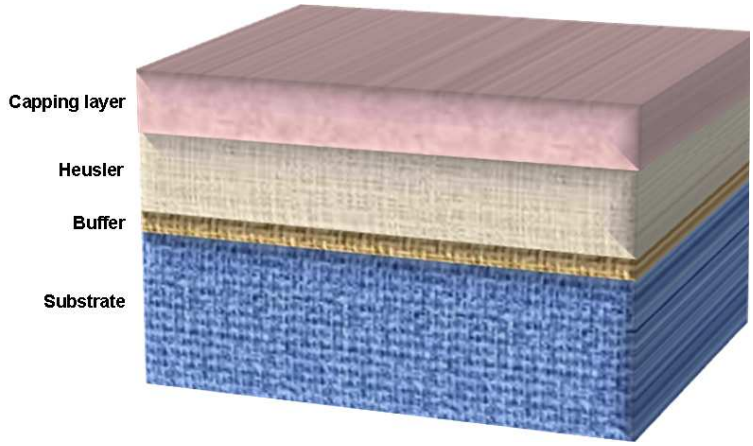


**Figure 3.5:** *Stack of layers deposited for analysis and characterization.*

### 3.3.1 Substrate preparation

The substrates used in this work are MgO (100). They come packed in a vacuum atmosphere to avoid contamination of the surface. In order to prevent as much as possible contamination from atmosphere exposure, the samples are opened and glued on the metallic holders in a *clean room*[‡]. Silver glue is used for this

[‡]A clean room is an environment, typically used in manufacturing or scientific research, that has a low level of environmental pollutants such as dust, airborne microbes, aerosol particles

process. Then, they are put in a "rough vacuum" inside the clean room for drying. After that, and as fast as possible, they are loaded in the load-lock chamber. Subsequently, the substrates are annealed in vacuum in the MBE chamber for 30 min at 650 °C. The purpose of this annealing process is the removal of surface contaminants. The substrates adopt a slightly darker, metallic color after this last step due to oxygen loss.

### 3.3.2 MgO buffer layer deposition

Thin film layers of 100 Å MgO are deposited in the MBE chamber by electron beam evaporation. This buffer layer improves the epitaxial growth of the Heusler thin films compared to a direct deposition on the MgO substrate.

The deposition method consists on the following: an electron beam with sufficient energy is directed to the MgO pieces, so that the material starts to sublimate directly without melting. This buffer layer is deposited at 400 °C and after the deposition it is cooled to 50 °C. Then, the sample is transferred to another deposition chamber where the Heusler material is deposited.

The deposition parameters are shown in appendix A.

### 3.3.3 $Co_2FeAl_{0.3}Si_{0.7}$ and $Co_2MnGa$ deposition

In the sputtering chamber A the $Co_2FeAl_{0.3}Si_{0.7}$ is deposited by magnetron rf sputtering ($Co_2MnGa$ is deposited in the same way in chamber B, as shown in figure 3.6) at room temperature.

First, 500 Å of $Co_2FeAl_{0.3}Si_{0.7}$ or $Co_2MnGa$ are deposited with deposition parameters which can be found in appendix A. Immediately afterwards, the sample is transferred to the MBE chamber for the annealing process. The annealing of the films is made in this chamber because of the lower base pressure. After annealing, the surface is studied with the RHEED system and then it is either moved to the STM chamber to analyze the surface topography of the Heusler compound or to the ARUPS chamber to study the electronic structure. The

and chemical vapours. More accurately, a clean room has a controlled level of contamination that is specified by the number of particles per cubic meter at a specified particle size. In this work a class 100 clean room is used.

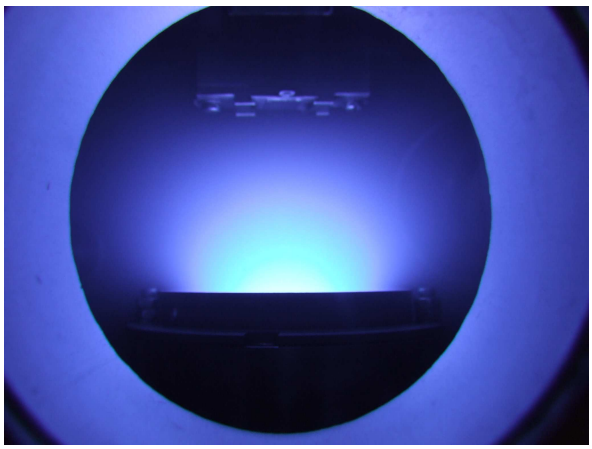

**Figure 3.6:** *Plasma during $Co_2MnGa$ deposition.*

description and analysis results obtained by RHEED, STM and ARUPS will be shown in next chapters.

The deposition parameters are shown in appendix A.

### 3.3.4 Capping layer deposition

It is worth noting that samples used for STM or ARUPS analysis are not useful for the implementation in MTJ devices due to the fact that, in spite of the ultra-high vacuum systems available, time plays an important role in degradation of the surface as it will be shown in the STM analysis in chapter 6. For a MTJ, a very good surface quality is required in order to get reliable results. Furthermore, these samples are not useful for ex-situ surface characterization, like the analysis of magnetic properties at the surface by XMCD (X-Ray Magnetic Circular Dichroism). In this particular case, after the annealing process, the samples have to be covered by the insulator forming the tunneling barrier in the case of MTJ preparation, or have to be protected by an Al capping layer, in the case of posteriori XMCD analysis.

Later on, the samples for STM or ARUPS can be used for ex-situ characterization of the bulk properties. Once the in-situ analysis is finished, the sample is transferred to the sputtering chamber B where 20 Å Al as capping layer are deposited by sputtering as capping layer. The capping layer will protect the sam-

ple from contaminants and oxidation when it is exposed to normal atmosphere conditions.

The deposition parameters are shown in appendix A.

# Chapter 4

# Characterization

In this chapter all techniques used to study different properties that characterize the $Co_2FeAl_{0.3}Si_{0.7}$ and $Co_2MnGa$ Heusler compounds grown as thin films are presented. Such studies are divided in two parts: One part corresponds to the bulk crystallographic and magnetic properties while the other corresponds to the surface crystallography and magnetometry, which could differ from the bulk. Photoemission and tunneling spectroscopy are surface and interface dependent, respectively. Hence the importance of controlling the surface properties. Crystallographic disorder, impurities and roughness at the surface influence the measured electronic properties. Therefore an interpretation of the results is not possible without control of the quality and characteristic of the $Co_2FeAl_{0.3}Si_{0.7}$ and $Co_2MnGa$ Heusler thin films. In addition, the dependence of the electronic properties on the crystallographic disorder was studied by photoemission measurements. Different types of disorder are achieved via changing the annealing temperature.

## 4.1 Bulk properties

### 4.1.1 X-ray diffraction

In order to investigate the bulk crystallographic properties (crystalline structure, impurity phases, preferential orientation, degree of disorder, thickness of the layers, roughness, lattice mismatch between film and substrate, mosaicity, coherence length scattering volume and quality) of the $Co_2FeAl_{0.3}Si_{0.7}$ and $Co_2MnGa$ Heusler thin films, X-ray diffraction is used.

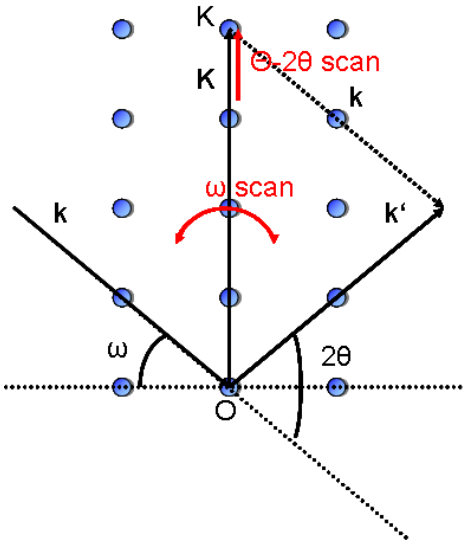


**Figure 4.1:** *Laue condition for X-ray diffraction*

This technique is a non-destructive method of sample characterization based on the analysis of diffracted X-rays (which contain relevant crystallographic information) from a sample.

The reason why X-rays are used as an electromagnetic probe of the microscopic structure of a solid is their energy range, which corresponds to a wavelength of the same order of magnitude as interatomic distances in a solid, around 1 Å. Constructive interference of monochromatic X-rays from a crystalline sample is the basis of X-ray diffraction, which occurs when the change in wave vector, **K**=**k'**-**k**, is a vector of the reciprocal lattice (Laue condition), see figure 4.1 [117].

The diffracted amplitude represented as a function of **K** in reciprocal space is the Fourier transform of the electron density of a finite crystal and is defined as

$$I(\mathbf{K}) = |F(\mathbf{K})|^2 = |\sum_{j=1}^{n} f_j exp(-2\pi i \mathbf{K} \cdot \mathbf{r}_j)|^2 \tag{4.1}$$

$F(\mathbf{K})$ is the structure factor, the sum is extended to all the atoms of the unit cell, **K** is a vector of the reciprocal space which correspond to the difference of the incident and scattered wave vector (Laue condition), $\mathbf{r}_j$ is the position of the atom j in the unit cell defined in terms of the three fundamental vectors **a**, **b**, **c**,

and $f_j$ is the element specific atomic scattering factor, defined as

$$f_j = \int \rho_{c,j}(\mathbf{r}) exp(-2\pi i \mathbf{K}\cdot\mathbf{r}) dv \tag{4.2}$$

$$\rho_c(\mathbf{r}) = \rho(\mathbf{r}) * [z(\mathbf{r})\sigma(\mathbf{r})] \tag{4.3}$$

$\rho_c$ is a triply periodic function, the three periodicities being defined by the three fundamental vectors **a**, **b**, **c** on which a unit cell is built, $\rho(\mathbf{r})$ is the electron density inside the unit cell, $z(\mathbf{r})$ is a function which describes the lattice by a series of Dirac functions centered on the lattice points, and $\sigma(\mathbf{r})$ is the form factor which defines the exterior shape of the object (equal to unity inside the sample volume and zero outside).

The expression $I(\mathbf{K})$ is non-zero if **K** satisfies the three conditions ($\mathbf{K}\cdot\mathbf{a} = h$, $\mathbf{K}\cdot\mathbf{b} = k$, $\mathbf{K}\cdot\mathbf{c} = l$) and h, k and l are simultaneously whole numbers. Within these conditions a relation between the structure of the crystal and its reciprocal space is established. (hkl) are the so-called Miller indices. For those Miller indices for which $I(\mathbf{K})$ is non-zero a Bragg reflection takes places [118].

Heusler compounds $X_2YZ$ are described as four interpenetrating fcc sublattices A, B, C and D, corresponding A and C sites to X atoms, B sites to Y atoms and D sites to Z atoms for a perfect order. This structure gives rise to non-zero Bragg reflections only when the Miller indices of the scattering planes are either all even, or all odd. The intensities of these reflections are determined by the squares of the structure factors. The structure factors for the three main Bragg reflections are [119]:

$$\begin{aligned} h,k,l \quad & F(111) = |4[(f_A - f_C)^2 + (f_B - f_D)^2]^{\frac{1}{2}}| \\ (h+k+l)/2 = 2n+1 \quad & F(200) = |4[f_A - f_B + f_C - f_D]| \\ (h+k+l)/2 = 2n \quad & F(220) = |4[f_A + f_B + f_C + f_D]| \end{aligned}$$

With the well known Bragg's law a relation between Bragg's reflections (hkl) and the diffraction angles $\theta$ in the real space is given:

$$sin\theta = \frac{\lambda\sqrt{h^2+k^2+l^2}}{2a} \tag{4.4}$$

For the crystallographic characterization of the samples a two-circle diffractometer and a four-circle diffractometer were used in this work for different applications. The basic elements of an X-ray diffractometer are: X-ray tube where

X-rays are generated, sample holder where the sample is positioned and X-ray detector where X-rays are counted.

**2-circle diffractometer**

In this setup the samples are measured in Bragg-Brentano geometry (divergent incident beam) [121] and scattering takes place in a plane perpendicular to substrate surface. The cathode, the sample and the detector are in one plane. The geometrical angles which are part of this measurement are: the diffraction angle $2\theta$, which is the angle between the incident beam and the detector; the incident angle $\omega$ ($\approx \theta$), which is the angle between the incident beam and the surface plane (see figure 4.1); and the offset angle $\beta$, which is a correcting angle between the surface plane and the sample holder plane.

- **Reflectometry**
  Reflectometry is a surface sensitive technique used to determine the thickness of a thin layer, or different thicknesses of a multilayer sample, surface and interface roughness and the density of each layer in the system.

  It is based on the coplanar scattering of X-ray radiation around the reciprocal lattice point (000).

  The reflectometry profile shows the scattered X-ray intensity dependent on the incidence angle (or reciprocal lattice vector q). For X-rays the refractive index of a solid is lower than the refractive index of air. As a consequence, for incident angles smaller than the critical angle (angle at which total external reflection occurs) all incident X-rays are totally reflected. For incident angles bigger than the critical angle, part of the incident beam penetrates into the medium and the intensity decreases on increasing the angle of incidence. Oscillation, named Kiessig fringes, of the intensity occurs due to the interference of X-rays reflected from different interfaces, of layers and multilayers. From the periodicity of these oscillations information about the thickness of the different layers is obtained. From their amplitude, information about surface and interface roughness is achieved [120, 122].

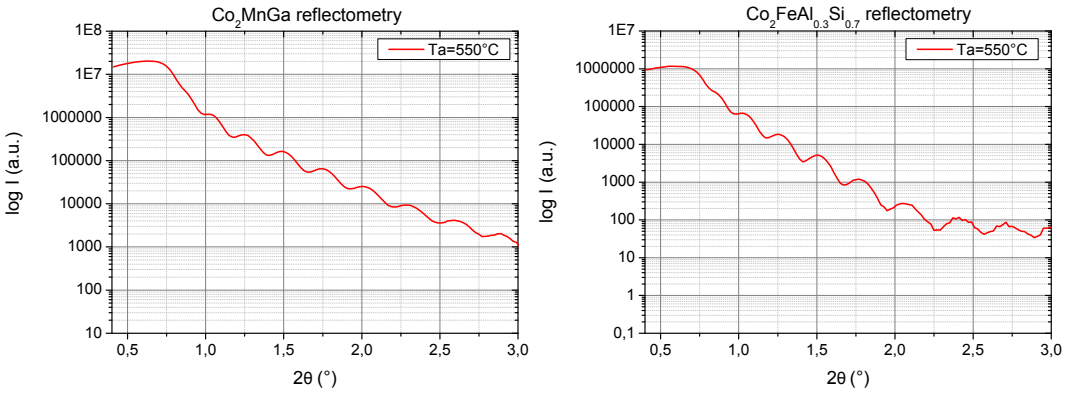


**Figure 4.2:** ***Left:*** *Reflectometry curve of a 321 Å $Co_2MnGa$ thin film annealed at 550 °C.* ***Right:*** *Reflectometry curve of a 303 Å $Co_2FeAl_{0.3}Si_{0.7}$ thin film annealed at 550 °C.*

The experimental reflectometry curves for a $Co_2MnGa$ and a $Co_2FeAl_{0.3}Si_{0.7}$ thin film annealed at 550 °C are shown in figure 4.2 left and right, respectively. $(\theta/2\theta)$-scans at low $2\theta$ angles between $\simeq 0.3°$ and $\simeq 3°$ are performed. Plotting the detected intensity against $2\theta$, the profile described before is observed. The film thickness and roughness are deduced from the periodicity and the amplitude of the oscillations, respectively.

The reflectometry curves show clear and well defined maxima. This indicates a smooth surface of the samples. From the periodicity of the maxima or minima observed, the thickness of a sample can be calculated. If just a thin film of one sort of material is on top of the substrate, by means of Bragg's law, an approximated value for the thickness can be determined. The method consists of plotting the number of consecutive maxima or minima versus their corresponding angle $\sin\theta$ and using Bragg's law $(m\lambda = 2dsin\theta)$, the thickness can be obtained from the slope of the linear fit of these points. Doing this for our specific $Co_2MnGa$ and $Co_2FeAl_{0.3}Si_{0.7}$ samples results in a thickness of 321 Å and 303 Å for samples deposited within 18 min 31 s and 45 min, respectively. Using Bragg's law is a first approach for thickness calculation. It can only be used for single layers and it does not take into account the refraction of the X-ray beam when it penetrates into the solid, as it is illustrated in figure 4.3. The difference on the optical path between two X-ray beams in a refractive medium differs from a non refractive medium and therefore, the thickness which is obtained

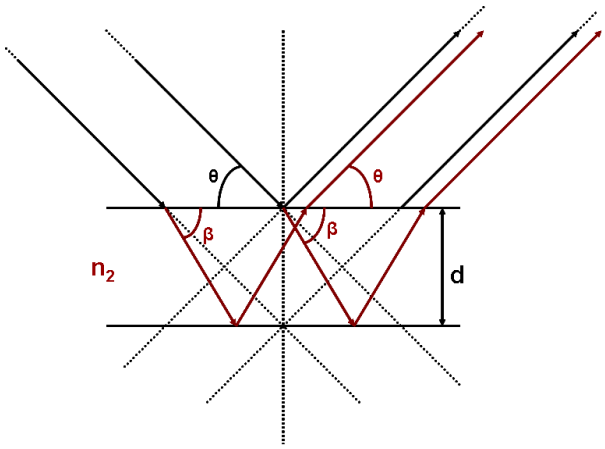


**Figure 4.3:** ***Left:*** *Refraction of the X-rays beams between two different mediums.* $n_1$ *is the refraction index in air and* $n_2$ *is the refraction index in the material. In Bragg's law approach:* $n_1 \approx n_2$ *and* $\theta = \beta$.

by considering no refraction (Bragg's law) differ from the real situation in which refraction takes place.

For complex layered structures, the interpretation of the reflectometry profile is more complicated and the information of thickness, roughness and density is obtained by a modelling and fitting procedure. The standard program used in this cases is the PARRAT32 software [123].

- **$\omega$-scan**
  An $\omega$-scan is performed by rocking (varying $\omega$) the sample around a fixed $2\theta$ angle which corresponds to a characteristic lattice plane of the crystal under study, for example the (200) or the (400) planes, which are characteristic for Heusler compounds (see figure 4.1).

  The rocking curve ($\omega$-scan) contains information about the mosaicity and the correlation length (due to atomic disorder or finite size effects) of the film. If the growth of the sample was ideal and perfect the rocking curve observed would be a delta function. Nevertheless, due to imperfections and instrument resolution broadening appears. Comparing the width of the (200) and (400) peaks (specular Bragg reflections of increasing order), it can be deduced which kind of broadening mechanism predominates in

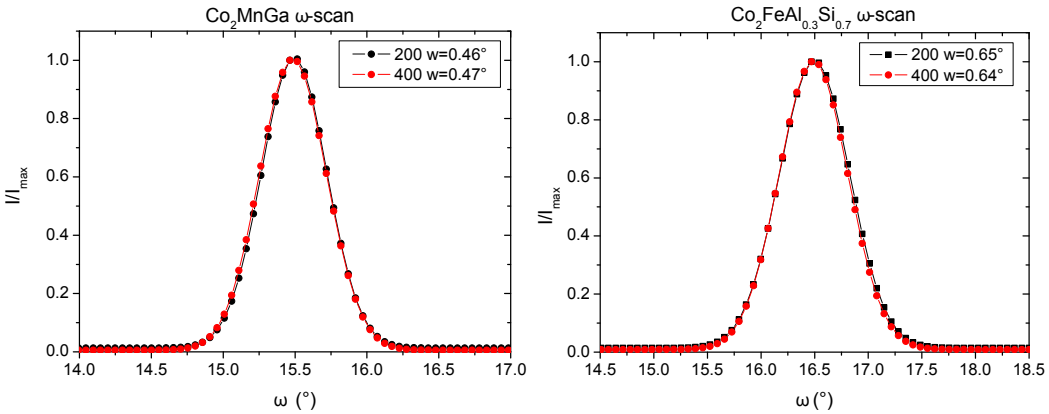


**Figure 4.4:** *ω scans of the specular (200) and (400) peaks of a 321 Å $Co_2MnGa$ thin film (left) and a 303 Å $Co_2FeAl_{0.3}Si_{0.7}$ thin film (right). The ω axis of the (400) reflection is shifted to display the scans on top of each other.*

the sample. When the width of both peaks is the same or almost the same, mosaicity is more relevant, but if the width of the higher order peak is significantly more narrow a relatively short lateral correlation length ($\simeq$ 100 nm) is the origin of the rocking curve broadening [124]. Comparing the width of the (200) and (400) rocking curves for $Co_2MnGa$ and $Co_2FeAl_{0.3}Si_{0.7}$ thin films on figure 4.4, left and right, the same width for both reflections is obtained. This indicates that, in both cases, the predominant broadening effect is crystal mosaicity. Comparing the width obtained for the two different compounds, $Co_2MnGa$ and $Co_2FeAl_{0.3}Si_{0.7}$ values of 0.46° and 0.64° are obtained, respectively. Therefore, crystal mosaicity is stronger in $Co_2FeAl_{0.3}Si_{0.7}$ Heusler thin films.

- **$\theta$-$2\theta$ scan**
  In a $\theta$-$2\theta$ scan, the detector moves around a circle and the sample is tilted in the center of this circle. Therefore, the X-ray beam is scattered from crystal planes parallel to substrate surface (see figure 4.1).

  Taking into account that the angular position of the oriented planes for a specific compound with an ordered and specific crystallographic structure is a priori known, from the measured peak positions information about the phase formation, stress and impurity phases is obtained, as well as information about the type and degree of disorder of the film. In the particular case of $Co_2MnGa$ and $Co_2FeAl_{0.3}Si_{0.7}$ Heusler compounds, a $L2_1$ crystallographic

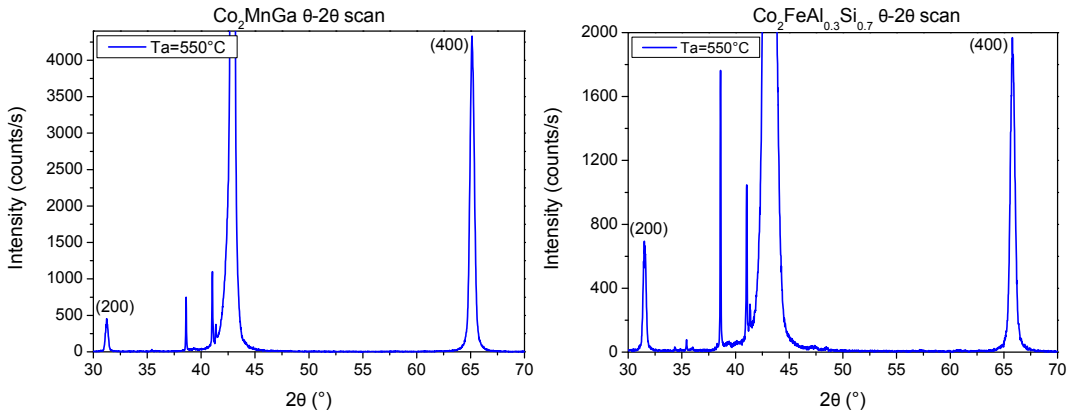


**Figure 4.5:** *θ-2θ scans of a 321 Å $Co_2FeAl_{0.3}Si_{0.7}$ thin film (left) and a 303 Å $Co_2MnGa$ thin film (right) annealed at 550 °C. (200) and (400) reflections are clearly visible as an indication of a B2 structure spectrum.*

structure is expected. The (400) and (200) are characteristic reflections of Heusler compound structures and they indicate crystallographic order of the perpendicular oriented planes, i.e. order between Co and Fe-(Al,Si) or Mn-Ga planes, for $Co_2FeAl_{0.3}Si_{0.7}$ and $Co_2MnGa$ respectively. The intensity ratio between both reflections (200) and (400) gives an indication of the degree of disorder present when comparing with theoretical simulations. Such an analysis is exposed in section 4.1.2. discussing the degree of disorder. *θ-2θ* scans for $Co_2MnGa$ and $Co_2FeAl_{0.3}Si_{0.7}$ thin films annealed at 550 °C are shown in figure 4.5, left and right, respectively. For both compounds, the presence of (400) and (200) reflection is noticeable. From this analysis, ordering between Co and Fe-(Al,Si) planes for $Co_2FeAl_{0.3}Si_{0.7}$ Co and Mn-Ga planes for $Co_2MnGa$ is concluded.

### 4-circle diffractometer

As already mentioned, with a two circle diffractometer it is only possible to study specular reflections, i.e. reflections for which the transferred momentum vector is perpendicular to the film surface. Consequently, a four-circle diffractometer was employed to study off-specular reflections in order to analyse the in-plane order of the films and to investigate the (111) diffraction peak, which is characteristic for the ordered $L2_1$ structure, more precisely for the degree of order on the Fe-Al/Si sites.

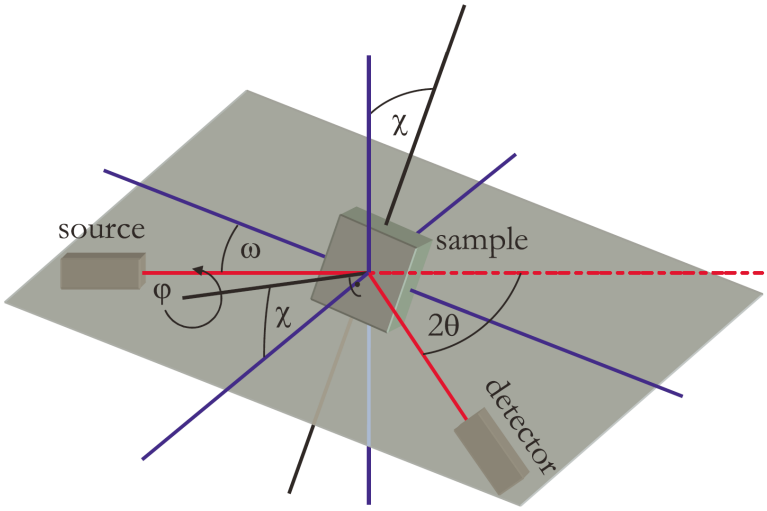


**Figure 4.6:** *Geometry of a X-ray diffraction experiment in a 4 circle diffractometer. $\omega$ is the beam incident angle, the detector moves in $\theta$ direction. Moreover the sample can rotate ($\varphi$) and tilt ($\chi$).*

The geometry of a four circle diffractometer is shown in figure 4.6. The four independent angles are $\varphi$, $\chi$, $\theta$, $\omega$. Here, not only the detector moves in $\theta$ direction, but also the sample can be rotated ($\varphi$) and tilted ($\chi$) allowing the investigation of all the reflections in the sample.

- **Collection of X-ray peaks and determination of lattice parameters**
  A collection of the main Bragg reflections which characterize the crystallographic structure of Heusler compounds is carried out. For this purpose, the determination of two reflections in different planes is required, for example the (400) and (220) peaks. The goniometer moves to their angular positions and their maxima are centered. Thus, having these two peaks as reference, the rest of the Bragg reflections and the lattice parameters of the crystal can be determined.

  As a result, the following lattice parameters for $Co_2FeAl_{0.3}Si_{0.7}$ are obtained:

| **Angle** | **Value (°)** | **Lattice constant** | **Value (Å)** |
|---|---|---|---|
| $\alpha$ | 90.00±0.14 | A | 5.67±0.01 |
| $\beta$ | 90.00±0.11 | B | 5.66±0.01 |
| $\gamma$ | 90.00±0.11 | C | 5.66±0.01 |

For the case of $Co_2MnGa$ the measured lattice parameters are the following:

| **Angle** | **Value (°)** | **Lattice constant** | **Value (Å)** |
|---|---|---|---|
| $\alpha$ | 90.00±0.16 | A | 5.71±0.01 |
| $\beta$ | 89.91±0.13 | B | 5.84±0.01 |
| $\gamma$ | 90.05±0.13 | C | 5.84±0.01 |

The MgO substrate lattice parameters are also measured. The results are:

| **Angle** | **Value (°)** | **Lattice constant** | **Value (Å)** |
|---|---|---|---|
| $\alpha$ | 89.99±0.11 | A | 4.20±0.01 |
| $\beta$ | 90.03±0.09 | B | 4.23±0.01 |
| $\gamma$ | 90.02±0.09 | C | 4.23±0.01 |

The errors given do not include systematic errors due to sample misalignment. The A lattice constant, which correspond to the out of plane lattice vector, differs from B and C in-plane lattice constant. This effect is simply due to a systematic error which comes from a non-optimal height adjustment of the sample in the sample holder of the goniometer. The same lattice constant values together with the three 90° angles on the three different directions indicate that the unit cells are simple cubic.

For $Co_2FeAl_{0.3}Si_{0.7}$ the (111) reflections were found for all samples annealed above 550 °C. For $Co_2MnGa$ the (111) reflection was found at 550 °C.

It is worth pointing out that the x-ray scattering cross sections scale with the atomic mass. Thus there is almost no contrast between scattering from Co and Fe and disorder between those elements, called DO3 disorder, can not be distinguished from $L2_1$ order by standard X-ray diffraction.

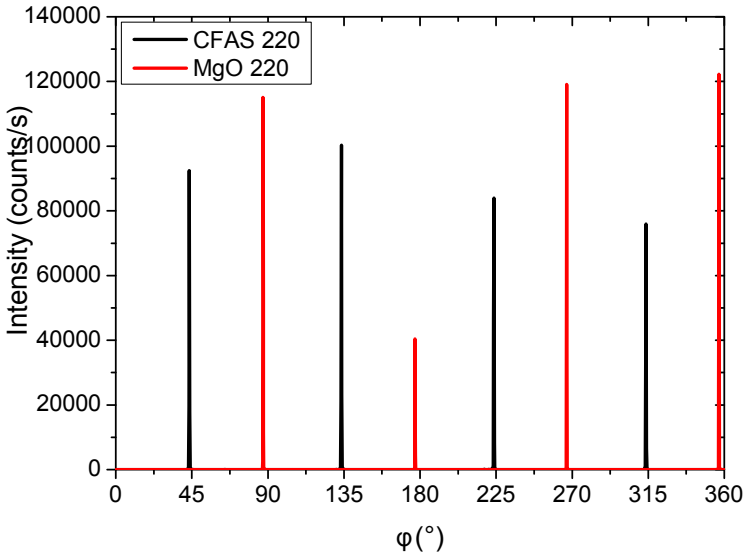


**Figure 4.7:** *X-ray $\phi$-scan of the (220) equivalent reflections of a $Co_2FeAl_{0.3}Si_{0.7}$ film ($2\theta$=43.49°, $\chi$=-45.56°) annealed at 550 °C (black) and of the MgO substrate (red) ($2\theta$=62.42°, $\chi$=-45.19°). The different intensities are due to an offset angle between the surface plane and the sample holder plane.*

- **$\phi$-scan**

  Furthemore, the in-plane orientation of the films with respect to the substrate or buffer layer was also determined via X-ray diffraction in the four-circle diffractometer. In a $\phi$-scan the sample is rotated around the substrate normal at constant momentum transfer q with $\vec{q}$ describing a circle in reciprocal space. The intersections of this circle with the points of the reciprocal lattices causes diffraction peaks to occur at the corresponding $\phi$ angles. A $\phi$-scan of the (220) $Co_2FeAl_{0.3}Si_{0.7}$ thin film is plotted together with a $\phi$-scan of the (220) MgO substrate in figure 4.7. As can be observed the diffraction peaks of the Heusler thin film are displaced by 45° with respect to the MgO substrate, indicating that the film grows epitaxially tilted by 45° on the MgO substrate. The same behaviour is found for $Co_2MnGa$. A sketch is shown in figure 4.8.

  From the lattice constants obtained from the diffraction experiments for MgO, $Co_2FeAl_{0.3}Si_{0.7}$ and $Co_2MnGa$ and given that the Heusler films grow tilted by 45° on MgO substrates, the lattice mismatch for $Co_2FeAl_{0.3}Si_{0.7}$ and $Co_2MnGa$ on MgO can be determined. The length of the MgO diago-

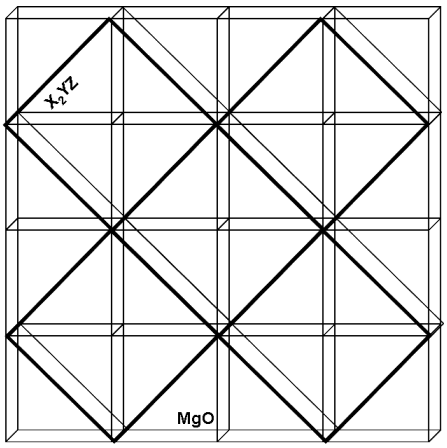


**Figure 4.8:** *Schematic representation of the epitaxial growth of $Co_2FeAl_{0.3}Si_{0.7}$ or $Co_2MnGa$ thin films on a MgO (100) substrate.*

nal is 5.94 Å. Lattice mismatch is defined as $\Delta a/a = (a - a_0)/a$, where a and $a_0$ are the material and substrate lattice constants, respectively. The lattice mismatch values for $Co_2FeAl_{0.3}Si_{0.7}$ and $Co_2MnGa$ corresponding to $-4.9 \times 10^{-2}$ and $-2.6 \times 10^{-2}$, respectively are found.

- **Q-scan**
  In a Q-scan, a scan is defined along a line or within a plane of reciprocal space. Hereby, $\vec{q}$ is varied and all points of the reciprocal lattice lying in this reciprocal space segment occur as reflections. Plane-scans parallel and line-scans perpendicular to the substrate surface are carried out.

  As well for $Co_2FeAl_{0.3}Si_{0.7}$ as for $Co_2MnGa$ an increase of intensity is found at the (111) position. This scan allows to determine the (111) reflection intensity and its width and compare it with the (200) reflection in order to estimate the degree of disorder of the films. This is discussed in the following subsection.

### 4.1.2 Degree of disorder

Disorder on the positions of the atoms in the crystallographic structure of $Co_2FeAl_{0.3}Si_{0.7}$ can destroy half-metallicity as already discussed in the subsection 1.3.4 “Effect of disorder” of chapter 1. Therefore, it is important to quantify the

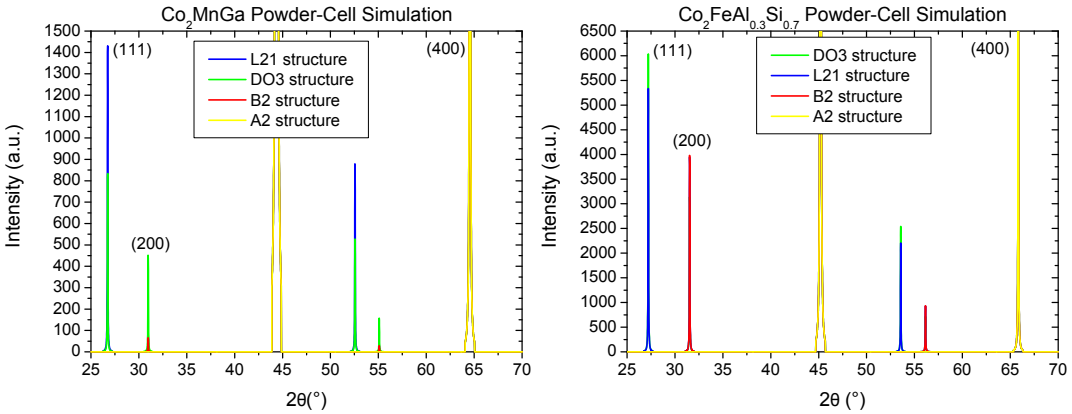


**Figure 4.9:** *Powder-Cell simulation spectra of a $Co_2MnGa$ (left) and a $Co_2FeAl_{0.3}Si_{0.7}$ (right) Heusler compound with four different crystallographic structures: DO3 structure (green), $L2_1$ ordered structure (blue), B2 structure (red), A2 (yellow).*

degree of disorder of these films.

The software **"Powder Cell"** [125] was used. It simulates X-ray diffraction for powder samples providing the peak positions and relative intensity distribution of the different reflections of the desired crystalline structure.

A powder simulation of the diffraction peaks of the four different crystalline structures for $Co_2MnGa$ and $Co_2FeAl_{0.3}Si_{0.7}$ is shown in figure 4.9, left and right, respectively: DO3, $L2_1$, B2 and A2 structures. The type of disorder can be obtained by analysing the (111), (200) and (400) reflections. So, when there is complete disorder between Mn-Ga atoms or Fe-Al/Si atoms (B2 structure) the (111) reflection can not be observed (red spectrum). If the disorder appears between Co-Mn atoms (DO3 structure) the (111) reflection decreases and the (200) reflection increases for $Co_2MnGa$ while for $Co_2FeAl_{0.3}Si_{0.7}$ it happens the opposite. This difference is due to the different electron density of Ga and Al, which determines the scattering cross sections. Moreover, if there is an additional Co-(Mn, Ga) disorder or Co-(Fe, Al/Si) (A2 structure) the (200) reflection also vanishes as it is shown in the yellow spectrum.

In order to determine the kind of disorder that is in the films, a comparison of the experimentally determined peaks with the simulations has to be done.

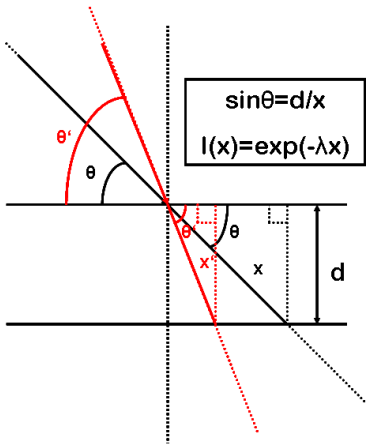


**Figure 4.10:** *Schematic view of the X-ray beam trajectory depending on the incident angle. No refraction between the two mediums is taken into account.*

A direct quantitative comparison of the diffraction intensities is not possible because of different reasons. First, the simulation is based on calculations for bulk materials where all X-rays are diffracted in the material, while for thin films this is not the case because most of the X-rays penetrate the thin film without being scattered. Since the path of the X-rays within the thin film is longer for small angles of incidence (see figure 4.10), the effective scattering volume and thus the diffraction peak intensity is increased for those angles. This effect can be approximately corrected by normalizing the X-ray intensity to the X-ray path length in the sample. However, this correction overestimates the intensity of the small angle peaks, because it does not consider the exponential decrease of the X-ray intensity within the sample.

For a disorder estimation, the evolution of the ratio between two reflections has to be studied as a function of an external parameter of disorder and compared with the simulation. The experimental ratios can also be determined as a function of annealing temperature and, by comparing its evolution with the simulated one, the type of order which is being induced by changes of the annealing temperature can be determined. It is important to mention, that the observation of the (111) reflection does not imply a direct affirmation of $L2_1$ order. The (111) reflection is also characteristic for DO3 disorder. It is the evolution of this peak together with the evolution of the (200) reflection which determines which kind of structure is present in the films. In the particular case of $Co_2FeAl_{0.3}Si_{0.7}$ an

additional inconvenient has to be taken into account. The x-ray scattering cross sections scale with the electron density. Thus there is almost no contrast between scattering from Co and Fe and disorder between those elements is difficult to detect by standard X-ray diffraction.

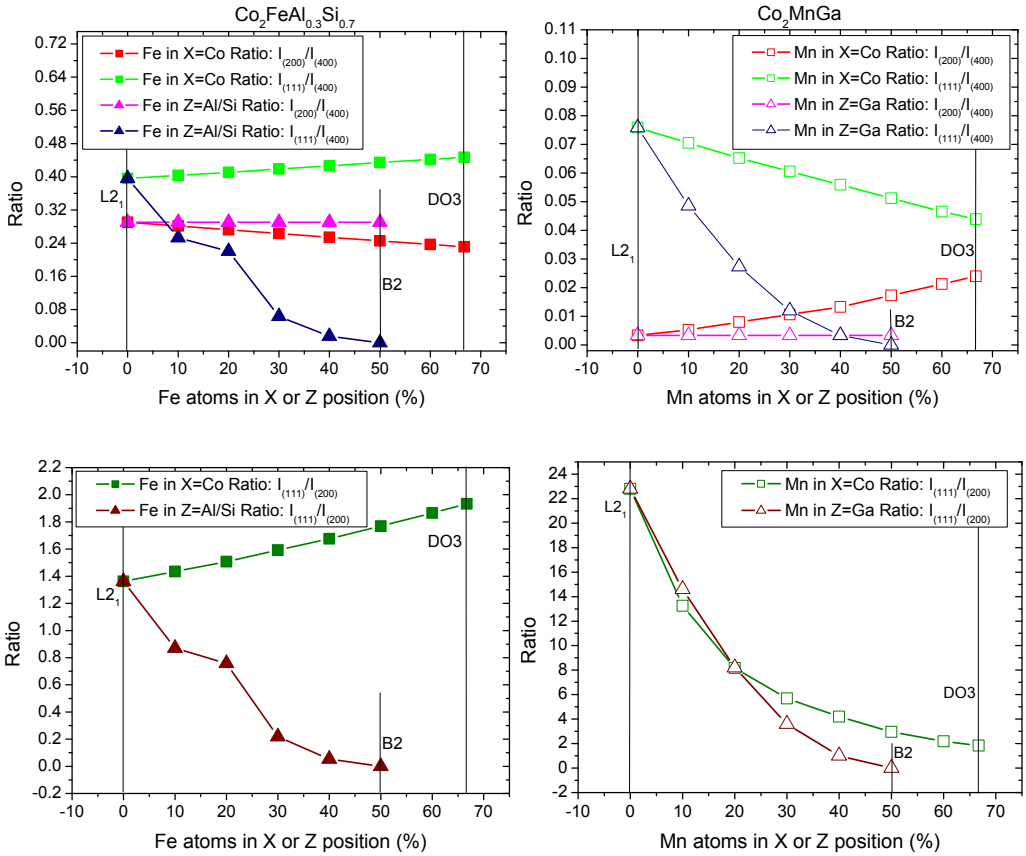


**Figure 4.11:** *Evolution of the simulated ratios for different types and degree of disorder (in percentage).* ***Top:*** *Ratios of the (111) and (200) peaks with respect to (400) peak for two different types of disorder for $Co_2FeAl_{0.3}Si_{0.7}$ (left) and $Co_2MnGa$ (right): Y atoms occupying Z position (full and open triangles, respectively), and Y atoms occupying X position (full and open squares, respectively).* ***Bottom:*** *Ratios of the (111) peak with respect to the (200) for the two different types of disorder for $Co_2FeAl_{0.3}Si_{0.7}$ (left) and $Co_2MnGa$ (right): Y atoms occupying Z position (full and open triangles, respectively), and Y atoms occupying X position (full and open squares, respectively).*

The evolution of the simulated ratios for different types and degree of disorder are plotted and shown in figure 4.11. In the two top graphs the ratios of the (111)

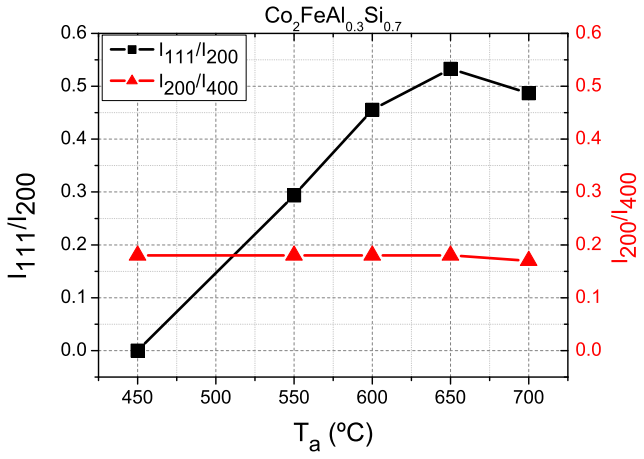


**Figure 4.12:** *Experimental evolution of the ratios $I_{(200)}/I_{(400)}$ and $I_{(111)}/I_{(200)}$ with the annealing temperature for $Co_2FeAl_{0.3}Si_{0.7}$ thin films.*

and (200) peaks with respect to (400) peak (this peak remains always constant) for two different types of disorder for $Co_2FeAl_{0.3}Si_{0.7}$ (left) and $Co_2MnGa$ (right) are presented. One type of disorder consist of Y atoms occupying Z position, i. e. Fe in Al/Si position for $Co_2FeAl_{0.3}Si_{0.7}$ and Mn in Ga position for $Co_2MnGa$ which is symbolized by triangles, full and open, respectively. The maximum degree of disorder, where 50 % of Y atoms occupy Z positions, is the so called B2 structure. The other type of disorder consist of Y atoms occupying X position, i. e. Fe on Co positions for $Co_2FeAl_{0.3}Si_{0.7}$ and Mn on Co positions for $Co_2MnGa$ which is symbolized by squares, full and open, respectively. The maximum degree of disorder in this case, where 66.7 % of Y atoms occupy X position, is the so called DO3 structure. In the two bottom graphs the ratios of the (111) peak with respect to the (200) are shown for the two different types of disorder for $Co_2FeAl_{0.3}Si_{0.7}$ (left) and $Co_2MnGa$ (right). Every graph shows the evolution of the peak ratios with the degree of disorder in percentage. Every ratio evolution starts with a completely ordered structure where each atom is at its corresponding position $X_2YZ$, i. e. 0 % for both types of disorder and finishes with the maximal degree of disorder for each type, B2 or DO3.

For $Co_2FeAl_{0.3}Si_{0.7}$ when Fe atoms occupy Z position a decrease of the (111) peak is observed and it vanishes completely with maximum disorder. The (200)

peak remains always constant for this type of disorder. When Fe atoms occupy X positions an increase of the (111) peak is observed together with a slightly decrease of the (200) peak. The DO3 disorder is difficult to distinguish from $L2_1$ order because, as can be seen in the graph, its evolution can also be confuse with an improvement of $L2_1$ order.

For $Co_2MnGa$ if Mn atoms occupy the Z position the same evolution as for $Co_2FeAl_{0.3}Si_{0.7}$ takes place. A decrease of the (111) peak is observed and it vanishes completely with maximum disorder. The (200) peak remains always constant for this type of disorder. However, when Mn atoms occupy X positions, a decrease of the (111) peak is observed together with an increase of the (200) peak. In this case the DO3 disorder can be distinguished by observing a decrease of the (111) peak while the (200) peak increases simultaneously.

Experimentally, the evolution of the ratios $I_{(200)}/I_{(400)}$ and $I_{(111)}/I_{(200)}$ with the annealing temperature was investigated for $Co_2FeAl_{0.3}Si_{0.7}$ thin films. The $I_{(200)}/I_{(400)}$ ratio was calculated with the $\sin(\theta)$ correction factor:

$$Ratio = R_{2/4} = I_{200}.sin(\theta_{200})/I_{400}.sin(\theta_{400}) \tag{4.5}$$

The $I_{(111)}/I_{(200)}$ was obtained from integrating the complete intensity of each peak in q-space. This process was done by scanning in q-space a plane for obtaining a cross section of the ellipsoid and a line for obtaining its maximum. We assume the ellipsoid is long-axis oriented, parallel to surface normal.

The results are shown in figure 4.12. The ratios $R_{2/4}$ (red triangular symbols) keep constant. A tiny decrease of this ratio is observed at 700 °C. For the ratio $I_{111}/I_{200}$, however, stronger changes appear. An increase of this ratio with raising annealing temperature is observed. It goes from 0 (no (111) peak) at 450 °C to 0.53 at 650 °C (maximum (111) peak). The (111) peak appears at 550 °C. A decrease of this ratio is observed at 700 °C. From this evolution and comparing with the simulations shown in figure 4.11, a crystallographic order improvement from B2 to $L2_1$ can be concluded. It starts from B2 disorder (50 % of Fe on Al/Si sites) at 450°C, and it finish with a higher degree of order on the Fe sites (less percentage of Fe on Al/Si sites) at 650 °C. Full $L2_1$ order can not be proven by our analysis methods due to the limitations of geometrical corrections. Additionally, some degree of DO3 disorder can not be excluded. Nevertheless,

theoretical predictions, shown in figure 2.11, claim the $L2_1$ structure to be energetically more favourable to be formed for the composition $Co_2FeAl_{0.3}Si_{0.7}$ than DO3 which would cost much more energy. Therefore an improvement on the $L2_1$ ordering direction is more probable.

For $Co_2MnGa$ the experimental ratios, $R_{2/4}$ and $I_{(111)}/I_{(200)}$ result on 0.05 and 0.93, respectively, for a film annealed at 550 °C. The evolution of disorder due to variation of annealing temperature was not investigated. However, similar behaviour as in the $Co_2FeAl_{0.3}Si_{0.7}$ case is expected.

### 4.1.3 Magnetic properties

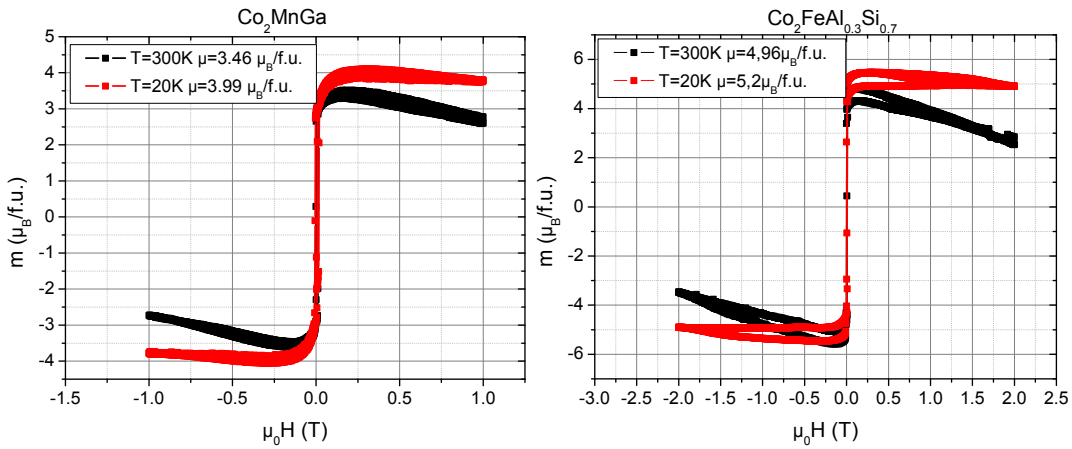


**Figure 4.13:** *Hysteresis curves at T=300 K (black) and T=20 K (red) of a $Co_2MnGa$ (left) and a $Co_2FeAl_{0.3}Si_{0.7}$ (right) films annealed at 550 °C.*

Information about the magnetic moments of the films is important for comparison with the theoretically predicted magnetic moments. Agreement with the predicted value would be an indication that the calculation is correct and the quality of the prepared films is appropriate to show half-metallicity.

The magnetization measurements of the different annealed temperature $Co_2FeAl_{0.3}Si_{0.7}$ films and of the $Co_2MnGa$ film annealed at 550 °C were made in a Vibrating Sample Magnetometer (VSM) with a magnetic field parallel to the surface plane.

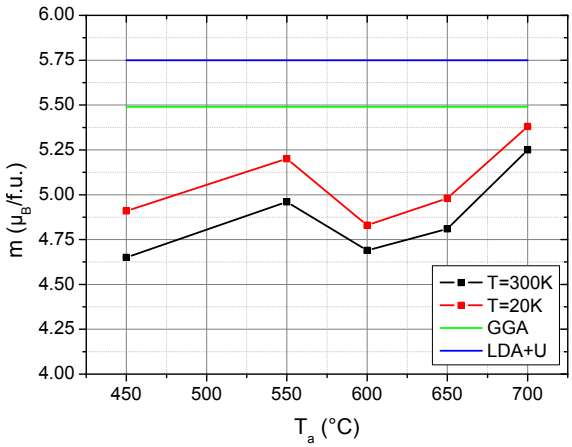


**Figure 4.14:** *Magnetic moments depending on the annealing temperature of $Co_2FeAl_{0.3}Si_{0.7}$ thin films. Magnetic moment values obtained at T=300 K (black) and T=20 K (red) are compared with the 5.45$\mu_B$/f.u. (GGA) and 5.75$\mu_B$/f.u. (LDA+U) theoretically predicted values (green and blue, respectively).*

A VSM is a sensitive device used to measure the magnetic behaviour of magnetic materials, such as the material magnetic moment dependence on time, applied magnetic field and temperature.

The hysteresis loops at 300 K and 20 K for a $Co_2MnGa$ film annealed at 550 °C are shown in figure 4.13, left. The saturation magnetization is 3.46 $\mu_B$/f.u. at 300 K and 3.99 $\mu_B$/f.u. at 20 K, which is quite close to the theoretically predicted value 4.05 $\mu_B$/f.u. [81]. By means of Slater Pauling rule a magnetic moment of 4.00 $\mu_B$/f.u. is obtained, which correspond to the same value obtained experimentally at 20 K. The same is shown in figure 4.13, right, for a $Co_2FeAl_{0.3}Si_{0.7}$ film annealed at 550 °C. A magnetic moment of 4.96 $\mu_B$/f.u. at 300 K and 5.2 $\mu_B$/f.u. at 20 K is measured for this film.

Additionally, the dependence of the magnetic moment on different annealed temperatures for $Co_2FeAl_{0.3}Si_{0.7}$ is shown in figure 4.14. Tiny variation around 5 $\mu_B$/f.u. is observed, which differs from the theoretically predicted value of 5.49 $\mu_B$/f.u. by the GGA approximation and 5.75 $\mu_B$/f.u. by the LDA+U approximation [85]. By means of Slater Pauling rule a magnetic moment of 5.70 $\mu_B$/f.u. is obtained. The sample most close to the predicted value is the one annealed at 700 °C. From the weak variation on the measured values, no dependency of the mag-

netic moment on the annealing temperature is concluded. There is a variation of the predicted magnetic moment depending on the method of calculation. However, the experimental value obtained is always smaller than predictions. The reason of experimental mismatching with theory is a non-perfect achieved $L2_1$ crystallographic structure in which theoretical calculations are based.

## 4.2 Surface properties

### 4.2.1 Reflection high-energy electron diffraction (RHEED)

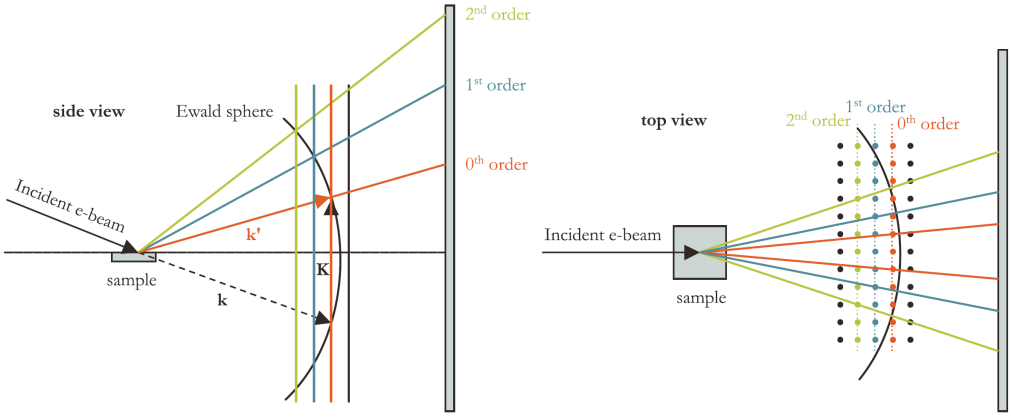


**Figure 4.15:** *Ewald sphere construction for a RHEED experiment.*

The crystalline order of the surface is studied by RHEED. Only information about the surface is obtained because the electrons can not penetrate deep in the volume of the film. Electrons with an energy of 18 kV hit the sample with an incident angle smaller than 5°, what implies a penetration depth of ≈20 Å. The distribution of the atoms at the surface (crystal structure and spacing between atoms) diffracts electrons, and those which interfere constructively following the Laue diffraction condition, reach the fluorescent screen and form the RHEED pattern. Thus, the diffraction pattern is surface feature dependent.

A sketch of the diffraction process in a RHEED experiment can be found in figure 4.15. A 2D system can be assumed due to the contribution of only the top atomic layers in the diffraction pattern. With this assumption, the reciprocal lattice can be seen as infinite rods perpendicular to the surface (see coloured lines

perpendicular to surface plane in figure 4.15). What is seen on the phosphorescent screen (bright dots around a circle in figures 4.16 and 4.17) is the diffraction pattern caused by the projection of the intersection of these rods with the "Ewald sphere" (black semicircle in figure 4.15).

The Ewald sphere determines which lattice planes (represented by the grid points on the reciprocal lattice) will result in a diffracted signal for a given wavelength of incident radiation.

The incident plane wave falling on the crystal has a wave vector k whose length is $2\pi/\lambda$. The diffracted plane wave has a wave vector k'. If no energy is gained or lost in the diffraction process (it is elastic) then k' has the same length as k. The amount the beam is diffracted by is defined by the scattering vector $\mathbf{K} = \mathbf{k}'\text{-}\mathbf{k}$ (Laue condition), see figure 4.15 as illustration. Since k and k' have the same length,the scattering vector must lie on the surface of a sphere of radius $2\pi/\lambda$ (Ewald sphere) [115, 127].

This diffraction pattern from a flat 2D surface on the screen of a RHEED system is an array of points situated on different circumferences corresponding to different diffraction orders.

The RHEED image of a $Co_2MnGa$ and a $Co_2FeAl_{0.3}Si_{0.7}$ film before and after annealing at 550 °C can be observed in figure 4.16, top and bottom, respectively. Additionally, a RHEED pattern evolution with annealing temperature of different $Co_2FeAl_{0.3}Si_{0.7}$ films is presented in different RHEED pictures in figure 4.17. Every picture is a different diffraction pattern corresponding to different samples. The first RHEED picture correspond to a sample which was not annealed, the second one is annealed at 250 °C and the others are annealed in increments of 100 °C until 650 °C, consecutively. The spots situated on different circles due to the different orders of diffraction can be clearly observed. For both $Co_2MnGa$ and $Co_2FeAl_{0.3}Si_{0.7}$ a clear improvement of the ordering is observed when comparing the image before and after the annealing process at 550 °C in figure 4.16. With this comparison the importance of annealing of the samples after deposition is illustrated. With the annealing process, the surface of the films become smoother and better ordered.

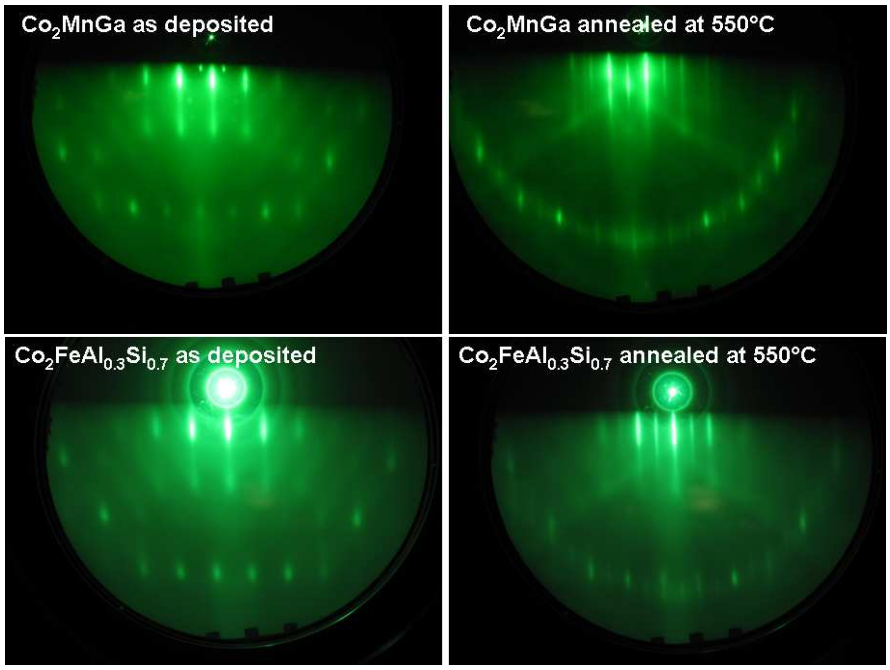


**Figure 4.16:** ***Top:*** *RHEED image of a $Co_2MnGa$ film before (left) and after (right) annealing at 550 °C.* ***Bottom:*** *RHEED image of a $Co_2FeAl_{0.3}Si_{0.7}$ film before (left) and after (right) annealing at 550 °C.*

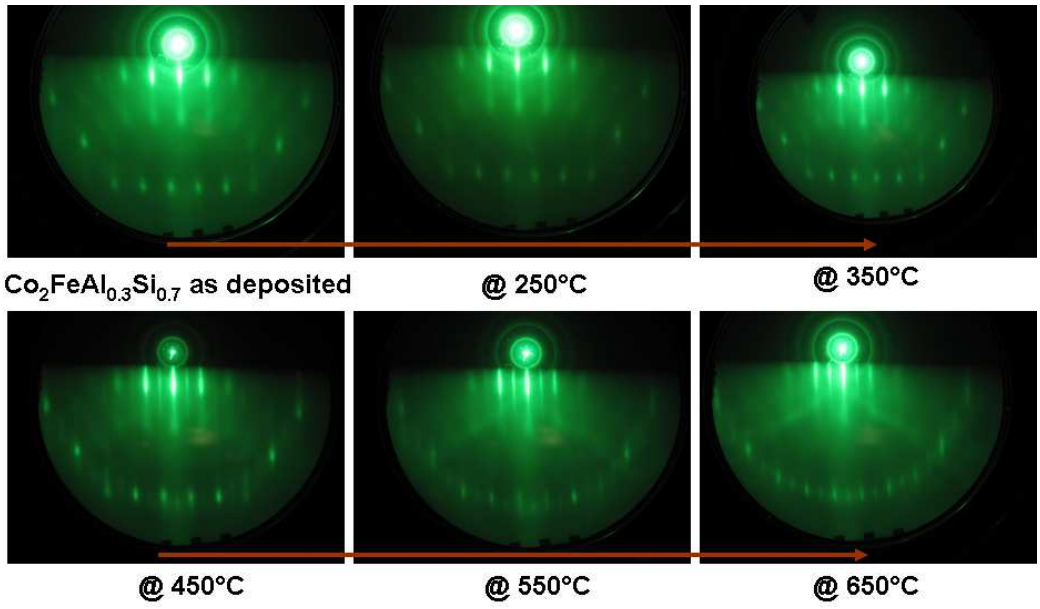


**Figure 4.17:** *RHEED images of a serie of $Co_2FeAl_{0.3}Si_{0.7}$ films annealed at different temperatures. From as deposited to 650 °C.*

For $Co_2FeAl_{0.3}Si_{0.7}$ the RHEED patterns reveal that surface ordering improves with temperature increase (figure 4.17). When comparing the RHEED image of the sample annealed at 350 °C with the one annealed at 450 °C a change is obvious. New spots with weaker intensity appear at 450 °C in between the brighter spots that are already present at 350 °C. This is an indication that a doubling of the unit cell in real space due to an improvement of the atomic positions has taken place. Therefore, at the surface, a crossover from B2 to $L2_1$ order is achieved already at 450 °C. In this case ordering in the surface seems to appear earlier than in the bulk, where $L2_1$ order appears above 550 °C.

The points of the diffraction pattern are not points with a punctual shape but with a linear shape. There are two possible reasons for this:

- A not completely monochromatic beam. The energy dispersion for the incident electrons causes that the Ewald sphere degenerates in a spherical shell and the intersection with the rods is not a punctual point.
- The mosaicity of the surface. In this case the rods are not unidimensional and their width increases with the distance to the surface, thus the intersection with the Ewald sphere has a line shape.

Therefore, it can be concluded that $Co_2MnGa$ and $Co_2FeAl_{0.3}Si_{0.7}$ films after annealing present a smooth and well ordered surface. Additionally, crystallographic order in the surface improves with annealing temperature, as well as it occurs in the bulk, for $Co_2FeAl_{0.3}Si_{0.7}$ films. However, the improvement of structural order from B2 to $L2_1$ appears at 450 °C in the surface while in the bulk such an order is observed at 550 °C.

### 4.2.2 X-ray Magnetic Circular Dichroism (XMCD)

In order to estimate if the magnetic properties in the bulk differ from the magnetic properties at the surface, an XMCD analysis is performed.

X-rays are a powerful source to study element specific electronic and magnetic properties of either mono- or multi-component materials. XMCD is a technique which is based on X-ray absorption spectroscopy and exploits the circular dichroism effect to measure the magnetic properties of 3d-transition metals. It allows a quantitative investigation of orbital and spin magnetic moments and it

can analyse bulk, interface and surface properties of thin films and multilayers.

The magnetic properties of 3d transition metal are mainly determined by their d valence electrons. Their properties are best probed in an X-ray absorption experiment by excitation of 2p core level electrons in empty 3d states above the Fermi energy (one electron model), as shown in figure 4.18 [128].

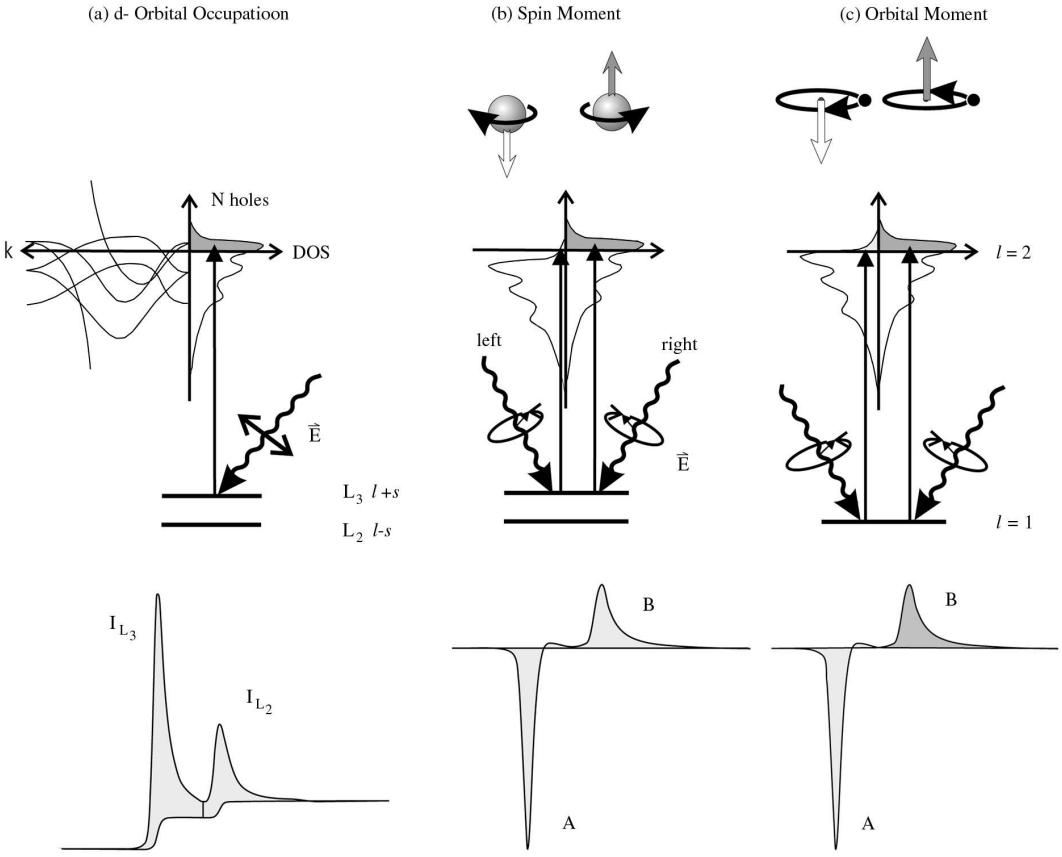


**Figure 4.18:** *(a) Electronic transitions in conventional L-edge X-ray absorption, (b) and (c) X-ray magnetic circular dichroism, illustrated in a one-electron model. The transitions occur from the spin-orbit split 2p core shell to empty conduction band states above the Fermi level. In conventional X-ray absorption the transition intensity measured as the white line intensity $I(L_3)+I(L_2)$ is proportional to the number of d holes, $n_h$=N. By use of circularly polarized X-rays the spin moment (b), and orbital moment (c), can be determined from the dichroic difference intensities A and B (see explanation in text) [128].*

The resulting L-edge X-ray absorption spectra contain contributions from $p \rightarrow d$ and $p \rightarrow s$ transitions, but the $p \rightarrow d$ channel dominates by a factor higher than 20 and $p \rightarrow s$ transitions are extracted from the spectra by a two step background subtraction as shown in figure 4.21 (green line). In the transition the contribution of two L-edges, $L_2$ ($2p_{1/2}$) and $L_3$ ($2p_{3/2}$), is considered due to the exchange split interaction which is much stronger in the p level as in the d level. The strong absorption peaks, often referred as "white lines", are due to an increase of the number of unoccupied d levels. Their intensities decrease with increasing occupation of the d-levels. The sum of the white lines, I($L_3$) and I($L_2$), is directly proportional to the number of d holes. It is the so called "charge sum rule":

$$I(L_3) + I(L_2) = Cn_h = C(10 - n) \tag{4.6}$$

where $n_h$ is the number of d holes, n is the number of occupied d states and $C = \frac{2}{15} A\Re^2$, where $A = 4\pi^2\hbar\omega\alpha_f$, $\Re$ is the radial transition matrix element, $\hbar\omega$ is the photon energy and $\alpha_f = \frac{e^2}{4\pi\varepsilon_0\hbar c} \approx \frac{1}{137}$ is Sommerfeld's fine structure constant [129].

XMCD spectra can be explained through the presence of two basic interactions: spin orbit coupling and exchange splitting.

The angular momentum of the photon is transferred to the photoelectron which can be transferred in part to the spin through the spin-orbit coupling. The direction of the angular momentum transferred to the electron depends on the radiation polarization, right or left circular polarized, respectively. In both cases photoelectrons with opposite spins are created. For each polarization direction, all the possible transition probabilities from $2p_{1/2}$ to 3d and from $2p_{3/2}$ to 3d, p level is splitted due to the spin-orbit coupling, are obtained by evaluating the transition matrix element in Fermi's Golden rule. The allowed transitions obey dipole selection rules. A scheme of the possible transitions for right polarized light is shown in figure 4.19 [130].

Summing over the final states with different spin orientation, for right circular polarized light, the excitations from the $L_2$ edge produces a net photoelectron spin polarization of -50 % and an orbital polarization of 75 %. The spin split

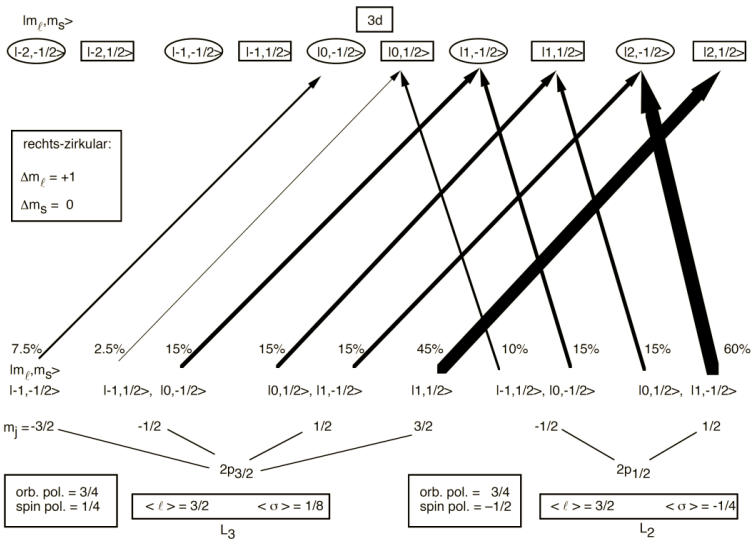


**Figure 4.19:** *Spin polarization of the photoelectrons originates from dipole transition rules for right circularly polarized light [130]. The width of the arrows is proportional to the transition probability.*

valence shell acts as a detector for the spin of the excited photoelectron. The quantization axis of the detector is given by the magnetization direction which needs to be aligned with the photon angular momentum direction in order to get the maximum dichroism effect.

The difference on the two absorption spectra (left or right circular polarized radiation) gives the MCD signal, where the two white line intensities A and B are related with the spin and orbital magnetic moments. Spin, orbital and charge sum rules, obtained from the transition rate calculations described above, allow a quantitative analysis of the spin and orbital magnetic moments as follows [129, 131, 132]:

$$\mu_s = -\frac{1}{C}(A - 2B)\mu_B \tag{4.7}$$

$$\mu_l = -\frac{2}{3C}(A + B)\mu_B \tag{4.8}$$

The experiment was performed at the UE56/1-SGM beamline at the German synchrotron light source BESSY II in Berlin in collaboration with other group. For a deeper understanding on the theoretical and experimental process the reader

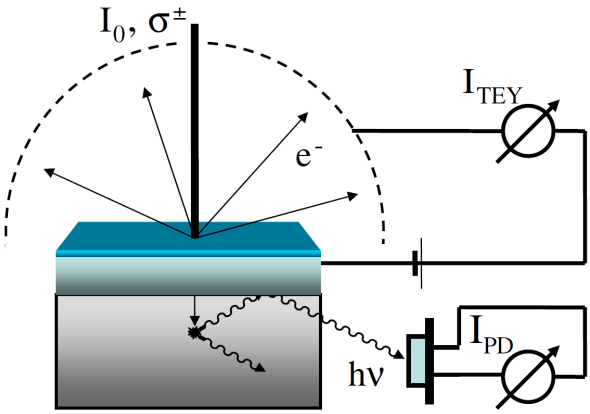


**Figure 4.20:** *Scheme of the experimental setup used for the X-ray absorption experiment in TM and TEY. Picture courtesy of M. Kallmayer [134].*

is referred to their work [133, 134, 135]. X-ray absorption spectra for a serie of $Co_2FeAl_{0.3}Si_{0.7}$ thin films annealed at different temperatures, between 450 °C and 700 °C, were measured.

An sketch of the experimental process can be observed in figure 4.20. X-ray light impinges on the thin film with right or left circular polarization in the presence of a magnetic field. In this experiment, the XMCD signal is achieved by fixing the X-ray polarization and changing the magnetic field direction.

Two different absorption spectra can be measured. In total electron yield mode (TEY) the X-ray absorption is determined via the photoemitted electrons originally stemming from the Auger relaxation of the 2p-core hole. It is a surface sensitive mode whose sensitivity is limited by the escape depth of the low-energy electrons (20-30 Å). It is measured via the sample current. The sample was shielded by a conducting tube on a positive bias voltage (100 V) in order to collect all electrons. In transmission mode the X-ray absorption is measured directly via X-ray luminescence in the substrate from the photon flux transmitted through the thin Heusler films. Bulk information is obtained via this mode which is only measurable on thin films. The luminescence light intensity was measured by a GaAs-photodiode. An external magnetic field of 1.6 T saturates the sample magnetization perpendicular to the film surface.

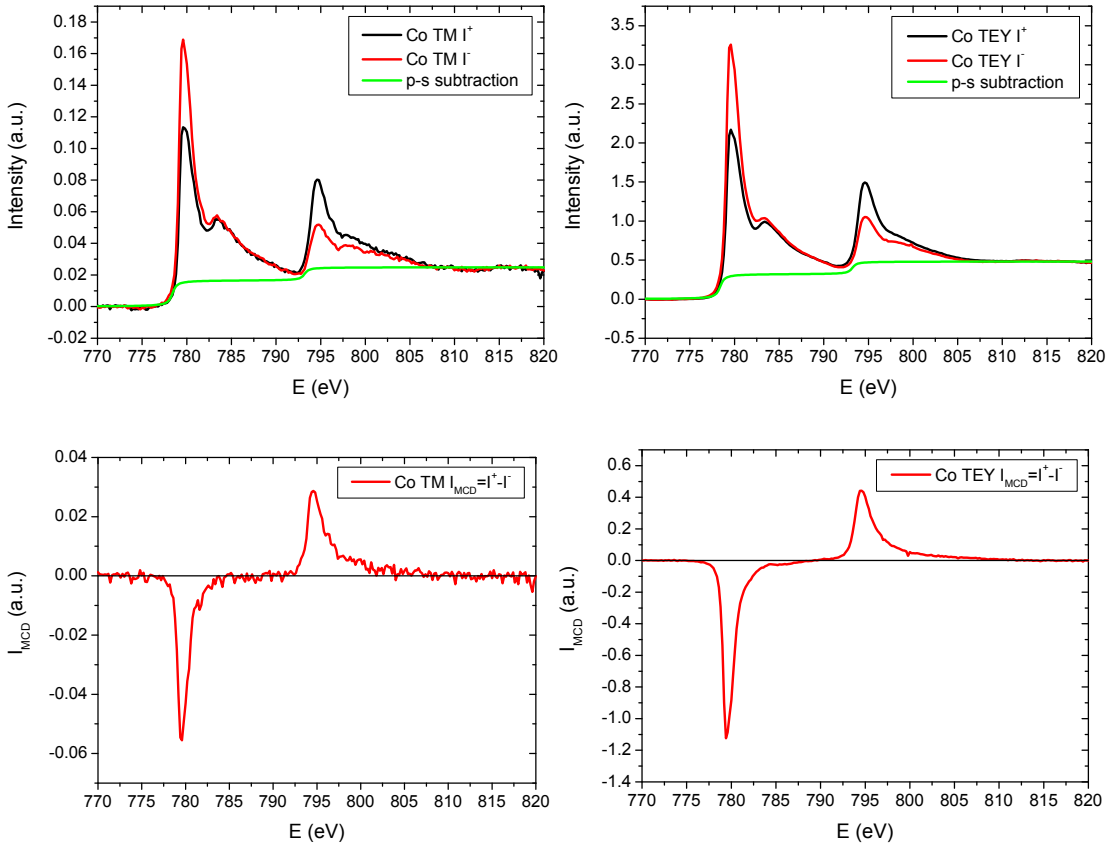


**Figure 4.21:** ***Top:*** *X-ray energy dependent (Co-edges) XMCD-TEY absorption intensity (right) and XMCD-TM absorption intensity (left) (T=300 K) for up $I^+$ (black line) and down $I^-$ (red line) magnetization of a 425 Å $Co_2FeAl_{0.3}Si_{0.7}$/20 Å Al sample annealed at 550 °C. The green line is the 2 step background substraction due to the p-s transition contribution.* ***Bottom:*** *X-ray energy dependent (Co edges) MCD-TEY signal (right) and MCD-TM signal (left) as a result of the difference between the two absorption spectra ($I^+$-$I^-$).*

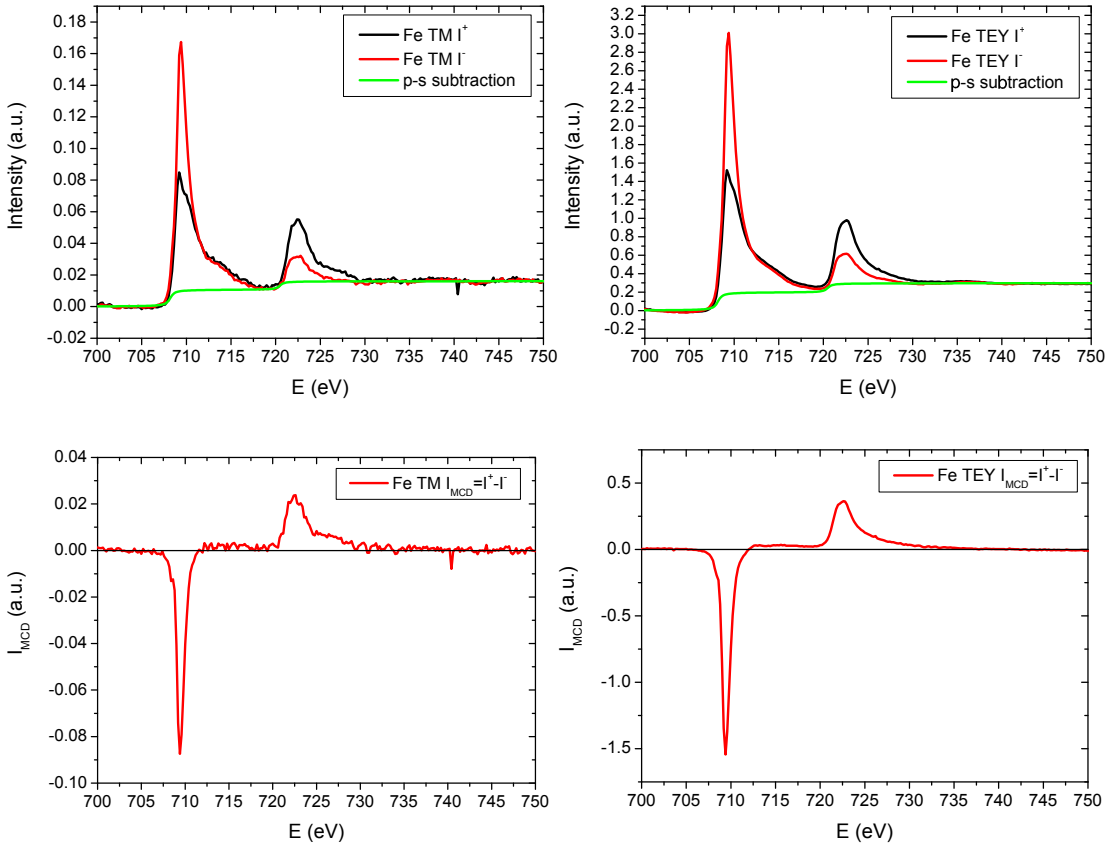


**Figure 4.22:** ***Top:*** *X-ray energy dependent (Fe-edges) XMCD-TEY absorption intensity (right) and XMCD-TM absorption intensity (left) (T=300 K) for up $I^+$ (black line) and down $I^-$ (red line) magnetization of a 425 Å $Co_2FeAl_{0.3}Si_{0.7}$/20 Å Al sample annealed at 550 °C. The green line is the 2 step background substraction due to the p-s transition contribution.* ***Bottom:*** *X-ray energy dependent (Fe edges) MCD-TEY signal (right) and MCD-TM signal (left) as a result of the difference between the two absorption spectra ($I^+$-$I^-$).*

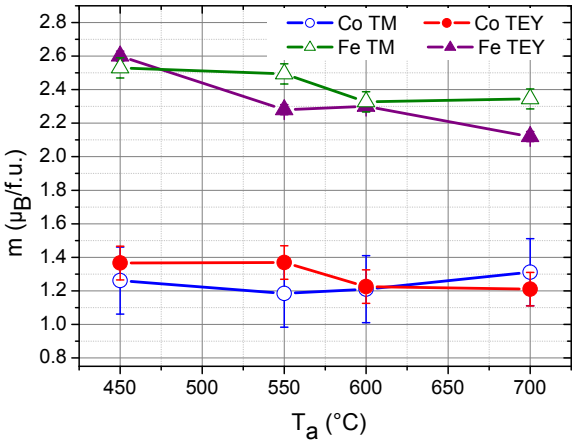


**Figure 4.23:** *Annealing temperature dependent element specific magnetic moment, Fe (triangle) and Co (circle), in TM (open symbols) and TEY (full symbols).*

The absorption spectra in TM (top-left) and TEY (top-right) mode for Co and Fe of a $Co_2FeAl_{0.3}Si_{0.7}$ thin film annealed at 550 °C is shown in figures 4.21 and 4.22, respectively, together with the MCD signal (graphs at the bottom, right (TEY) and left (TM) in figure 4.21 and 4.22) resulting from the difference between the two spectra measured at opposite magnetization directions. The absorption spectra are measured at different energy ranges depending on the p-d transition energy corresponding to the elements Co or Fe. When comparing the polarization up spectrum with the polarization down one an asymmetry is clearly visible. This asymmetry results in the MCD signal shown in the lower graphs of figures 4.21 and 4.22. From the two MCD peaks the magnetic moments are obtained through the sum rules as mentioned above. The resulting element specific magnetic moment values as a function of annealing temperature are plotted for both TEY and TM modes and shown in figure 4.23. As can be observed, no difference between bulk and surface magnetic moments is observed, only a small decrease of the Fe surface magnetic moment is present for the sample annealed at 700 °C. From these results it can be concluded that the magnetic properties at the surface do not differ from the bulk properties.

In figure 4.24, the total bulk (TM) and surface (TEY) magnetic moments obtained by XMCD are compared with the bulk values obtained by VSM. The good agreement of both methods (taking into account the XMCD error bars) make the results more reliable.

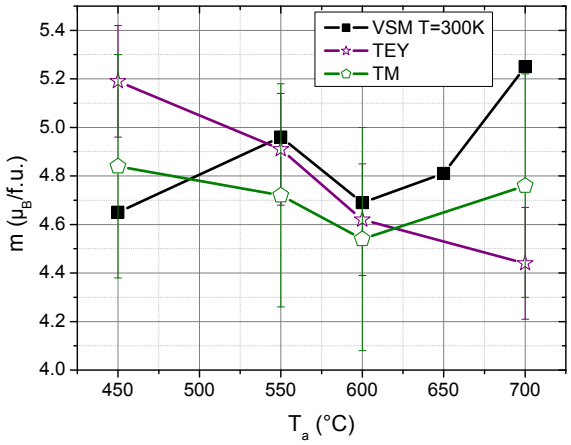


**Figure 4.24:** *Total bulk (open green polygon) and surface (open violet stars) magnetic moments compared with VSM results (full black squares) at 300 K as a function of annealing temperature.*

From all these different methods used for characterizing and understanding better the properties of the two Heusler materials $Co_2FeAl_{0.3}Si_{0.7}$ and $Co_2MnGa$ conclusions can be summarized as follows:

- Epitaxial growth and high bulk and surface quality of the thin films are achieved.
- Increasing annealing temperature improves the crystallographic order. A crossover from B2 to $L2_1$ is observed for $Co_2FeAl_{0.3}Si_{0.7}$.
- In bulk, the crossover from B2 order to $L2_1$ is observed at 550 °C (X-ray diffraction), while in the surface this change is already observed at 450 °C (RHEED).
- XMCD analysis revealed that magnetic properties in surface and bulk are the same for $Co_2FeAl_{0.3}Si_{0.7}$. No strong changes are observed.
- Experimental magnetic moments via VSM and XMCD differ from theory in $Co_2FeAl_{0.3}Si_{0.7}$ thin films while for $Co_2MnGa$ thin films the experimental result is in agreement with theoretical predictions. Moreover, the magnetic moment remains constant with improving crystallographic order (increase on annealing temperature).

- Surface and bulk properties of $Co_2FeAl_{0.3}Si_{0.7}$ thin films are demonstrated to be similar. Therefore, surface disorder problems would not be a reason, in this case, for a reduction of the spin polarization in the tunneling spectroscopy measurements.

# Chapter 5

# Ultraviolet Photoemission Spectroscopy

In this chapter the validity of band structure calculations of the Heusler compounds $Co_2FeAl_{0.3}Si_{0.7}$ and $Co_2MnGa$ is experimentally tested by Ultraviolet Photoemission Spectroscopy (UPS). This technique allows an experimental evaluation of $Co_2FeAl_{0.3}Si_{0.7}$ and $Co_2MnGa$ DOS close to the Fermi energy. Due to its surface sensitivity, UPS gives information about electronic states at the surface which can differ from bulk properties. First, a theoretical introduction to the concept of UPS and its connection with electronic properties is given, followed by the experimental description. Then, the experimental results are presented and discussed. Here a comparison of the experimental UPS spectra for $Co_2FeAl_{0.3}Si_{0.7}$ and $Co_2MnGa$ thin films are measured and compared with the total density of states of $Co_2FeAl_{0.25}Si_{0.75}$ and $Co_2MnGa$ as derived from the digitized graphs calculated by [85] and [81], respectively. Additionally, theory predicts that disorder results in a smearing out of the DOS [92, 67]. For the evaluation of this prediction, the influence of disorder on band structure features close to the Fermi energy is experimentally studied. Finally, conclusions are given.

## 5.1 Theoretical background

In Photoemission Spectroscopy (PES), monoenergetic photons from a source, like a He-lamp for Ultraviolet PES (UPS), impinge on a sample with an angle $\psi$ with respect to surface normal. All electrons with sufficient kinetic energy are emitted into the vacuum. Polar and azimutal angles $\theta$ and $\phi$ are chosen for the emitted

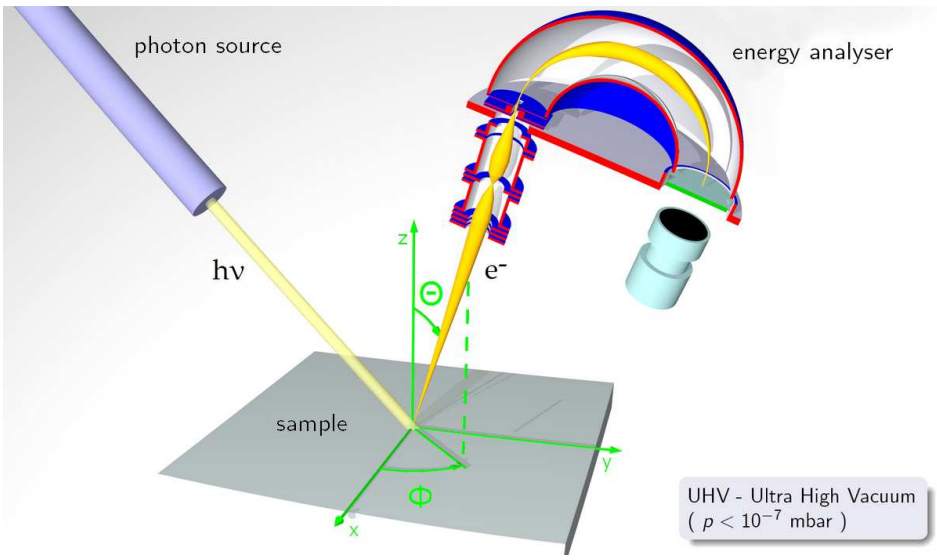


**Figure 5.1:** *General principle of ARPES [136].*

electrons and the electron energy distribution spectra is measured, see figure 5.1. With the resulting spectra, conclusions about the electronic band structure of the sample are obtained. In this theoretical introduction to UPS most of the information and concepts are taken from S. Hüfner's book [99] and for a deeper understanding the reader is referred to it.

The process is based on the photoelectric effect:

$$E_{ph} = h\nu = E_k + \phi \tag{5.1}$$

where $E_{ph}$ is the photon energy, $E_k$ the kinetic energy of the emitted electrons and $\phi$ is the energy needed to bring the electrons out of the solid into the vacuum.

In the ultraviolet regime the energy of the incoming photon is between 5 to 100 eV. In this regime the valence band structure of the solid can be investigated. The small kinetic energy of the excited electrons results in a low electron escape depth. Therefore with UPS only information about the electronic properties close to the surface is achieved.

### 5.1.1 Three step model

For the theoretical interpretation of PES experiments the "three step model" has proven to be useful. In this model the process of PES can be divided into three distinct and independent processes:

1. Photoionization: Absorption of the photon and excitation of the electron from its initial state to a final state.

2. Propagation of the excited electrons in the crystal to the surface. Here some inelastic scattering processes can take place (resulting in secondary electrons).

3. The electron escapes through the surface into the vacuum where it is detected.

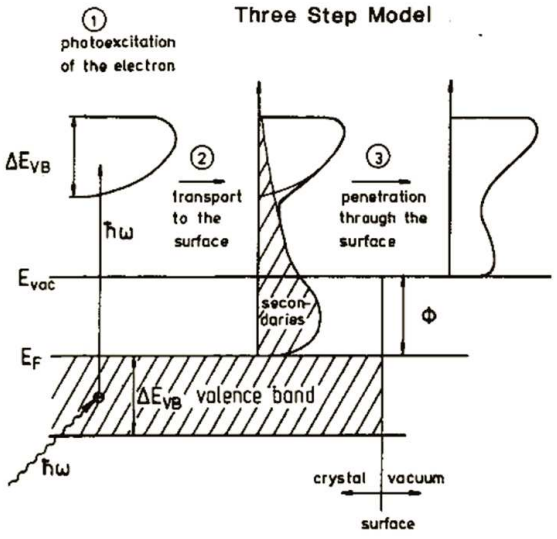


**Figure 5.2:** *Scheme of the three step model for PES [99].*

A detailed explanation of each step is given here and sketched in figure 5.2:

1. **Optical excitation of the electron in the solid.**
   The optical excitation is a direct transition in the reduced zone scheme. Here the energy and momentum of the photoexcited electron is conserved and the allowed transitions obey Fermi's Golden Rule

$$E_f(\mathbf{k}_f) = E_i(\mathbf{k}_i) + \hbar\omega \tag{5.2}$$

$$\begin{aligned} \mathbf{k}_f &= \mathbf{k}_i \quad \text{in the reduced scheme} \\ \mathbf{k}_f &= \mathbf{k}_i + \mathbf{G} \quad \text{in the extended scheme} \end{aligned} \tag{5.3}$$

The internal energy distribution of the photoexcited electrons $N_{int}(E, \hbar\omega)$, where E is the final kinetic energy and $\hbar\omega$ the photon energy, is given by

$$\begin{aligned} N_{int}(E, \hbar\omega) \propto \sum_{f,i} |\tilde{M}^1_{fi}|^2 \delta(\mathbf{k}_i + \mathbf{G} - \mathbf{k}_f) \\ \times \delta(E_f(\mathbf{k}_f) - E_i(\mathbf{k}_i) - \hbar\omega) \delta(E - E_f(\mathbf{k}_f) + \phi) \end{aligned} \tag{5.4}$$

where $E_f(\mathbf{k}_f)$ and $E_i(\mathbf{k}_i)$ correspond to the energies of the final and initial bands, respectively. Both, the final and initial band, are described as Bloch functions in this model. $\tilde{M}^1_{fi}$ is the transition matrix element of the interaction operator

$$H^{int} = \frac{e}{mc} \mathbf{A} \cdot \mathbf{P} \tag{5.5}$$

$\mathbf{A}$ is the vector potential of the exciting electromagnetic field and $\mathbf{P}$ is the momentum operator of the electron. The transition matrix element is determined by means of Fermi's Golden Rule. The first delta function refers to the momentum conservation, the second one imposes energy conservation and the third one is added to indicate that only photoemitted electrons with an energy above the vacuum level $\phi$ can be detected.

It can be assumed that the complete volume of the solid within the electromagnetic field penetration depth $\alpha^{-1}$ participates in the photoemission process.

2. **Transport of the electron to the surface**
   Once the electrons are excited, they propagate in the crystal to the surface. During the transport, scattering processes could take place and the number of photoexcited electrons reaching the surface with $E_f$ is reduced.

   The most dominant scattering mechanism is the electron-electron interaction, resulting in secondary electrons in the photoemitted spectrum. Assuming that the scattering frequency $1/\tau$ ($\tau \equiv lifetime$) is isotropic and

depends only on the energy E, the electron inelastic mean free path $\lambda(E,k)$ is given by:

$$\lambda(E,k) = \tau v_g = \frac{\tau}{\hbar}\frac{dE}{dk} \tag{5.6}$$

where $v_g$ is the group velocity in the final state. A classical transport description is defined by the d(E,k) coefficient [137]. It describes the fraction of the total number of photoelectrons created within one mean free path $\lambda$ from the surface

$$d(E,k) \simeq \frac{\alpha\lambda}{1+\alpha\lambda} \quad \text{dominant term} \tag{5.7}$$

$\alpha$ is the optical absorption coefficient of the light ($\alpha^{-1} \sim 100 - 1000$ Å in the energy range discussed here). To understand this function, two limits are analysed:

- $\alpha\lambda \ll 1 \Rightarrow d(E,k) \to \alpha\lambda$, in the case of an electron mean free path much smaller than the light penetration depth, the electrons generated deeper in the material than the mean free path suffer inelastic scattering.

- $\alpha\lambda \gg 1 \Rightarrow d(E,k) \to 1$, in the case of an electron mean free path much bigger than the light penetration depth, all the electrons arrive to the surface without scattering.

The electron mean free path depends on the kinetic energy. Thus in the particular case of UPS, for an energy of 21.2 eV, for example, the mean free path is about 7 Å [138]. This energy corresponds to the excitation of an electron with the He I-line directly at the Fermi-edge. Consequently, an electron with this energy can propagate around 7 Å without experimenting inelastic scattering. Therefore, UPS is known as a surface sensitive method, because only information at a small depth (few Å) can be achieved.

The surface sensitivity also depends on the emission angle of the emitted electrons with respect to surface normal.

$$l(E_{kin},\theta) = \lambda(E_{kin})cos\theta \tag{5.8}$$

The maximum information depth is achieved by normal detection, $\theta = 0$. At higher angles the information depth decreases.

3. **Escape of the electron into vacuum**
In this last step the photoexcited electrons are transmitted into the vacuum. The escaping electrons in their final excited state are those for which the component of the kinetic energy normal to the surface is sufficient to overcome the surface potential barrier; the other electrons are totally reflected back into the bulk.

The excited electrons in the solid can be described as free electrons that move in a potential well of depth $E_v - E_0$. For escape into the vacuum, the electrons must pass over this potential well. The component of the kinetic energy perpendicular to surface in the final state has to be larger than $E_v - E_0$, i. e.

$$\frac{\hbar^2}{2m}\mathbf{k}_{f\perp}^2 \geqslant E_v - E_0 \Rightarrow \mathbf{k}_{f\perp,min} = \sqrt{\frac{2m(E_v - E_0)}{\hbar^2}} \tag{5.9}$$

where $E_0$ is the energy of the valence band bottom, $E_v$ is the vacuum energy and $\mathbf{k}_{f\perp}$ is the component of the final wave vector of the excited electrons normal to the surface. Here the parallel component of the wave vector is conserved

$$\mathbf{p}_{||}/\hbar = \mathbf{k}_{f||} = \mathbf{k}_{i||} + \mathbf{G}_{||}^s \tag{5.10}$$

where p is the momentum of the photoelectron in vacuum, $\mathbf{k}_{f||}$ is the parallel component of the wave vector $\mathbf{k}_f$ of the photoexcited electron and $\mathbf{G}^s$ is the surface reciprocal lattice vector.

The energy of an electron in vacuum is defined as

$$E_{kin} = E_f - \phi = E_i + \hbar\omega - \phi \tag{5.11}$$

Within the free electron model for the excited electrons, $\mathbf{p}_{||}/\hbar$ simply reflects Snell's law

$$\mathbf{k}_{f||} = sin\theta \left(\frac{2m}{\hbar^2}E_{kin}\right)^{\frac{1}{2}} = sin\theta' \left[\frac{2m}{\hbar^2}(E_f - E_0)\right]^{\frac{1}{2}} \tag{5.12}$$

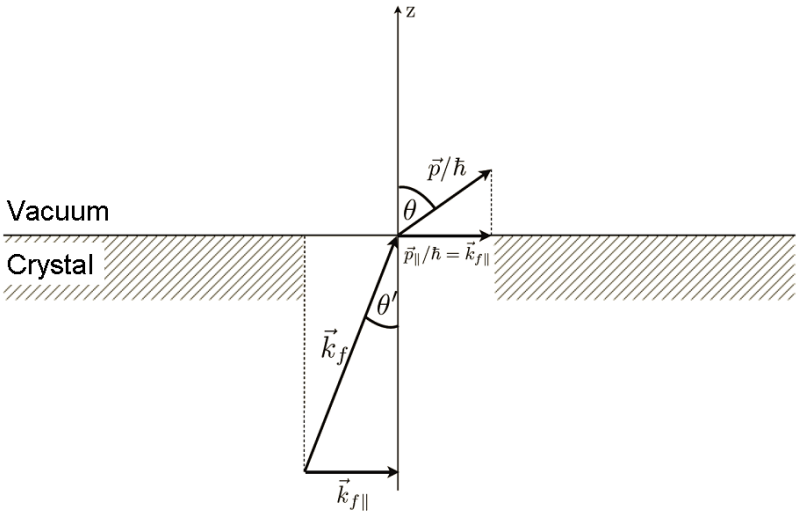


**Figure 5.3:** *Momentum relations at the crystal-vacuum interface [99].*

where $\theta$ is the angle outside and $\theta'$ is the angle inside the sample with respect to the surface normal. The momentum relations at the solid-vacuum interface is shown in figure 5.3. From this relation it can be concluded that

$$\forall E_f(\theta \leqslant \frac{\pi}{2}), \exists \theta'_{max}/sin\theta'_{max} = \sqrt{\frac{E_{kin}}{E_f - E_0}} \tag{5.13}$$

It exists a maximum angle $\theta'$ in the solid, below which the excited electrons with their final energy can cross the surface. The angular region $\theta' \leqslant \theta'_{max}$ is called the escape cone.

The kinetic energy outside the crystal is determined by:

$$E_{kin} = \frac{\hbar^2}{2m}[\mathbf{k}^2_{f_{\|}} + (p_{\perp}/\hbar)^2] = E_f(\mathbf{k}) - E_v \tag{5.14}$$

where $p_{\perp}/\hbar$ is the perpendicular component of the electron wave vector in the vacuum.

Experimentally, the emission angle $\theta$ of the excited electrons in the vacuum is limited by the angular resolution of the energy analyser which is $\pm 10°$ in our experiment and it is positioned at $0°$. Additionally, the light (21.2 eV and 40.8 eV photon energy) from the He-lamp used as photon source

is not polarized. Thus, in normal emission from (001) oriented thin films, assuming an $L2_1$ structure, not only the electronic states with momentum **k** parallel to Γ-X direction (001) contribute to the energy spectrum but also those which momentum **k** is between 0° and 10°. The maximum value of the parallel component of the final electron momentum **k** in the vacuum is, by means of equation 5.12, $k_{f_{\parallel}}$=3.56×10$^9$ m$^{-1}$.

An elemental cell in a Heusler compound with $L2_1$ order is a fcc lattice, which correspond to a bcc lattice in the reciprocal space. Therefore, the primitive lattice vector in the direction parallel to $k_{f_{\parallel}}$ correspond to $\mathbf{G}_{\parallel} = \frac{2\pi}{a_{L2_1}}(010)$, i.e. $G_{\parallel} = 10.1 \times 10^9$ m$^{-1}$ ($a_{L2_1} = 5.7 \times 10^{-10}$ m). This indicates that, the obtained information is not average over the complete Brillouin zone because the in plane wave vector amounts to $k_{f_{\parallel}}$=3.56×10$^9$ m$^{-1}$, which corresponds to 1/3 of the Brillouin zone.

None of these equations contains the observable $\mathbf{k}_{f\perp}$ inside the crystal. Thus experimental problems to determine the full wave vector $\mathbf{k}_f$ of the crystal state arise. An approximate solution is the so-called **"free-electron final state model"** which assumes a free electron final state:

$$E_f = (\hbar^2/2m^*)(\mathbf{k} + \mathbf{G})^2 - |E_0| \tag{5.15}$$

where $m^*$ is the effective mass, and the energies are measured with respect to the Fermi energy. The inner potential $V_0 = E_0 + \phi$ and $m^*$ are the parameters to be determined. The free electron mass is $m^* = m$ and $V_0$ can be determined by using the theoretical muffin-tin zero potential.

For simplification, let us assume a normal emission experiment. The peaks observed in the UPS spectrum are related to the energy of the initial states with respect to the Fermi energy and to the perpendicular wave vector in a way that the free electron parabola is attached to the bottom of the conduction band at $E_0$ and the measured spectrum with its low-kinetic energy cutoff at $E_v$. The intersection of the measured peak energies with the free electron parabola starting at $E_0$ gives the wave vector $k_\perp$ of these states and a shift parallel to the energy axis to lower energies by $\hbar\omega$ yields the

initial state band structure energies $E_i(k_\perp)$.

This model can be only an approximation since the optical excitation takes place in the presence of a crystal potential. This approximation gets better with higher excitation energies because the crystal potential gets weaker with increasing the kinetic energy of the electron. However, at higher energies a quick decrease of the electron mean free path induces an increase on the wave-vector broadening and therefore a smearing out of the direct transition features.

In a solid the wave function $\psi_f(\mathbf{k})$ of a state at $E_f(\mathbf{k})$ is a Bloch wave containing plane-wave contributions with a number of reciprocal lattice vectors $\mathbf{G}$:

$$\psi_f(\mathbf{k}) = \sum_{\mathbf{G}} u_f(\mathbf{k}, \mathbf{G}) e^{i(\mathbf{k}+\mathbf{G})\cdot\mathbf{r}} \tag{5.16}$$

Each component has the possibility of matching to an escaping wave outside the crystal, which means that the photoelectron can emerge from the crystal in a number of possible directions determined by eq. 5.12 and 5.14.

The final expression for the angle-resolved photoelectron energy spectrum $N(E, \mathbf{k}_{f_\parallel}, \hbar\omega)$ at photon energy $\hbar\omega$ is

$$\begin{aligned} N(E, \mathbf{k}_{f_\parallel}, \hbar\omega) \propto \sum_{f,i} & |\tilde{M}^1_{fi}(\mathbf{k}_i, \mathbf{k}_f)|^2 d(E_f, \mathbf{k}_f) |T(E_f, k_{f_\parallel})|^2 \\ & \times \delta(E_f(\mathbf{k}_f) - E_i(\mathbf{k}_i) - \hbar\omega) \delta(E - [E_f(\mathbf{k}_f) - \phi]) \\ & \times \delta(\mathbf{k}_i + \mathbf{G} - \mathbf{k}_f) \delta(k_{f_\parallel} - p_\parallel(\theta, \varphi)/\hbar) \end{aligned} \tag{5.17}$$

$|\tilde{M}^1_{fi}(\mathbf{k}_i, \mathbf{k}_f)|^2$ represents the optical transition probability, the function $d(E_f, \mathbf{k}_f)$ takes the inelastic scattering processes into account, $|T(E_f, k_{f_\parallel})|^2$ is the transmission probability and the delta functions represent the different conservation laws.

Although the three step model violates the uncertainty principle, due to the assumption that the optical excitation takes place inside the solid before propagating and transmitting into the vacuum, and that the electrons lose energy due to inelastic scattering processes after optical excitation, many experimental

analysis have demonstrated this model to be an accurate approximation. This model shows the basis of photoemission spectroscopy. However, for a refined understanding and to be able to determine band structures of a solid from the PE experimental data, a deeper knowledge about the theoretical aspects of this technique is required.

### 5.1.2 One step model

The most significant physical effects neglected in the three step model are the interference between bulk and surface emission, the interference between loss and no-loss transport from the photoexcitation place to the surface, and the description of the escape of the electron through the surface by a simple transmission factor. A shortcoming of this model is the assumption that the final state can only be described by bulk Bloch states.

For taking properly the mentioned effects into account the inverse LEED theory of PES was developed and it is well explained by Mahan [139]. Within this formalism the equation for the photocurrent results in

$$N(E,\hbar\omega,\hat{\mathbf{R}}) \propto \upsilon \cdot \sum_{occupied,i} (|\langle\psi^L(\mathbf{r},E,\mathbf{k}_f)|H^{int}|\psi_i(\mathbf{r},\mathbf{k})\rangle|^2)|M_{fi}|^2 \times\delta(E_f - E_i - \hbar\omega) \qquad (5.18)$$

where $E = E_f - \phi$ is the kinetic energy of the photoelectron, $\hat{\mathbf{R}}$ the unit vector along the photoelectron beam, $\mathbf{k}_f$ is the photoelectron wave vector in the vacuum and $\mathbf{k}$ is the photoelectron wave vector in the solid. $\psi^L(\mathbf{r},E,\mathbf{k}_f)$ and $\psi_i(\mathbf{r},\mathbf{k})$ are the final states on vacuum and the initial states in the solid, respectively.

The final states in the crystal are written as sums of propagating and evanescent waves expanded in terms of two-dimensional Bloch functions and the initial state can be described in terms of two-dimensional Bloch functions as shown and explained schematically in figure 5.4.

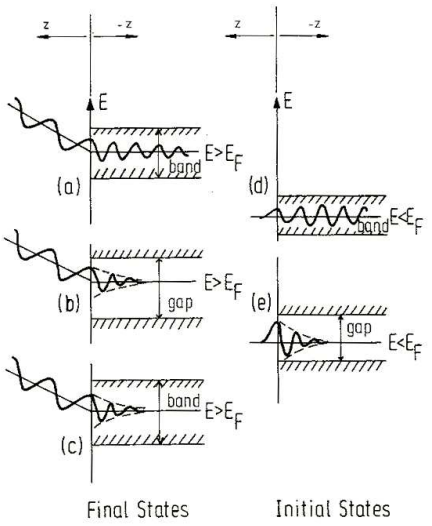


**Figure 5.4:** *Wave functions involved in PES in the inverse LEED formalism.* ***Left:*** *Final states: (a) bulk Bloch wave, weakly damped; (b) strongly damped gap state (surface state); (c) strongly damped Bloch wave (short mean free path).* ***Right:*** *Initial states: (d) bulk Bloch wave; (e) surface state in the gap*

## 5.2 Experiment

ARPES is an experimental technique which provides information about the electronic DOS close to the Fermi energy. Due to its surface sensitivity, information about surface band structure, which can differ from the bulk is obtained. For reliable results, extremely clean and well ordered surfaces are required.

There are different ways to deal with the surface quality of the sample and carried-out ARPES experiments. On one hand, there are experiments where bulk samples are fractured or polished inside the spectroscopy chamber [140, 141, 142], or after the preparation of bulk or thin film samples, they are transferred ex-situ into another chamber for ARPES analysis [143, 25]. On the other hand, for complex intermetallic alloys like Heusler, such methods are not suitable due to distortions of the surface order and stoichiometry. A solution to this inconvenience is to use HAXPES for the detection of photoemitted electrons from thin films capped by thin MgO layers [144, 145]. This results in an increase of the PES information depth up to 20 Å [138]. Another possibility is to transfer the uncapped sample in a vacuum suitcase to a synchrotron facility for spin polariza-

tion PES measurements [146].

The experiment performed here consists of measuring ARUPS of uncapped Heusler thin films in-situ in an UHV analysis chamber directly after preparation. The analysis chamber is part of a cluster system where all chambers are connected and samples can be transported from one chamber to the other by a transfer arm (see figure 3.1). This allows to measure undistorted atomically clean surfaces and because the preparation procedure is the same as for Magnetic Tunnelling Junction devices, a direct comparison is possible. Previous work has already demonstrated the validity of this method concerning surface purity [147].

The preparation of the samples is described in chapter 3. After the annealing process the sample is transferred to the analysis chamber for ARUPS. The analyser used in this experiment is a Leybold EA-10/100 hemispherical electron energy analyser. An entire setup description is found in [148].

The energy distribution spectra are measured in the normal direction of the (001)-oriented thin films. The photon source is a Helium gas discharge lamp which produces two unpolarized photon energies of 21.2 eV (HeI) and 40.8 eV (HeII). The typical pressure in the chamber with the He-lamp on is of the order of $6 \times 10^{-8}$ mbar. The spot diameter on the sample is around 3 mm. The photon angle of incidence on the sample surface is $\psi \simeq 50°$. The sample can be tilted with a maximum angle of 20° off-normal and consequently the photon angle of incidence can change until a maximum value of 70°. The angular resolution of the energy analyser is 10°. The energy resolution is around 200 meV. The EDC's for different samples or the same samples transferred temporarily into other chamber can not be compared quantitatively. A qualitative comparison can be made by scaling the curves.

The purpose of this experiment consists, first, in testing the validity of Band Structure Calculations (BSC) by the investigation of DOS related features, and second, in testing experimentally how the influence of disorder effects DOS features close to the Fermi energy as also predicted by theory [92, 67].

For the study of the influence of disorder on the DOS features, thin films of the Heusler compound $Co_2FeAl_{0.3}Si_{0.7}$ annealed at different temperatures were

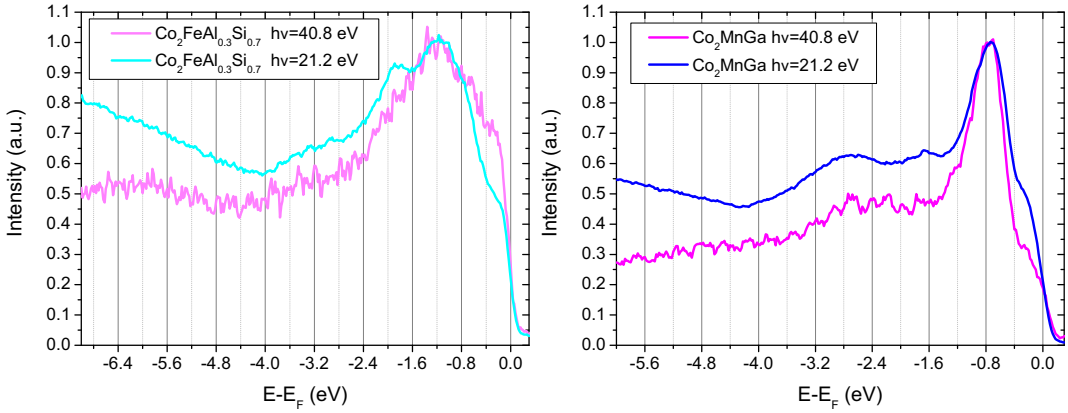


**Figure 5.5:** ***Left:*** *Comparison of the UPS spectra of a $Co_2FeAl_{0.3}Si_{0.7}$ thin film obtained with h$\nu$=40.8 eV (light pink) and h$\nu$=21.2 eV (light blue) photon energy.* ***Right:*** *Comparison of the UPS spectra of a $Co_2MnGa$ thin film obtained with h$\nu$=40.8 eV (pink) and h$\nu$=21.2 eV (blue) photon energy.*

analysed by UPS with 21.2 eV and 40.8 eV photon energies. Additionally, UPS on thin films of the Heusler compound $Co_2MnGa$ annealed at 550 °C was also performed. Results and conclusions are shown in the next sections. Moreover first measurements of spin-polarized UPS on $Co_2MnGa$ was carried out within a collaboration with other group [149]. The results are discussed at the end of this chapter and are compared later with spin polarization values obtained by measuring the TMR of MTJ's.

## 5.3 Results

First, ARUPS measurements for $Co_2FeAl_{0.3}Si_{0.7}$ and $Co_2MnGa$ thin films annealed at 550 °C were carried out with 21.2 eV and 40.8 eV photon energies. The results for the two different Heusler compounds are shown in figure 5.5. On the left graph a comparison of the ARUPS spectra of $Co_2FeAl_{0.3}Si_{0.7}$ obtained with h$\nu$=40.8 eV (light pink) and h$\nu$=21.2 eV (light blue) photon energy is shown. On the right, the same comparison for $Co_2MnGa$ is made. In both cases, the two spectra show obvious differences. If only DOS would contribute to the UPS measurement both spectra should look identical. However, there are other aspects which contribute to the UPS signal:

- Direct optical transitions which are photon energy dependent. Hence, dif-

ferent transitions associated to different photon energies would contribute differently in the UPS signal. In the three step model, ARUPS are dominated by direct optical transitions which are photon energy dependent. The intensity in a direct transition is related to a joint density of an initial and a final state [99]. In metals like Ag with s-p electrons and well defined bands these direct transitions dominate the UPS spectrum. However in strongly correlated systems with d-electrons, like it is the case for $Co_2FeAl_{0.3}Si_{0.7}$ and $Co_2MnGa$ a broadening of the bands makes many direct transitions possible and therefore a smearing of the emission peaks due to direct transitions characterize the photoemission spectrum. Nevertheless, strong emission peaks should always be related to an energy range with a high density of initial states and consequently DOS contributions dominate the UPS intensity features. This has already been experimentally demonstrated [147, 148, 149].

- The He II-line (h$\nu$=40.8 eV) is 100 times weaker than the He I-line (h$\nu$=21.2 eV). Therefore, the outcoming intensity has to be increased by a multiplication factor, resulting in a much more noisy signal of the UPS spectra obtained with h$\nu$=40.8 eV, as can be observed in figure 5.5 for both Heusler spectra.

- Different information depth. When the material is irradiated with a photon energy of h$\nu$=21.2 eV, an information depth of around $\sim$7 Å is achieved. However, with a photon energy of h$\nu$=40.8 eV, an information depth of around $\sim$3.5 Å is achieved. This means, that the h$\nu$=40.8 eV spectra is even more surface sensitive than the h$\nu$=21.2 eV spectra. Taking into account that the lattice constants for $Co_2FeAl_{0.3}Si_{0.7}$ and $Co_2MnGa$ are $\sim$5.7 Å, information of about less than 2 unit cells is obtained with h$\nu$=21.2 eV, while information of about less than 1 unit cell is obtained with h$\nu$=40.8 eV. This explains the different features observed in the $Co_2FeAl_{0.3}Si_{0.7}$ UPS spectra (see left graph of figure 5.5), where two intensity features are observed for the spectrum obtained with h$\nu$=21.2 eV, whereas only one is observed for the spectrum obtained with h$\nu$=40.8 eV.

- The photoionization cross section is, in general, energy dependent. d-states are weaker dependent than s-p states. Thus, the relative emission intensity of the oxygen state (2p-like) referred to the Heusler states (3d-like) is reduced for h$\nu$=40.8 eV compared with h$\nu$=21.2 eV [150]. Although here only a weak oxidation peak is observed for $Co_2FeAl_{0.3}Si_{0.7}$ because the analysis was done for *"clean"* surfaces, previous work on the influence of oxidation in $Co_2Cr_{0.6}Fe_{0.4}Al$ and $Co_2FeAl$ heusler compounds has demonstrated the oxidation peak to be at E-$E_F$ $\simeq$-6 eV and reduced for h$\nu$=40.8 eV compared with h$\nu$=21.2 eV [147].

For both Heusler compounds and both photon energies, the most obvious common features in ARUPS spectra are observed near the Fermi edge (see figure 5.5). In the rising edge of the pronounced emission peaks there is a shoulder like feature in the four spectra. Its origin would be discussed later.

Differences between the two compounds are also obvious. They can be related to energy ranges with a high density of initial states and are compared with the theoretically predicted total bulk density of states.

Since ARUPS is a non-spin-dependent measurement, it needs to be compared with the theoretical total DOS which is obtained from the digitized spin-resolved graphs for $Co_2FeAl_{0.3}Si_{0.7}$ [85] and $Co_2MnGa$ [81]. The total bulk density of states of $Co_2FeAl_{0.3}Si_{0.7}$ and $Co_2MnGa$ were calculated by Felser et al. [85] and Galanakis et al. [81]. They are shown in the top graphs of figure 5.6, left and right, respectively. For $Co_2FeAl_{0.25}Si_{0.75}$ (top left) the first DOS feature appears at E-$E_F$ $\simeq$-1.1 eV (labelled B). From 0 eV to -1.1 eV no DOS increase is observed. Between -1 eV and -2 eV two more DOS features are present at -1.4 eV and -1.75 eV (labelled C).

For $Co_2MnGa$ (top right) the first DOS feature is closer to the Fermi energy, at E-$E_F$ $\simeq$-0.75 eV (labelled E). From 0 eV to -0.75 eV an increase of DOS is observed. Between -0.4 eV and -2 eV two more DOS features are present at -1 eV (labelled F) and -1.6 eV (labelled G).

For comparison, in the same figure 5.6 the ARUPS spectra obtained with a photon energy of h$\nu$=40.8 eV (middle) and h$\nu$=21.2 eV (bottom) for thin

films of the Heusler compounds $Co_2FeAl_{0.3}Si_{0.7}$ (left) and $Co_2MnGa$ (right) after annealing at 550°C are shown.

For $Co_2FeAl_{0.3}Si_{0.7}$, the spectrum obtained with h$\nu$=40.8 eV (left middle) shows a very broad peak which starts to increase directly at the Fermi energy, has a change of slope at E-$E_F$ $\simeq$-0.2 eV (labelled A) and achieves its maximum value at E-$E_F$ $\simeq$-1.1 eV (labelled B). The spectrum obtained with h$\nu$=21.2 eV (left bottom) shows the same A and B features observed with h$\nu$=40.8 eV but more pronounced. Additionally, another feature at E-$E_F$ $\simeq$-1.75 eV (labelled C) is visible. When comparing both ARUPS expectra with the theoretical total DOS (top left) differences are obvious. First, the main ARUPS features are much broader than theoretically predicted. There are different possible reasons why the UPS intensity features are broader than in theory.

On one hand, well defined peaks are difficult to observed experimentally due to the ARUPS resolution which is 200 meV, comparable to the broadening of the theoretical bulk DOS features (between 200 and 500 meV).

On the other hand, total bulk DOS calculations are based on LDA+U approximations which usually show sharp and well defined DOS features. However, LSDA+DMFT has demonstrated that for systems which contain d-electrons close to the Fermi energy, like in Heusler alloys, a smearing of the DOS is predicted because of finite lifetime effects [60]. Therefore, it is likely that the broad features observed by UPS experiments correspond to a smearing of the DOS features as LSDA+DMFT predicts.

Moreover, an intensity feature (labelled A) together with an intensity increase close to the Fermi energy present in ARUPS spectra do not correspond to the calculated total bulk DOS. Apart from the smearing of the DOS features due to correlations (d-electrons) another possibility to explain this behaviour is the presence of surface states, which are not predicted by theoretical calculations. The contribution of surface states can induce changes of the DOS and the half metallic properties could be even lost [197]. Additionally, it has been predicted that some degree of disorder can contribute to changed DOS features [92, 67]. However, and as will be shown later, disorder does not contribute to such stronger changes like observed here, but only to some broadening of the ARUPS features.

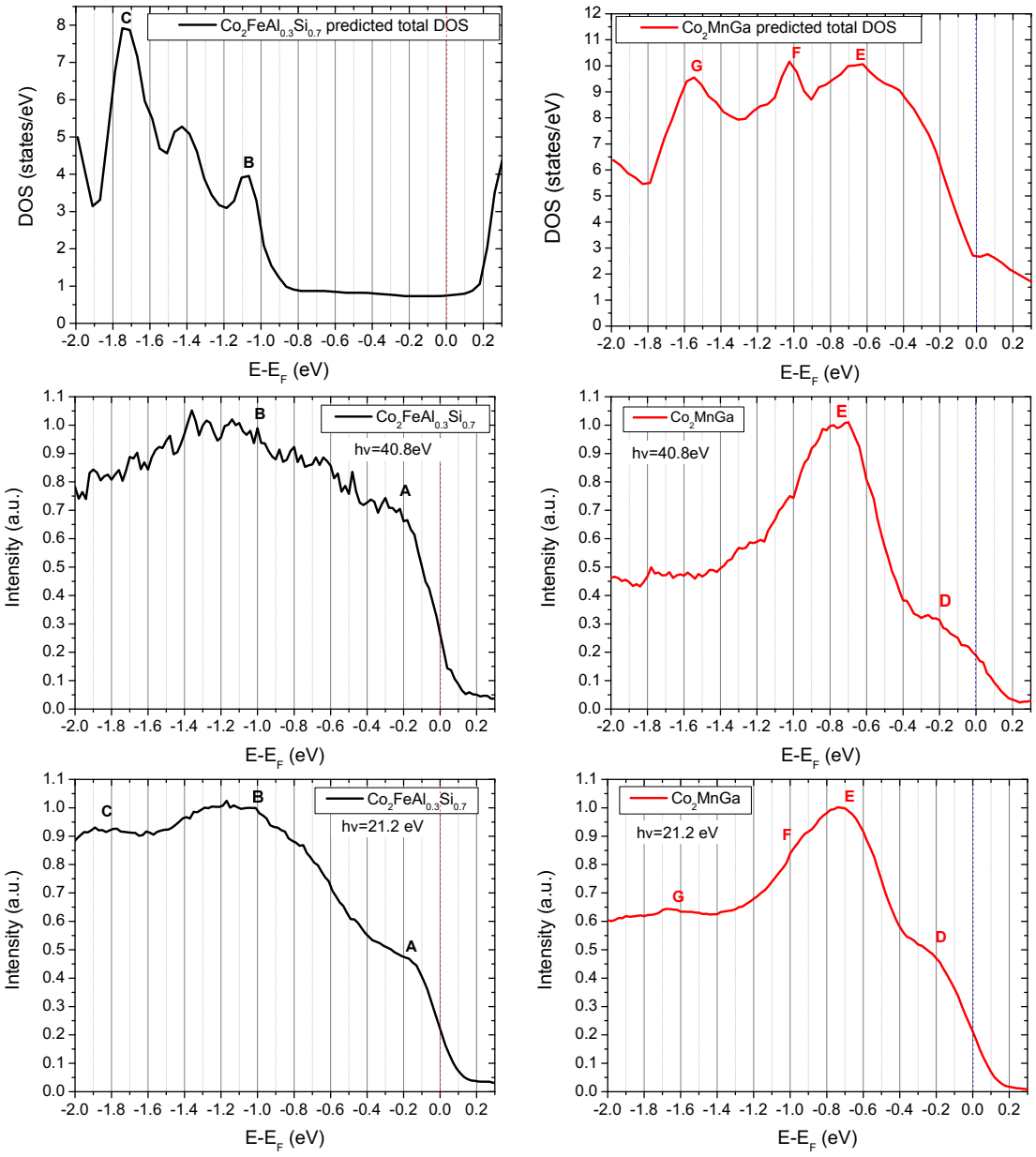


**Figure 5.6:** *Comparison of theoretical predicted total DOS with experimental UPS intensity obtained for thin films of the two Heusler compounds:* $Co_2FeAl_{0.3}Si_{0.7}$ *(left) and* $Co_2MnGa$ *(right).* ***Top:*** *Total density of states of* $Co_2FeAl_{0.25}Si_{0.75}$ *(left) and* $Co_2MnGa$ *(right) as derived from the digitized graphs calculated by [85] and [81], respectively.* ***Middle:*** *UPS spectra of a* $Co_2FeAl_{0.3}Si_{0.7}$ *(left) and a* $Co_2MnGa$ *(right) thin film obtained with* $h\nu$*=40.8 eV photon energy.* ***Bottom****: UPS spectra of a* $Co_2FeAl_{0.3}Si_{0.7}$ *(left) and a* $Co_2MnGa$ *(right) thin film obtained with* $h\nu$*=21.2 eV photon energy.*

Therefore, the most probable reason would be the presence of surface states.

Nevertheless, when comparing the ARUPS intensity maxima with theory it can be observed that the energies of B and C correspond to two DOS features located at the same energies on the calculated total DOS (labelled also B and C). This is an indication that these two ARUPS features correspond to high bulk DOS energy ranges as theory predicts.

For $Co_2MnGa$, the spectrum obtained with h$\nu$=40.8 eV (right middle) shows a narrow peak, which starts to increase directly at the Fermi energy, has a change on slope at E-$E_F$ $\simeq$-0.2 eV (labelled D) and achieves its maximum value at E-$E_F$ $\simeq$-0.75 eV (labelled E). The spectrum obtained with h$\nu$=21.2 eV (right bottom) shows the same D and E features present with h$\nu$=40.8 eV but more pronounced. Additionally, two more weak features can be distinguished at E-$E_F$ $\simeq$-1 eV (labelled F) and E-$E_F$ $\simeq$-1.6 eV (labelled G). When comparing both ARUPS spectra with the theoretical total DOS (top right) the same differences concerning broadening effects of the ARUPS intensity feature as in $Co_2FeAl_{0.3}Si_{0.7}$ are observed. The reasons are the same discussed above. However, for this case a better fit of the ARUPS intensity behaviour close to the Fermi energy with theoretical total bulk DOS features is shown. Although an intensity feature at E-$E_F$ $\simeq$-0.2 eV (labelled D) in the ARUPS spectra is not predicted by theory, the intensity of peak E increase close to the Fermi energy fit with a direct increase of the calculated total DOS at the Fermi energy. The feature labelled D is at the same energy than the feature labelled A on the $Co_2FeAl_{0.3}Si_{0.7}$ ARUPS spectra. As already discussed above, this feature can correspond to a surface state. Another possibility in this case, would be that this peak D would in reality correspond to the theoretical small bump situated just at the calculated Fermi energy, and that the Fermi energy is shifted by 0.2 eV to the right. This assumption, would make D and E peaks to fit with theoretical DOS features, however, F and G would not match anymore.

When comparing the ARUPS intensity maxima with theory it can be observed that the energies of the features E, F and G correspond to the three DOS features located at the same energies on the calculated total bulk DOS (labelled also E, F and G). This is also an indication that these three ARUPS features correspond to high bulk DOS energy ranges as theory predicts.

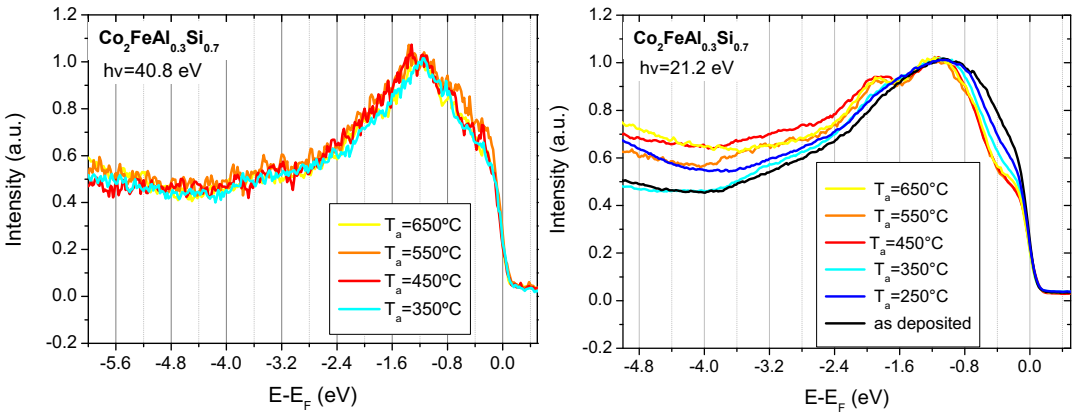


**Figure 5.7:** *UPS spectra for different annealing temperatures of thin films of the Heusler compound $Co_2FeAl_{0.3}Si_{0.7}$. The spectra change as the degree of $L2_1$ order is increasing.*

Furthermore, in order to gain a better understanding on how crystallographic disorder effects DOS features, ARUPS measurements on thin films of the Heusler compound $Co_2FeAl_{0.3}Si_{0.7}$ annealed at different temperatures were carried out. The samples were all prepared under the same conditions as described in chapter 3. Each sample was annealed at different temperatures (as deposited, 250 °C, 350 °C, 450 °C, 550 °C, 650 °C) and the UPS measurements were done directly after the annealing process in order to avoid oxidation (to achieve a "clean" surface). The RHEED images of these samples were shown in chapter 4 and revealed an improvement of the degree of order with increasing temperature. A crossover from B2 order to $L2_1$ order was observed at 450 °C.

The ARUPS spectra of the different annealed temperature $Co_2FeAl_{0.3}Si_{0.7}$thin films are shown in figure 5.7 obtained with h$\nu$=40.8 eV (left) and h$\nu$=21.2 eV (right) photon energy. At h$\nu$=40.8 eV no changes on the UPS spectra with increasing annealing temperature is observed. Due to the pronounced surface sensitivity within this photon energy (∼3.5 Å penetration depth [138]), a possible explanation could be that at the surface no changes of the crystallographic order take place. No changes on the spectra intensity features would indicate that at the very surface, no changes on the crystallographic order take place.

However, the ARUPS spectra of the differently annealed films obtained with h$\nu$=21.2 eV (figure 5.7, right), with a deeper penetration depth ∼7 Å [138], show

obvious differences. The black UPS curve corresponds to a sample which was not annealed and analysed as deposited, just B2 order is present on this sample and a broad peak without shoulder-like feature close to the Fermi edge (labelled A in left bottom graph of figure 5.6) is present. As soon as the order is improved with increasing temperature the broadening is reduced and the shoulder-like feature develops. At 450 °C (red curve), where a crossover from B2 to $L2_1$ order takes place, a double peak-like feature (labelled B and C in the left bottom graph of figure 5.6) is developed and also present at higher temperatures. Therefore, the changes of the ARUPS features, which above were concluded to be due to a high DOS, are influenced by different degrees of disorder, and it was experimentally demonstrated that disorder produces a broadening of the DOS features.

As the shoulder like feature A, which could correspond to a surface state, develops with increasing crystallographic order and it was also demonstrated that it disappears with degree of oxidation [147], it can be taken as a reference for the surface quality of the films in ARUPS measurements.

In conclusion, evidence for the validity of the predicted total bulk DOS was found. Close to the Fermi energy the energies of the maxima of the ARUPS features are in agreement with theoretically predicted energy ranges of high DOS. Additional ARUPS intensity contributions and a shoulder-like feature close to the Fermi energy observed experimentally for both Heusler thin films do not correspond to any calculated total bulk DOS. Such a mismatch with theoretical predictions could be due to the contribution of surface states in the ARUPS spectra, not predicted theoretically. The obtained broadening of the ARUPS features can be due to different factors: measurement resolution, smearing of the DOS due to strong correlations in systems with d-electrons like it is the case for $Co_2FeAl_{0.3}Si_{0.7}$ and $Co_2MnGa$ or a non perfect $L2_1$ crystallographic order. Particularly, for $Co_2FeAl_{0.3}Si_{0.7}$ it has been demonstrated that crystallographic order plays an important role for this broadening effect. The properties can be modified and controlled by sample annealing. If the order is improved, better defined ARUPS features are observed.

From the agreement between experiment and theory for $Co_2MnGa$, a high spin polarization is expected. First spin polarized ARUPS measurements on $Co_2MnGa$ result on a spin polarization of 34 % at the Fermi energy [149]. For

this measurements the samples were transferred from the deposition chamber into an SRUPS chamber with a highly efficient spin detector. Therefore, some degradation of the surface could not be avoided and could result in a reduction of the spin polarization. In order to avoid degradation of the samples during transferring the SRUPS chamber was attached to the deposition chamber and direct measurements after deposition could be performed under optimized vacuum conditions. First measurements on $Co_2MnGa$ thin films under these conditions result on a spin polarization of 60 % at the Fermi energy [151], which is the highest experimental spin polarization value obtained for this Heusler compound. This value is really close to the theoretical prediction of 67 % [81].

However, for $Co_2FeAl_{0.3}Si_{0.7}$ the highest spin polarization obtained by SRUPS amounts to 40 % [151]. This value, although it is the highest experimentally obtained for this Heusler compound, is far away from the theoretical prediction of 100 % (half-metal). One of the main reasons could be the influence of surface states on this compound which could contribute to destroy real half-metallicity.

These results are compared with the analysis of TMR values and tunneling spectroscopy on different MTJ's with $Co_2FeAl_{0.3}Si_{0.7}$ or $Co_2MnGa$ as base electrode in the next chapter.

# Chapter 6

# Tunneling Spectroscopy

In this chapter the suitability of tunneling spectroscopy as an experimental method for the observation of DOS features is evaluated. In particular, Magnetic Tunneling Junctions based on the Heusler compounds $Co_2FeAl_{0.3}Si_{0.7}$ and $Co_2MnGa$ are prepared for tunneling magneto resistance (TMR) measurements and tunneling spectroscopy. With TMR measurements, information about the spin polarization of $Co_2FeAl_{0.3}Si_{0.7}$ and $Co_2MnGa$ is obtained, as well as its temperature dependence. With tunneling spectroscopy, information about the effects that contribute to the tunneling current can be evaluated and discussed, such as the barrier potential, DOS of the Heusler compounds, the DOS of the upper ferromagnetic electrode, inelastic processes, temperature effects, etc. First, a theoretical introduction to the concept of the TMR effect and tunneling spectroscopy is given, followed by a description of the junctions preparation. Then, the experimental results are presented and discussed. Here a comparison of the experimental conductance curves with numerical calculation of the conductance obtained from eqs. 6.10 and 6.11, by modelling different shapes of the potential barrier and DOS contributions, is presented. Finally, conclusions are given.

## 6.1 Theoretical background of the TMR effect

### 6.1.1 Relation between spin polarization and TMR

Spin polarized tunneling was first discovered in 1970 by Tedrow and Merservey [152, 153]. First TMR results due to tunneling between two ferromagnetic elec-

trodes and its dependence on the relative orientation of the magnetizations of the electrodes was observed and quantitatively estimated by Jullière [4]. He described the TMR ratio in terms of the classical tunneling theory, earlier formalized by Bardeen [154]. It assumes that the two electrodes separated by an insulating barrier are completely independent systems, and the barrier is a perturbation which causes quantum transitions between them (tunneling). In this model the tunneling current which flows between two non-magnetic electrodes at a given energy E from Fermi's Golden rule results in

$$I(V,E) \propto |t(E)|^2 N_1(E-eV) N_2(E)[f(E-eV)-f(E)] \tag{6.1}$$

for an one dimensional system, where $N_1$ and $N_2$ are the total densities of states of the two electrodes, $|t(E)|^2$ is the square of the tunneling matrix element (tunneling probability) and $f(E)$ is the Fermi function. For the energy range $E \sim eV$, it is assumed that the tunneling matrix element is energy independent and therefore, the total tunneling current is the integral over the energy.

$$I(V) \propto |t|^2 \int_{-\infty}^{\infty} N_1(E-eV) N_2(E)[f(E-eV)-f(E)]dE \tag{6.2}$$

In the low bias regime and at low temperatures

$$lim_{eV\to 0}\frac{[f(E-eV)-f(E)]}{eV} = \delta(E-E_F)$$

$$\frac{dI}{dV} \propto |t|^2 N_1(E_F) N_2(E_F) \tag{6.3}$$

where $E_F$ is the Fermi energy and $\frac{dI}{dV} = G$ is the tunneling junction conductance at zero-bias. For magnetic electrodes the densities of states are now spin dependent, there is a different DOS for spin up $N^{maj}$ and DOS for spin down $N^{min}$ electrons, and consequently the tunneling current depends on the relative magnetization orientation between the two electrodes, which are either parallel or antiparallel. The Jullière model assumes spin conservation in the tunneling process, thus the tunneling of spin up and down electrons are two independent processes. Assuming that at zero magnetic field the magnetization orientation of the two electrodes is antiparallel, the conductance is

$$G(0) \propto N_1^{maj}(E_F) N_2^{min}(E_F) + N_1^{min}(E_F) N_2^{maj}(E_F) \tag{6.4}$$

and that at a saturating applied field $H_s$ the magnetization orientation of the two electrodes is parallel, the conductance is

$$G(H_s) \propto N_1^{maj}(E_F) N_2^{maj}(E_F) + N_1^{min}(E_F) N_2^{min}(E_F) \tag{6.5}$$

the tunneling magneto resistance (TMR) ratio is defined as

$$TMR = \frac{G(0)^{-1} - G(H_s)^{-1}}{G(H_s)^{-1}} = \frac{R_{antipar} - R_{par}}{R_{par}} \tag{6.6}$$

where $R_{par}$ is the tunneling resistance in the parallel configuration and $R_{antipar}$ is the tunneling resistance in the antiparallel configuration.

The spin polarization of the two electrodes are defined in terms of their spin dependent DOS as

$$P_{1,2} = \frac{N_{1,2}^{maj}(E_F) - N_{1,2}^{min}(E_F)}{N_{1,2}^{maj}(E_F) + N_{1,2}^{min}(E_F)} \tag{6.7}$$

So the TMR is related to the two electrodes spin polarization of the two electrodes by the resulting relation:

$$TMR = \frac{2P_1P_2}{1 - P_1P_2} \tag{6.8}$$

This model is successful in relating directly the tunneling current with the spin polarization of the two electrodes and the barrier is considered as a passive element with no influence on the spin polarization of the tunnelling current.

This simple model is able to give consistent results for $AlO_x$ barriers. However, it has its limitations. It is no longer valid for epitaxial barriers like MgO. Additionally, it can not predict the dependences of the TMR on the thickness and height of the insulating barrier. It is not able to describe the effects of impurities in the barrier and/or disorder at the interface between the ferromagnet and the barrier on the TMR. Also it can not explain the temperature and bias voltage dependence of the TMR. Therefore, a direct comparison of the TMR value with the spin polarization remains challenging when other aspects not included in the relation are influencing the experimental TMR value. In the following, the most important aspects that can affect the measurements are discussed.

### 6.1.2 Influence of the barrier

The TMR depends strongly on the quality of the tunnel barrier. The most succesful barrier materials have demonstrated to be $AlO_x$ and MgO. Others appear

**Table 6.1:** *Highest TMR and spin polarization values of MTJ's based on different Heusler compounds with $AlO_x$ and MgO as insulating barrier.*

| MTJ | TMR | Spin polarization |
|---|---|---|
| $Co_2MnSi/(MgAl)O_x/Co_2MnSi$ | 570% (6K) | 85% * [156] |
| $Co_2MnSi/(MgAl)O_x/Co_2MnSi$ | 67% (300K) | 50% [156] |
| $Co_2FeAl_{0.5}Si_{0.5}/AlO_x/CoFe$ | 106% (4K) | 68% [157] |
| $Co_2FeAl_{0.5}Si_{0.5}/MgO/Co_2FeAl_{0.5}Si_{0.5}$ | 390% (5K) | – † [158] |
| $Co_2FeAl_{0.5}Si_{0.5}/MgO/Co_2FeAl_{0.5}Si_{0.5}$ | 220% (300K) | – [158] |
| $Co_2MnSi - Co_2FeSi/AlO_x/CoFe$ | 114% (4K) | 70% [159] |
| $Co_2Cr_{0.6}Fe_{0.4}Al/AlO_x/CoFe$ | 101% (4K) | 67% [162] |
| $CoFeB/AlO_x/CoFeB$ ‡ | 70% (300K) | 51% [160] |
| $CoFeB/MgO/CoFeB$ | 604% (300K) | – [161] |

* *No knowledge about thickness of MgO and its influence on TMR is given.*

† *Jullière model can not be applied for epitaxial MgO barriers. Spin polarization remains unknown.*

‡ *CoFeB is not a Heusler compound. However, high TMR and spin polarization can be also achieved.*

to be non-stoichiometric and/or magnetic resulting in spin memory loss or spin scattering. The highest TMR values found in literature for different MTJ's based Heusler compounds are shown in table 6.1. As can be observed most of the highest TMR values correspond to junctions with MgO barriers. Since for the same Heusler compound (see $Co_2MnSi$ as example) two different TMR values are obtained depending on the insulating barrier, it is clear that the tunnel barrier is playing an important role for the TMR and its value is not only influenced by the spin polarization of the electrodes, but depends on the crystallographic properties of the tunnel barrier. The amorphous $AlO_x$ barrier in MTJ's provides consistent spin polarization values by means of the Jullière model. Theoretical support of the Jullière model validity for disordered barriers is given [155]. However, for the epitaxial MgO barrier another kind of considerations is necessary and the Jullière model is no longer valid. The reasons are exposed below:

- **$AlO_x$**
  This barrier is an amorphous oxide. Its structural disorder can easily generate intermediate states in the gap of the oxide. The way this disorder

affects the spin polarization of tunneling and TMR was investigated by Tsymbal et al. [155]. In this type of systems, with a high degree of disorder characterizing the insulator, the current-flow through the insulator takes place in regions with highly conducting channels for electron transport. These regions are due to the local disorder configuration and they depend on the disorder level and barrier thickness. Thus, an increase of the disorder and thickness produces a decrease on the tunneling current. The spin polarization of the tunneling current is, therefore, not only determined by the intrinsic properties of the ferromagnet, but also by the properties of the potential barrier. Therefore an optimization of the barrier is of great importance. Applying Jullière model for optimized $AlO_x$ barrier gives acceptable consistent TMR results.

Such an agreement can be understood in terms of diffusive elastic scattering due to disorder at the electrode/barrier boundary. This diffusive scattering mixes all the incoming electronic states with the same energy. Consequently the total DOS keeps invariant, since it is a property summed over states in some energy interval dE. In this description energy changes due to scattering process or spin flip are not included.

- **MgO**
  This barrier is an epitaxial oxide. Its crystalline order makes the tunneling process coherent. A high TMR in this case, does not mean a high spin polarization of the ferromagnetic electrodes, but a spin polarization of only the states with high transmission probability, since only some electronic bands are selected to take part in the tunneling process.

  This can be understood by describing the tunnel conductance as a process which strongly depends on the symmetry of the Bloch states in the electrodes and of the evanescent states in the barrier layer. The wave vector is described as $k = k_{\shortparallel} + k_{\perp}$, where $k_{\shortparallel} = k_x + k_y$ (component parallel to the interface plane) and $k_{\perp} = k_z = q + i\kappa$. $\kappa$ is the attenuation length of the evanescent wave in the barrier. The complex part of the wave vector of the evanescent states makes them form complex bands in the insulator [163, 164]. For an ordered barrier and smooth interface, conservation of the

$k_{\shortparallel}$ component can be assumed in tunneling. Tunneling consists now of a selective process where those states with the smallest $\kappa$ and energy near to $E_F$ will contribute to the tunneling current and, additionally, new effects such as resonant interface states* [165] contribute to the tunneling conductance. Such effects are a consequence of the symmetry matching among the electronic bands of the electrodes and of the electrodes and the complex bands in the insulator. This symmetry matching acts as well as *"spin selecting"* because some symmetries in the ferromagnet are only characteristic for one spin direction, so they only contribute for one of the electrode configurations, either parallel or antiparallel, and contribute in this sense to an increase or decrease of the TMR value, respectively.

From the different properties of an amorphous and an epitaxial barrier it can be concluded that an amorphous barrier gives a direct relation to the spin polarization of the ferromagnets. Since this work consist of the experimental determination of the spin polarization of $Co_2FeAl_{0.3}Si_{0.7}$ and $Co_2MnGa$, $AlO_x$ barriers are used.

### 6.1.3 Influence of the interface

The spin polarization in a MTJ is primarily determined by the electronic and atomic structure of the ferromagnet/insulator interfaces rather than by the bulk properties. Because of breaking symmetries and missing partners, DOS at the interface, which depend on terminating layer, differ from bulk. Taking into account that the mean free path of the electrons in Heusler alloys is around $\lambda \sim$20 Å, only interface information of the tunneled electrons is achieved. Consequently, the magnitude of the conductance and therefore the spin polarization of the tunneling current is effected by interface properties.

This has been theoretically demonstrated. Modelling small variations in the atomic potentials and hopping integrals near the interface resulted in a strong and unexpected effect on the shape of the interface DOS and, hence, on the con-

*Resonant interface states, known as "hot spots" as well, are states in the barrier that allow electrons with their $k_{\shortparallel}$ values to tunnel through the junction with very little or not attenuation at all. It is an effect which occurs only in the minority band of the ferromagnet. Such an effect vanishes for large barrier thickness where the conductance for $k_{\shortparallel}$ is suppressed [165, 166, 167].

ductance [168].

The relevance of the interface properties has also been experimentally demonstrated in several experiments by introducing dusting layers at the interface [169, 170, 171]. They showed how the TMR ratio falls exponentially with the thickness of the dusting layer for the first atomic layers and the decay becomes slower for larger thickness.

Additionally, surface roughness of the bottom ferromagnetic electrode can lead to dipolar or orangepeel coupling between the bottom and top ferromagnetic electrodes giving rise to a non-independent switching between them [172]. Growing a thin insulator on a rough surface results in a non-uniform coverage of the insulator. Hence, the tunnelling process becomes unstable due to the formation of hot spots at the interface which entail an enormously high current density in these regions, giving as a result a premature breakdown of the junction.

In order to avoid these problems, an optimization of the quality of the surface of the ferromagnet is required as well as a good crystallographic order and smoothness and an optimization of the oxidation conditions of the barrier, in order to avoid oxidation of the first monolayers of the ferromagnet or Al layers at the interface which are not completely oxidized. Although different experimental methods and analysis techniques (like RHEED or STM) have helped to improve the interface quality, experimentally achieving a perfect interface in a MTJ device is challenging.

### 6.1.4 Defects and impurities

Magnetic impurities at the barrier originate elastic spin-flip processes. Scattering by these imperfections leads to a loss of the spin orientation of the electrons [173].

When a spin-flip event occurs in the barrier, it is as if the magnetization of electrode 2 has been reversed, i.e., they exhibit an inverse magnetoresistance. Denoting their fraction by $f$ , the conductance for parallel magnetization becomes $(1-f)Gp + fGap$ and similarly for the antiparallel case, leading to

$$TMR = \frac{(1-2f)\cdot TMR^0}{1-f\cdot TMR^0} \tag{6.9}$$

Increasing defect concentration in the barrier increases the spin flip rates. Thus, the magnetoresistance is reduced linearly with the fraction f and could even vanish. This behaviour has been studied on Co/$AlO_x$/NiFe junctions [174] showing a linear decrease of TMR with dopant thickness explained by equation 6.9.

Additionally, magnetic impurities at the interface between ferromagnet and insulating barrier can make an electron, which tunnels innelastically through the barrier to flip its spin. Because of the coupling between the localized state and the ferromagnet, the process contributes to a magnon excitation in the bulk of the ferromagnet [175].

This inelastic spin flip processes do not reduce the magnetoresistance at zero temperature and zero voltage, but give rise to non ohmic effects at finite voltages, and to changes in the conductance as a function of temperature [173].

## 6.2 Theoretical background of tunnelling spectroscopy

The dependence of the tunneling current between two metals separated by an insulating barrier on an applied bias voltage has no ohmic behaviour. It has been demonstrated that the dependence on the tunnelling current should be directly proportional to the applied voltage for voltages very much less than the barrier height and should exponentially increase with voltage when the voltage becomes comparable to the barrier height. This is because as the bias voltage increases, the barrier changes it shape, allowing the higher energy states to tunnel more easily [176].

Assuming the WKB approximation[†] inside the barrier the tunneling current density is given by the following expression [177]

$$j = \frac{4\pi e}{\hbar} \sum_{k_\perp} \int_{-\infty}^{\infty} dE_z N_1(E) N_2(E - eV) P(E_z) \times [f(E) - f(E - eV)] \quad (6.10)$$

where $N_1(E)$ and $N_2(E)$ are the DOS for a given transverse momentum $k_\perp$ and total energy E for the upper and bottom electrodes, $f(E)$ is the Fermi distribution

[†]In the WKB approximation it is assumed that the band structure of the metal-insulator-metal system only varies slowly compared to the electron wavelength.

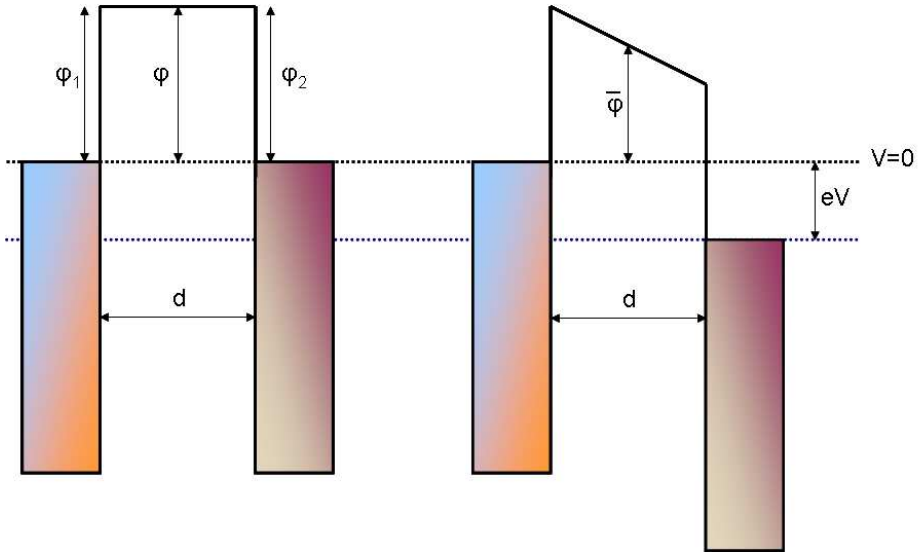


**Figure 6.1:** *Simmons' model of a tunneling barrier.* ***Left:*** *Barrier shape when no bias voltage is applied.* ***Right:*** *Barrier deformed due to an applied bias voltage. A eV shift of the Fermi energy takes place.*

function and $E_z$ is the total energy in the direction perpendicular to the barrier. $P(E_z)$ is the tunneling probability which depends on the barrier and bias voltage as follows

$$P(E_z) = exp\left(-\frac{2}{\hbar}\int_0^d \{2m[\varphi(z',V) - E_z]\}^{\frac{1}{2}} dz'\right) \tag{6.11}$$

where d is the barrier thickness and $\varphi(z,V)$ the barrier height. The current flow from one electrode to the other exponentially decreases with the barrier height $\varphi$. The total net current corresponds to the sum of two currents flowing in opposite directions.

Experimentally, the differential conductivity dI/dV is most commonly measured because, by making use of a lock-in amplifier technique, a very sensitive and low-noise determination of this magnitude is achieved.

The dependence of the differential conductivity on the bias voltage was previously modelled by Simmons [178], who assumed a symmetric rectangular barrier, $\varphi(x,eV) = \varphi(eV)$(figure 6.1, left), which gets deformed in a trapezoidal shape (figure 6.1, right) when a bias voltage is applied. He came to the following ex-

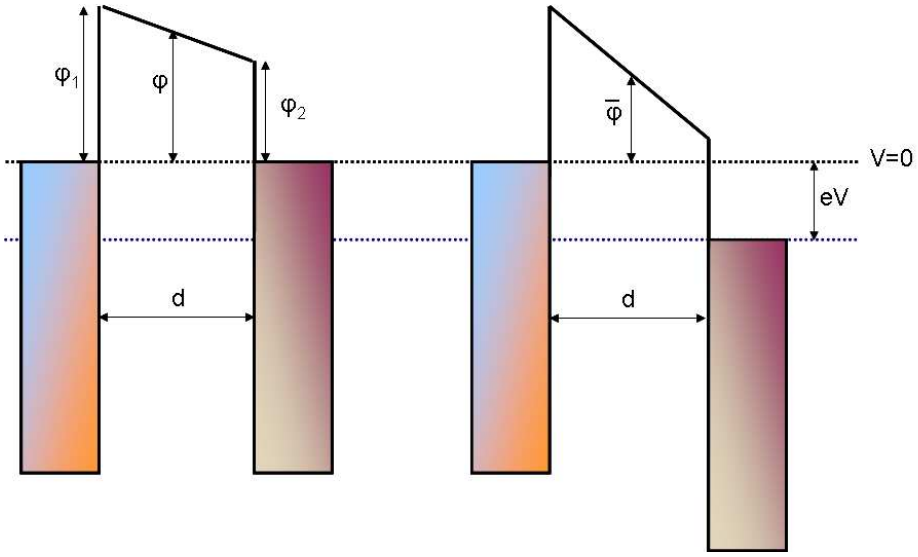


**Figure 6.2:** *Brinkman's model of the tunneling barrier.* ***Left:*** *Barrier shape when no bias voltage is applied. An asymmetry of the barrier at zero bias voltage is considered.* ***Right****: Barrier deformed due to an applied bias voltage. A eV shift of the Fermi energy takes place.*

pression:

$$\frac{dI/dV(V)}{dI/dV(0)} = 1 + 3\gamma V^2 \tag{6.12}$$

where $\gamma \approx \dfrac{0.0115}{\bar{\varphi}} d^2$ when d and $\bar{\varphi}$ are given in Ångstroms and Volts, respectively. This expression results in a symmetric parabolic dependency of the differential conductance on the bias voltage, which fits with the parabolic behaviour obtained experimentally. However, this simple model is not able to explain the experimentally observed asymmetry in the parabola with respect to the bias voltage sign. Such an asymmetry was explained later by Brinkman et al. [179], who described the differential conductivity by taking into account the possibility of having asymmetrical barriers due to the presence of two different electrodes on each side of the barrier, $\varphi(x, eV) = \varphi_1 + (x/d)(\varphi_2 - eV - \varphi_1)$ as shown in figure 6.2 This more realistic description results in the following expression for the differential conductivity:

$$\frac{dI/dV(V)}{dI/dV(0)} = 1 - \left(\frac{eA_0\Delta\varphi}{16\varphi^{\frac{3}{2}}}\right) V + \left(\frac{9A_0^2e^2}{128\bar{\varphi}}\right) V^2 \tag{6.13}$$

where $A_0 = 4(2m)^{\frac{1}{2}}d/3\hbar$, $dI/dV(0) = 3.16 \times 10^{10}(\bar{\varphi}^{\frac{1}{2}}/d)exp(-1.025d\bar{\varphi}^{\frac{1}{2}})$, the asymmetry $\Delta\varphi = \varphi_1 - \varphi_2$ and $\bar{\varphi} = (\varphi_1 + \varphi_2)/2$. It is important to point out that $d$ and $\varphi$ are parameters related to the potential barrier and not to the width of the physical barrier of the junction and that these two models are only valid for voltage ranges where $eV < \bar{\varphi}$. Moreover, for high voltage values heating effects may also contribute to the conductance.

Both models allow an evaluation of the barrier parameters and their influence on the tunneling conductance curve by taking only barrier properties into account. It is known, however, that the tunneling conductance also depends on the DOS of the two electrodes and inelastic tunneling processes. In principle, by measuring experimentally the differential conductivity of this type of systems, the barrier contribution is obtained by fitting the curve to the theoretical models. By using Brinkman's model, the differential conductivity is fitted to a polynomial function of second order, $dI/dV(V) = A + B \cdot V + C \cdot V^2$, which, together with equation 6.13, gives information about the potential barrier parameters:

$$\bar{\varphi} = \sqrt{\frac{A}{32C}}e \cdot ln\left(\frac{h^3 \cdot \sqrt{CA}}{\sqrt{2}\pi e^3 m}\right) \tag{6.14}$$

$$d = -\frac{\hbar}{8\sqrt{\bar{\varphi}m}} \cdot ln\left(\frac{h^3 \cdot \sqrt{CA}}{\sqrt{2}\pi e^3 m}\right) \tag{6.15}$$

$$\Delta\varphi = -\frac{12\hbar\bar{\varphi}^{\frac{3}{2}}B}{\sqrt{2m}edA} \tag{6.16}$$

Typically, other effects also contribute to the tunneling conductance: inelastic processes like spin flip processes due to impurities at the interface or magnon excitations, and DOS contribution of the electrodes. As a consequence, a good fitting of the curve by means of models which only takes barrier shape into account is not possible. Other considerations for the evaluation have to be done. With respect to the observation of DOS contributions on the shape of the differential conductivity curve, only strong DOS features close to the Fermi energy could be observed in the dI/dV-V curve. By extracting the barrier contribution from the fit of the curve, information about them can be obtained. The reason why only strong DOS features can be observed is that the quadratic term in the parabolic dependence of dI/dV with bias voltage blurs out DOS effects. Additionally, the contribution of inelastic processes could be strong and cover all

DOS contributions. Moreover, the measurement is limited by the barrier quality. The presence of pinholes in the barrier induces high local current densities which generate heat when a voltage is applied across the junction. The heat induces atom migration from the electrode to the barrier and its consequent degradation. Thus, the applicable voltage is limited by barrier degradation which produces breakdown processes at the barrier [180, 181]. Although all these effects make the analysis of these curves challenging, qualitative information can be achieved as will be shown. The evaluation of these curves are explained more in detail in the subsection about tunneling spectroscopy results 5.4.1.

## 6.3 Experiment

### 6.3.1 Magnetic tunnelling junction design

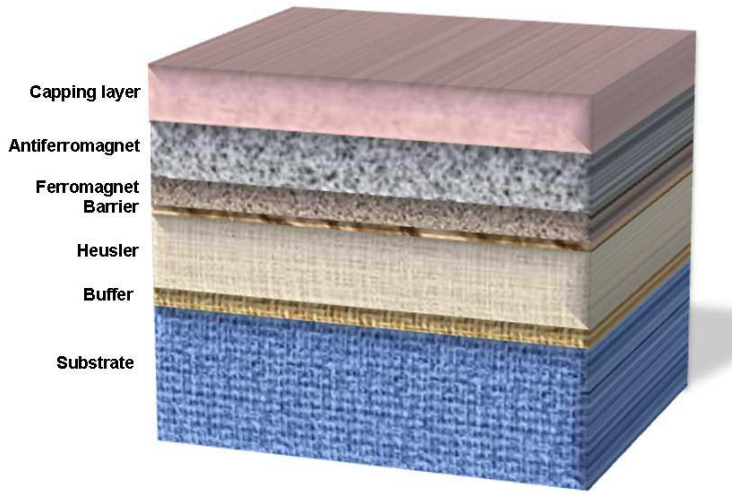


**Figure 6.3:** *Scheme of the multilayered structure which forms the magnetic tunnelling junction.*

The magnetic tunneling junctions prepared in this work consist of multilayers (figure 6.3). A MgO substrate is needed for allowing an epitaxial growth of the Heusler compounds. Then, a MgO buffer layer is deposited by electron beam evaporation in the MBE to improve the epitaxial growth of Heusler thin films compared to a direct deposition on the MgO substrate. A thin $Co_2FeAl_{0.3}Si_{0.7}$

or $Co_2MnGa$ film is deposited by sputtering on the MgO buffer layer to use it as bottom electrode of the magnetic tunnel junction with the aim to investigate its characteristics as a high spin polarization material. Then, a very thin tunneling barrier of $AlO_x$ is deposited. First, 2.5 Å of Mg as a seed layer are deposited by rf-sputtering in chamber B, consecutively Al is deposited by rf-sputtering in the same chamber. The oxidation process also takes place here. The deposition thickness of Al and the oxidation time was varied from 10 Å to 18 Å and from 8 s to 15 s, respectively, in order to optimize the parameters which entail the highest TMR effect. The 2.5 Å of Mg deposition is explained and justified in subsection 5.2.2. Finally, the top electrode is deposited. Here two different types of MTJ's are investigated. On one hand, conventional MTJ's, with another ferromagnetic material as upper electrode in order to measure the TMR effect, are prepared. On the other hand, in order to be able to relate tunnelling spectroscopy curves with only the DOS of the Heusler compound under study, an upper electrode material, whose DOS can be consider constant at low temperatures such as a noble metal, is used.

Therefore, for the first type of MTJ's a CoFe ferromagnetic top electrode is sputtered in chamber A, followed by MnFe layer deposited by rf-sputtering. This MnFe is a thin antiferromagnetic layer which pins the CoFe ferromagnetic layer due to exchange bias. The exchange bias is created ex-situ and explained in subsection 5.2.4. This pinning of the magnetization of one of the electrodes is needed to observe the maximum TMR effect, which appears when there is an antiparallel configuration of the magnetization of both electrodes, CoFe and $Co_2FeAl_{0.3}Si_{0.7}$ or $Co_2MnGa$. The effect depends on the thickness of the ferromagnetic and the antiferromagnetic layer. Typically, a minimal thickness is necessary to observe the effect. In this work and after parameter optimization, 40 Å of CoFe and 150 Å of MnFe are deposited. Finally, 200 Å of a thin Au layer were deposited to protect the MTJ's during the lithography process.

For the second type of MTJ 200 Å of Au layer were deposited directly after oxidation of the $AlO_x$ tunnelling barrier.

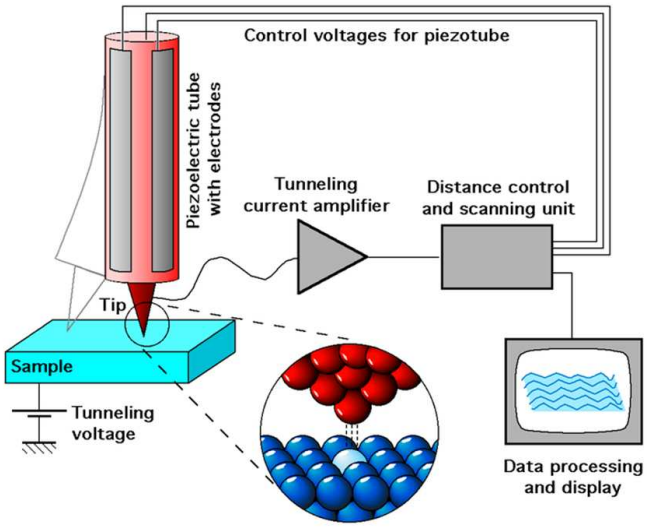


**Figure 6.4:** *Schematic description of STM [182].*

### 6.3.2 Morphology analysis by Scanning Tunneling Microscopy (STM)

Morphology and topology are relevant properties of the samples. This information helps to understand the relation between growth, structure, order and transport properties in a MTJ. TMR measurements strongly depend on the interface properties of the MTJ. As already studied with UPS in chapter 5, disorder at the surface reduces the spin polarization. Additionally, when the roughness of the interface increases, the number of the scattering processes also does, and in consequence the TMR ratio decreases. As a result of the roughness, a small spin polarization is calculated. Moreover, the small thickness of the insulating barrier requires a smooth surface to reduce pinholes defects which result in leaking direct currents. Hence, the importance of the study of the surface morphology and topology of the films.

With STM the morphology of the films is analysed. It is based on the concept of quantum tunnelling. When a conducting tip is brought very near to a metallic or semiconducting surface, a bias between both can allow electrons to tunnel through the vacuum between them. The resulting tunnelling current is a function of tip position, applied bias voltage and local DOS of the sample. Information is obtained from monitoring the current as the tip scans across the

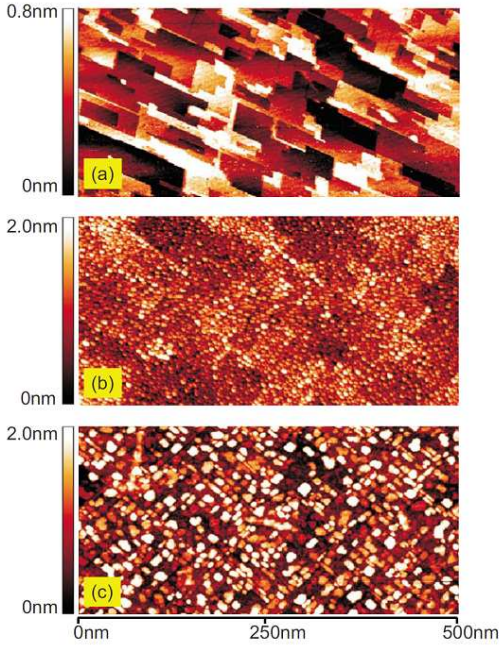


**Figure 6.5:** *In situ STM images. (a) $Co_2Cr_{0.6}Fe_{0.4}Al$ thin film after annealing, (b) 18 Å of Al deposited on an aged $Co_2Cr_{0.6}Fe_{0.4}Al$ surface, and (c) 18 Å of Al deposited on a fresh $Co_2Cr_{0.6}Fe_{0.4}Al$ surface [162].*

surface. Variations on the surface morphology induce corrections on the piezo-electrictube to keep the distance between tip and surface and current constant. These adjustments produce feedback signals resulting into colour changes in an image (see figure 6.4).

STM analysis is used in order to optimize and improve smoothness and growth not only of the Heusler thin films, but also of the $AlO_x$ tunnelling barrier.

An optimization of high quality Heusler compounds based MTJ's was carried out in previous work by C. Herbort [108]. In particular, STM analysis of the $Co_2Cr_{0.6}Fe_{0.4}Al/AlO_x$ surface morphology revealed its influence on TMR results [162]. The results justify the actual preparation method used for the tunnelling barriers of MTJ's and therefore, the analysis and conclusions are exposed here.

The $Co_2Cr_{0.6}Fe_{0.4}Al$ deposition parameters were optimized in order to achieved an improved surface morphology as shown in figure 6.5 (a). The Heusler film

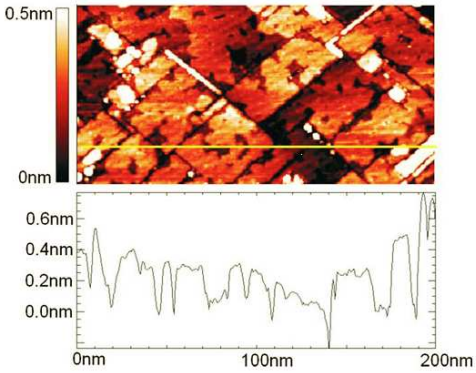


**Figure 6.6:** *Upper image: in situ STM image of 2.5 Å of Mg seed layer on a $Co_2Cr_{0.6}Fe_{0.4}Al$ surface. Lower image: height profile along the yellow line indicated in the upper image [162].*

present a smooth surface with squared-shaped terraces. The morphology is changed when Al is deposited on the Heusler surface and it is strongly influenced by the vacuum condition before deposition. The formation of islands, which is a non suitable morphology for tunnelling barriers, can be observed in figure 6.5 (b) for 18 Å of Al deposited on an aged $Co_2Cr_{0.6}Fe_{0.4}Al$ surface and (c) for 18 Å of Al deposited on fresh $Co_2Cr_{0.6}Fe_{0.4}Al$ surface, and it indicates that Al has unfavourable wetting properties on the Heusler surface.

STM analysis revealed a drastic improvement of the surface morphology of the $AlO_x$ when inserting a very thin layer of 2.5 Å of Mg at the interface (figure 6.6). The Mg acts as a seed layer between the Heusler layer and $AlO_x$ and improves the wetting properties without degrading the Heusler surface or generating spin flip scattering centers for the tunnelling electrons. Additionally, due to its high reactivity, it will oxidized with the Al during the oxidation process to originate the insulating barrier. With the deposited Mg layer the STM images showed additional covered squared-shape terraces with curved defects, whose depth correspond to the Mg layer thickness (2-3 Å). This improvement resulted in a pronounced enhancement of the TMR, 101 %, which is the highest TMR published up to now for the Heusler compound $Co_2Cr_{0.6}Fe_{0.4}Al$.

In order to find out if the TMR value is still dominated by the polycrystalline $AlO_x$ barrier and its enhancement is due to its improved morphology, MTJ's with

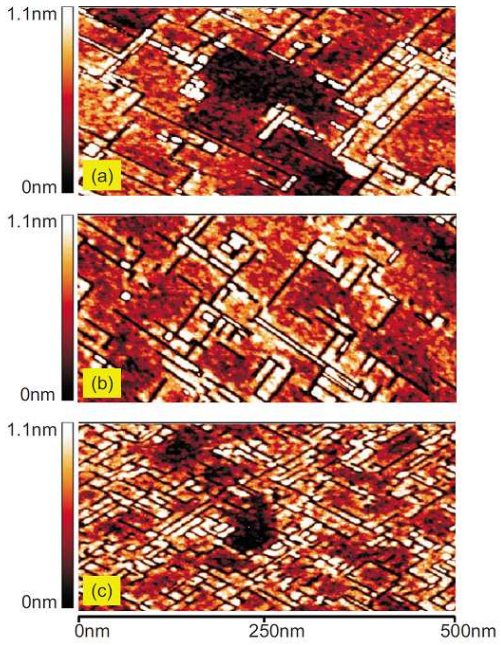


**Figure 6.7:** *In situ STM images of 18 Å of rf-sputtered Al on (a) 2.5, (b) 5.0, and (c) 7.5 Å of Mg on $Co_2Cr_{0.6}Fe_{0.4}Al$ thin films [162].*

18 Å of Al on Mg layers with different thickness were performed, 2.5 Å, 5.0 Å and 7.5 Å. The STM images of the Al surface on top of Mg (figure 6.7) revealed a smooth surfaces form by square-shaped terraces with deep trenches. An increase of the trench density with increasing Mg thickness is observed. The origin of these trenches could be due to grain boundaries of the Mg seed layer which are related to the $Co_2Cr_{0.6}Fe_{0.4}Al$ surface morphology.

The TMR values measured at 4 K for 18 Å of $AlO_x$ barrier on Mg layers with different thickness are plotted in figure 6.8. The maximum TMR is obtained for the thinnest Mg layer (2.5 Å). Therefore, the Mg only acts as a seed layer and does not influence the TMR due to coherent tunnelling, i.e. the polycrystalline properties of $AlO_x$ dominate the tunnelling process.

101 % TMR corresponds to a $Co_2Cr_{0.6}Fe_{0.4}Al$ spin polarization of 67 % when a 50 % spin polarization for CoFe (upper electrode) is assumed. Taking into account that $Co_2Cr_{0.6}Fe_{0.4}Al$ thin films grow with B2 order and that theory predicts 77 % spin polarization for this type of disorder [67], a relatively close approach

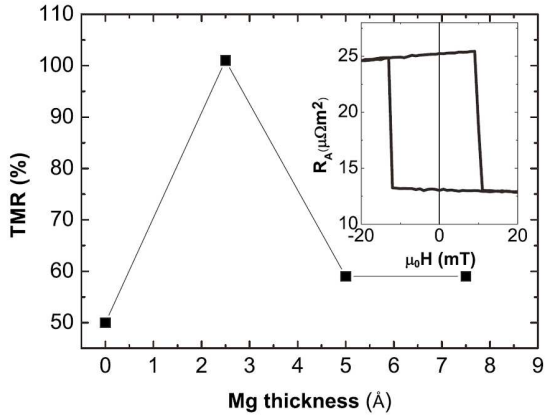


**Figure 6.8:** *Dependence of the TMR on the Mg layer thickness of $MgO/Co_2Cr_{0.6}Fe_{0.4}Al/Mg/AlO_x$(18 Å)/CoFe/MnFe/Ag tunnelling junctions. The inset shows the magnetoresistance loop of the junction with a Mg thickness of 2.5 Å [162].*

to the theoretical predictions can be concluded.

Accordingly, the same procedure for the MTJ's based on $Co_2FeAl_{0.3}Si_{0.7}$ and $Co_2MnGa$ was used here.

### 6.3.3 Lithography

A detailed description of the preparation of mesa structures can be found in [183], little changes due to the shape of the mesa and the ion etching were done and are specified in [108]. The same procedure as in [108] has been followed in this work. A short description of the complete process is mentioned here. The parameters of the procedure are specified in appendix B.

The multilayer samples were prepared as described before in order to create a magnetic tunnelling junction. The current flows perpendicular to the sample surface and for measuring it a special structure is designed: a square-shaped mesa for optical lithography.

As soon as the MTJ film preparation is finished, the sample is taken to the clean room to start the lithography process. First, the sample is covered with a positive photoresist using a spinner, followed by a soft annealing to dry it. When

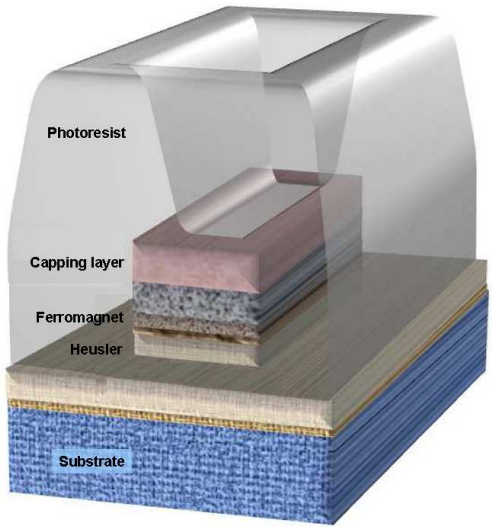


**Figure 6.9:** *Schematic view of a* $160 \times 80 \mu m^2$ *tunnel contact structure after lithography.*

it is cooled to room temperature, the photoresist is illuminated with UV light using a specific shadow mask with square shape. The UV light exposure induces a change in the chemical properties of the photoresist and the non-illuminated areas can be removed with an appropriate liquid developer. Thus the square shape of the photoresist is obtained.

The photoresist free area is removed by etching in an Argon/Oxygen ion etching chamber. The ion beam is a mixture between Argon and Oxygen in a 4/1 relation and hits the sample surface alternating between 86 and 50 degrees with respect to the sample surface every 2 minutes and the sample rotates during this process to remove material evenly. The process is done in this way in order to remove material from the edges and to avoid the possible re-accumulation of etched particles on the edges, which would produce shortcircuits between upper and lower electrodes. The oxygen is used to oxidized the possible re-accumulated particles and therefore avoid shortcircuits. By etching, at the same time, a reference sample with the same thickness as the top electrode, the quantity of material removed can be controlled. Hence, when the substrate of the reference sample is visible, it indicates that the top electrode is completely etched. The etching is continued for additional 20% of the removing time of the top electrode to etch the tunnelling barrier as well and be sure that it reaches the bottom electrode.

Now, the positive photoresist can be removed with acetone. The Au capping layer is relevant because without it the photoresist reacts with the MnFe layer in a way that it is not possible to remove it at all.

Then, negative photoresist with very good insulating properties is put on the sample by using the spinner again. A shadow mask with smaller square shape on the mesa and square shape in the corner is used. With this photoresist the illuminated areas are removed by the developer giving as a final result the structure shown in figure 6.9. Such a tower multilayer structure is called *"mesa"* structure. This shape avoids shortcircuits while making connections between top and bottom electrodes and at the same time it protects the whole sample from external contaminants. By using silver glue, copper wires used to perform the measurements are attached to the samples. On a substrate of $10 \times 10\ mm^2$ 6 square mesas with three different dimensions, $100 \times 100 \mu m^2$ (called A and B), $160 \times 80 \mu m^2$ (called C and D) and $60 \times 60 \mu m^2$ (called E and F), are patterned.

### 6.3.4 Exchange Bias

For TMR measurements, one of the ferromagnets which form the MTJ fixes its magnetization orientation while the other keeps flexible to switch from one orientation to the opposite one allowing a parallel and antiparallel configuration.

To provide a proper work of the switching mechanism, the coercitive field ($H_c$) values between both ferromagnets must differ. Such a difference is achieved by setting an exchange bias for one of the electrodes. In this particular case, the CoFe electrode is fixed while the Heusler electrode is able to switch.

Exchange bias is an exchange-interaction effect which takes place at the interface between two magnetic materials, one a ferromagnet (CoFe) and the other an antiferromagnet (MnFe). The hard magnetization behaviour of the antiferromagnetic film causes a shift in the magnetization curve of the ferromagnetic film. Although not all the physical background is well understood, it is a often used method for the stabilization of magnetic materials [184].

An antiferromagnetic material is characterized by a very small or no net mag-

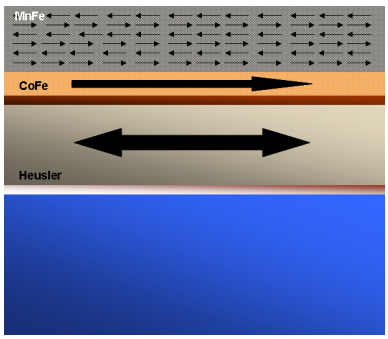


**Figure 6.10:** *Schematic figure of the exchange bias process. The magnetization orientation of the Heusler can switch while the CoFe one is fixed via MnFe.*

netization. Thus, its spin orientation is weakly influenced by an externally applied magnetic field (H). A ferromagnet is coupled to the antiferromagnet and consequently its spins are pinned. A reversal of the magnetization orientation of the ferromagnet requires extra energy corresponding to the energy necessary to create a Néel domain wall within the ferromagnetic film. This energy implies a shift in the switching field of the ferromagnet. Therefore, in an exchange-biased ferromagnetic film, the magnetization curve is shifted away from the H=0 axis by an amount $H_e$ (exchange-bias field) which is proportional to the energy cost and inversely proportional to the thickness of the ferromagnet. It has also been demonstrated that defects at the interface plays an important role for the strength of the exchange-bias effect, as well as magnetic pinning in the antiferromagnet [185]. Therefore, for a correct description of the exchange-bias, surface effects have to be taken into account [186].

Experimentally the exchange bias is created after the lithography process in a small vacuum chamber in the presence of a magnetic field of 200 mT applied parallel to the sample surface (in-plane). The junction is heated above the Néel temperature ($T_N$). $T_N$ for MnFe is 217 $°C$ and consequently the samples are annealed up to 250 $°C$. Above $T_N$ the moment of the magnetically ordered ferromagnet applies an effective field to the antiferromagnet as it is ordered, breaking the symmetry and influencing formation of domains. Hence, the direction of the exchange bias is set and the sample can be cooled down. A schematic figure of how exchange bias looks like after this process is shown in figure 6.10.

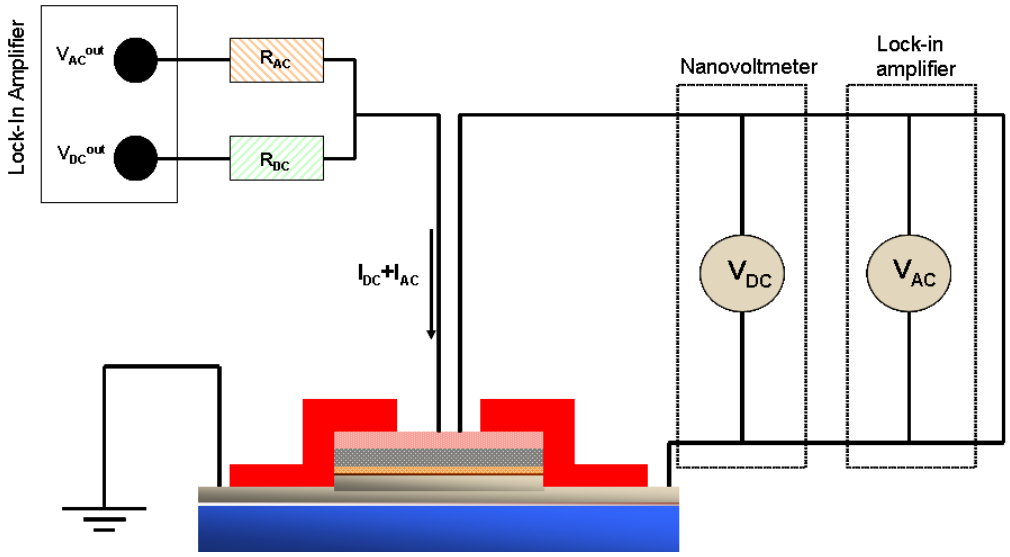


**Figure 6.11:** *Schematic representation of the ac-modulation technique used for tunneling spectroscopy measurements.*

### 6.3.5 Measurement technique

In order to carry out the TMR and tunneling spectroscopy measurements, the connections between upper and lower electrodes are made by using very thin copper wires, silver glue for the contacts and a microscope to make the connections. An schematic representation of the experimental setup used for the TMR and differential conductivity measurements is shown in figure 6.11. For a very sensitive and low-noise direct determination of dI/dV a standard lock-in technique was used. The measurements were performed with the samples placed inside a standard cryostat to perform low temperature measurements. Using a lock-in amplifier the ac-modulation technique uses a current through the junction which is the sum of a dc-current $I_{dc}$ and an ac-current $I_{ac}sin(\omega t)$ generated by the sinus voltage output of the lock-in amplifier. Since the ac component is much smaller than the dc one, a Taylor expansion of V(I) around $I_{dc}$, with the ac-current as small perturbation, is considered:

$$V(I_{dc}+I_{ac}sin(\omega t)) = V_{dc}+V_{ac}+...=V(I_{dc})+\frac{\partial V}{\partial I}|_{I_{dc}}I_{ac}sin(\omega t)+... \quad (6.17)$$

where the inverse of the ac-voltage is directly proportional to the differential tunneling conductivity.

The dc and ac currents are generated by the output voltages of the lock-in amplifier which are connected in serial to two independently tunable resistances $R_{DC}$ and $R_{AC}$, which must be much larger than the junction resistance to get an ideal modulated current output. The DC and AC voltage drop across the junction, $V_{dc}$ and $V_{ac}$, are measured via a nanovoltmeter and the lock-in amplifier, respectively (see figure 6.11).

## 6.4 Results

### 6.4.1 Tunneling Magneto-Resistance (TMR)

For TMR measurements, series of MTJ's with different barrier thickness were prepared. TMR very critically depends on the quality of the tunnel barrier. The barrier thickness was changed in order to find the best parameters which enhanced TMR values. For such a purpose, the thickness of Mg, Al and the oxidation time are the variable parameters. Playing with these parameters the barrier properties can be improved. When growing Al on top of the Heusler surface different situations could be present. When the barrier is too thin the Heusler surface can get oxidized during barrier formation increasing the spin scattering, whereas when the barrier is too thick no tunneling current could be measured at all. Typical barrier thickness for MTJ are around 10-22 Å. Another important issue is the Mg seed layer thickness, which should not be too thick in order to ensure that the tunneling process is still dominated by the effect of the amorphous $AlO_x$ barrier. The maximal thickness used in this case was 10 Å. The oxidation time is of major importance in order to achieve a perfect insulating oxide barrier. A not sufficient oxidation time results on an underoxidized barrier with a non-magnetic metal at the interface. Consequently, the tunneling electron polarization is reduced and hence the TMR. A longer oxidation can result in an overoxidation which will again increases spin scattering due to Heusler surface oxidation. Additionally, for the Heusler compound $Co_2FeAl_{0.3}Si_{0.7}$ two different annealing temperatures were used in order to vary the interface quality: 450 °C and 550 °C. For TMR measurements CoFe is used as upper electrode.

Besides TMR measurements, the temperature dependence of tunnel resistance measurements was investigated. The resistance behaviour with temperature is characteristic not only for junctions with magnetic electrodes, but also for stan-

dard junctions with non-magnetic electrodes. Although, in general, the change in junction resistance with temperature differs from one material to the other, a weak insulator like temperature dependence of the resistance is expected. This weak resistance dependency is one of the usually applied Rowell's criteria [187]. The other criteria are the exponential barrier thickness dependence of the resistance and the non-linear behaviour of the I-V or dI/dV-V relation. The latter should follow a parabolic behaviour which can be fitted by considering a trapezoidal shape of the barrier, as described by Brinkman et al. [179] and later discussed in more detail. However, these criteria are not sufficient to describe tunneling conductance or resistance behaviour with temperature or bias voltage because they are not able to describe the effects of pinholes or other conductivity contributions which are not spin dependent.

Pinhole effects on tunneling junctions have been already studied [188, 189]. They are material dependent and contribute to a reduction of the tunnel resistance and a weaker temperature dependence (hence a weaker temperature dependence is not always an indication of a better barrier). Thus, although tunneling still dominates the electron transport, they contribute to the conduction properties. An increase of the number of pinholes can result in an ohmic-like conduction which dominates the transport. A MTJ with a pinhole can be modelled as a tunnel magnetoresistor in parallel with an ohmic resistor.

A model which describes the conductance in MTJ's as the sum of a polarization dependent direct elastic tunneling part, due to the magnetization contribution of the magnetic electrodes, and a non-polarization dependent part, $G_{SI}$, has been put forward by Shang et al. [190]:

$$G(\theta) = G_T\{1 - P_1P_2cos\theta\} + G_{SI}$$

$$TMR = \frac{2P_1P_2}{1 - P_1P_2} \cdot \frac{G(\theta = 180)}{G(\theta = 180) + G_{SI}} \tag{6.18}$$

where $\theta$ is the angle between the magnetization directions of the two electrodes ($\theta = 0°$ or $\theta = 180°$ for parallel or antiparallel magnetizations, respectively); $G_T$ is the prefactor for direct elastic tunneling; and $P_1$ and $P_2$ denote the effective tunneling electron spin polarizations of the ferromagnets. Each of these two contributions depend in a different way on temperature. While for the elastic tunneling part the temperature dependency is explained by thermal spin wave

excitations, $P(T) = P_0(1 - \alpha T^{3/2})$, where $\alpha$ is the material dependent constant, the $G_{SI}$ term is proportional to $T^{\gamma}$, where $\gamma$ depends on the number of localized states N associated to imperfections in the $AlO_x$ barrier.

$$\gamma(N) = N - [2/(N+1)] \tag{6.19}$$

This dependence on T of the spin-independent contribution to the conductance is theoretically deduced assuming a sufficient density of imperfections to provide a noticeable hopping conductance through the associated localized states [191]. It originates from phonon emission or absorption at the transition from the first to the next localized state along the chain, to overcome the energy difference between the two levels.

A previous study on the temperature dependence of the tunnel resistance and TMR on Heusler based MTJ's compounds by means of this model, however, revealed that the experimental curve still deviates from the curve obtained with the model [108]. Therefore, there are additional contributions that affect the tunneling conductance and its dependency on temperature which are not included in this model. These other contributions will be discussed later together with the tunneling spectroscopy results.

First, the results for $Co_2FeAl_{0.3}Si_{0.7}$ and $Co_2MnGa$ are analysed separately and later compared.

For $Co_2FeAl_{0.3}Si_{0.7}$ the temperature dependence of the tunnel resistance was measured in absence of external magnetic fields for different barrier thicknesses (Mg and Al thickness was varied). This analysis was done for junctions with $Co_2FeAl_{0.3}Si_{0.7}$ annealed at 550 °C (figure 6.13 left) and 450 °C (figure 6.12 left). The letters A, B, C, D, E or F in the figure inset refer to the mesa areas described in the lithograhpy process section. A weak linear decrease of the resistance with increasing temperature is observed in both cases. While for the different 450 °C annealed junctions the resistance behaviour with temperature is almost the same (a reduction on the resistance of 20 %), the different 550 °C annealing junctions, however, show different decreasing resistance behaviour (a reduction which varies between 20 % and 60 %). A reduction of 20 % at is the usual resistance reduction with increasing temperature for Heusler alloys based MTJ's, obtained also, e. g. for $Co_2Cr_{0.6}Fe_{0.4}Al$ in previous work [108]. A stronger reduction would be an

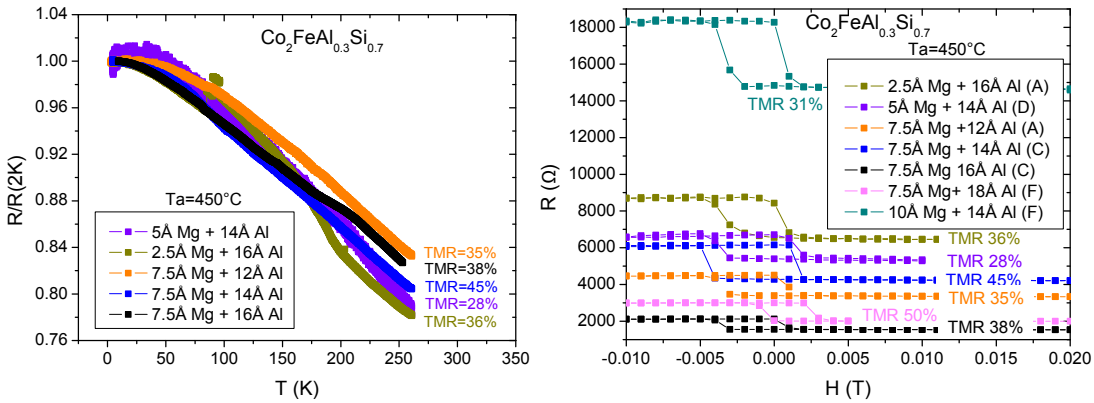


**Figure 6.12:** ***Left:*** *Temperature dependence on tunnel resistance normalized by the lowest temperature of $Co_2FeAl_{0.3}Si_{0.7}$ based MTJ's with different barrier thicknesses absence of external magnetic field.* ***Right:*** *TMR of $Co_2FeAl_{0.3}Si_{0.7}$ based MTJ's with different barrier thicknesses and different mesa areas: A ($100 \times 100\mu m^2$), C, D ($160 \times 80\mu m^2$) and F ($60 \times 60\mu m^2$). The annealing temperature of the $Co_2FeAl_{0.3}Si_{0.7}$ base electrode amounts to 450 °C.*

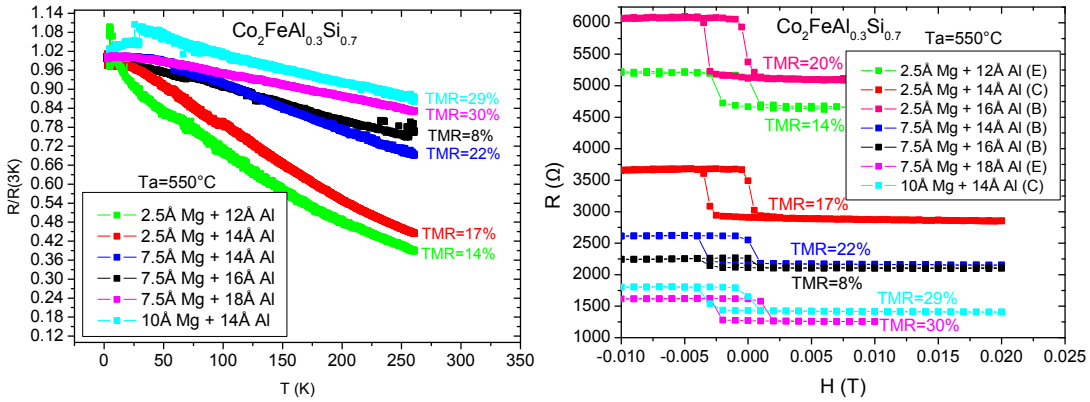


**Figure 6.13:** ***Left:*** *Temperature dependence on tunnel resistance normalized by the lowest temperature of $Co_2FeAl_{0.3}Si_{0.7}$ based MTJ's with different barrier thicknesses in absence of external magnetic field.* ***Right:*** *TMR of $Co_2FeAl_{0.3}Si_{0.7}$ based MTJ's with different barrier thicknesses and different mesa areas: B ($100 \times 100\mu m^2$), C ($160 \times 80\mu m^2$) and E ($60 \times 60\mu m^2$). The annealing temperature of the $Co_2FeAl_{0.3}Si_{0.7}$ base electrode amounts to 550 °C.*

indication of a reduced barrier quality. In our case, the larger resistance decrease correspond to the two smallest barrier thicknesses with 2.5 Å of Mg and 12 Å or 14 Å of Al, the green and red curves, respectively, in figure 6.13 left. The most probable reason is that the thin Mg seed layer does not cover completely the Heusler surface leaving open regions were oxidation could penetrate through the barrier and oxidize the $Co_2FeAl_{0.3}Si_{0.7}$ surface. The Al does not cover this open areas because it is most likely to wet only on the Mg deposited regions. As a consequence, and assuming that the oxidized Heusler surface form some kind of insulating tunneling barrier, spin scattering increases and the resistance gets stronger influenced by increasing temperature. Such an explanation would fit with the measured TMR values, which are the smallest measured, 14 % and 17 %, respectively. In figure 6.13, right, the TMR measurements of these junctions are shown together with other junctions with different barrier thicknesses. As can be observed, these two junctions present high resistances due to the oxidation of the $Co_2FeAl_{0.3}Si_{0.7}$ surface. The other junctions with thicker barrier have smaller slopes and lower resistances. Although their behaviour is in agreement with Rowell's criteria, a high quality of the barrier may not be concluded. Pinholes affect the resistance curve in the same way as already mentioned and underoxidation also reduces resistance. Underoxidation can be identified from the temperature dependence of the resistance curves by typically a non-linear behaviour occuring at low temperatures, like it is the case for the junction with 10 Å of Mg and 14 Å of Al (blue curve in figure 6.13). However, this non-linear behaviour can be also due to other factors like redeposited metallic material due to the ion etching in the lithography process or insufficient etching depth. Therefore, in the cases in which the linear behaviour is similar, as well as the resistance values, only TMR measurements and tunneling spectroscopy would give an indication of how good the barrier properties are. All results shown in figures 6.12 and 6.13 are obtained by using the same oxidation cathode and the same oxidation time, which was 30 seconds. The maximum TMR values obtained with these oxidation conditions are 45 %, for a junction with 7.5 Å of Mg and 14 Å of Al barrier thickness and annealed at 450°C (blue curves in figure 6.12), and 30 %, for a junction with 7.5 Å of Mg and 18 Å of Al barrier thickness and annealed at 550°C (pink curves in figure 6.13). In both TMR measurements, as shown in figure 6.12 and 6.13, right, the center of the magnetoresistance loop is shifted from zero external magnetic field and differs from one junction to the other. The reason for this is that the external magnetic field applied parallel to the junction surface is originated by

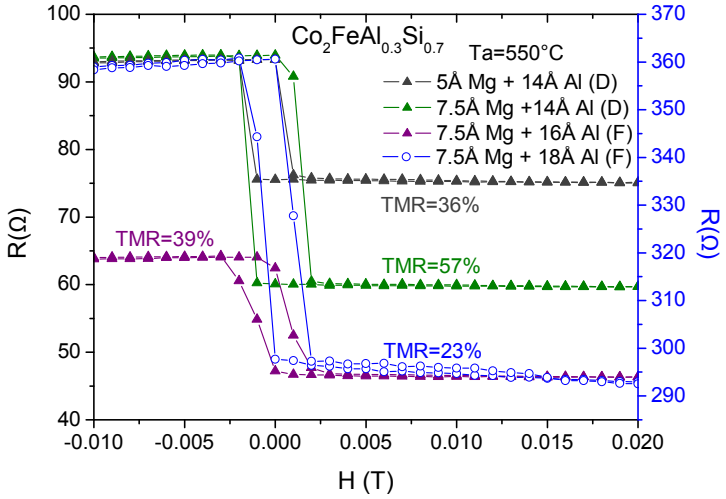


**Figure 6.14:** *TMR of $Co_2FeAl_{0.3}Si_{0.7}$ based MTJ's with different barrier thicknesses and different mesa areas: D ($160 \times 80 \mu m^2$) and F ($60 \times 60 \mu m^2$). Oxidation conditions were improved. The annealing temperature of the $Co_2FeAl_{0.3}Si_{0.7}$ base electrode amonts to 550 °C*

a superconducting magnet and sometimes the presence of trapped flux in the superconducting magnet can not be avoided.

Due to unstable conditions during oxidation process which made reproducibility difficult, another oxidation cathode was built and placed in another chamber. The oxidation conditions were improved and stabilized by adjusting also oxidation time (15 s) and distance to the sample. After that, the resistance of $Co_2FeAl_{0.3}Si_{0.7}$ junctions changed drastically from kΩ range to Ω range and TMR values were improved (see figure 6.14). The lowest TMR value corresponds to the highest resistance value of a junction with the highest barrier thickness: 7.5 Å of Mg and 18 Å of Al (blue open dots in figure 6.14). Due to the fact that the oxidation time for this junctions was kept constant (15 s), overoxidation would not be an explanation, unless for this sample barrier deposition condition changed accidentally, or worst Heusler surface quality was achieved. Underoxidation would be the possible reason for the behaviour of this junction.

The highest TMR value achieved for $Co_2FeAl_{0.3}Si_{0.7}$ was 57 % at 2 K. Applying Jullière model, this correspond to a spin polarization of 44 % for $Co_2FeAl_{0.3}Si_{0.7}$ when 50 % spin polarization for CoFe is considered [192]. No other published re-

sults on experimental spin polarization values for $Co_2FeAl_{0.3}Si_{0.7}$ have been found.

For $Co_2MnGa$ the oxidation process was made with the new oxidation cathode. Here the oxidation time was also varied as well as barrier thickness in order to enhance TMR values. Results are shown in figure 6.15. The temperature dependence of the tunnel resistance normalized to the lowest temperature for different barrier thicknesses and oxidation times is shown in the left graph of figure 6.15. This analysis was done for junctions with $Co_2MnGa$ annealed at 550 °C. A weak linear decrease of the resistance with increasing temperature is also observed here. The different barriers result in different decreasing behaviours of the resistance curves (a reduction which varies between 10 % and 30 %). From the junctions for which the temperature dependence of the resistance was measured the curve with the largest decrease (30 %) correspond to the junction with the highest TMR value (black curve in figure 6.15, left and right). However, it shows a very high resistance value which could be due to an overoxidation, due to a longer oxidation time compared to the others (barrier parameters: 5 Å of Mg + 14 Å of Al + 15s Ox). Another junction prepared with the same barrier parameters shows a smaller decrease of the resistance (20 %) but a smaller TMR value (11 %) (light blue curve in figure 6.15 left), although the resistance values were in the same order for both junctions (around 4 kΩ). All junctions with a small decrease of the resistance did not show TMR values higher than 14 %. Taking into account that the highest measured TMR value for $Co_2MnGa$ was only 24 % for a barrier thickness of 5 Å of Mg + 10 Å of Al + 12s Ox with a resistance of 580 Ω (see blue open dots in right graph of figure 6.15), it can be assumed that for the other junctions, the used barrier parameters, result in underoxidation because of their smaller resistance range 100-300 Ω. However, no optimal parameters which enhanced TMR values for $Co_2MnGa$ were achieved.

Comparing $Co_2MnGa$ with $Co_2FeAl_{0.3}Si_{0.7}$, it can be observed that even by using the same barrier parameters, the results are rather different. While for $Co_2FeAl_{0.3}Si_{0.7}$ a TMR value of 57 % was achieved, for $Co_2MnGa$, however, only 24 % TMR was measured. This could indicate that spin polarizations are different (theory predicts $Co_2MnGa$ not to be a half-metal, but a relatively high spin polarization of 67 % is expected [81]), but the most probable reason here could be that interface properties of both materials are rather different, affecting the tunneling current in a different way. Moreover, although RHEED revealed

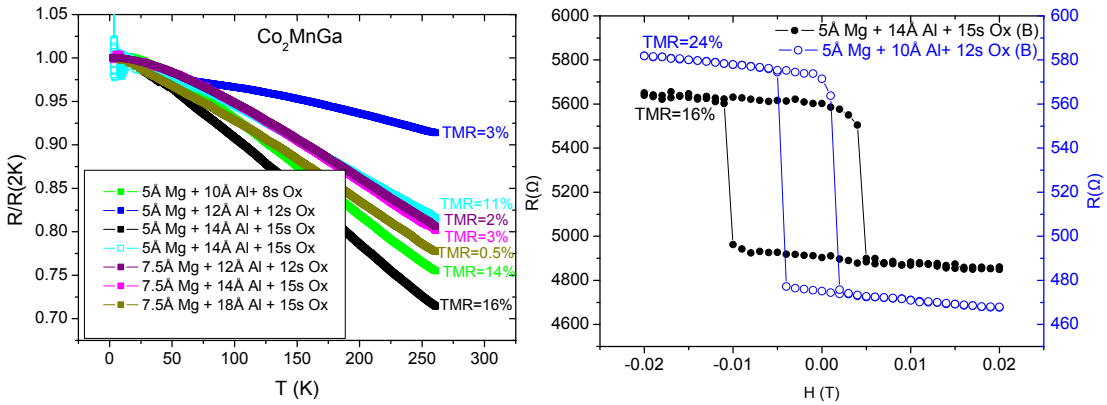


**Figure 6.15:** *Left: Temperature dependence on tunnel resistance normalized by the lowest temperature of $Co_2MnGa$ based MTJ's with different barrier thicknesses in absence of external magnetic field. Right: TMR of $Co_2MnGa$ based MTJ's with different barrier thicknesses Heusler compound and B mesa area ($100 \times 100\ \mu m^2$). The annealing temperature of the $Co_2MnGa$ base electrode amounts to 550 °C.*

good crystallographic order at the surface, the surface magnetic properties of $Co_2MnGa$ were not analysed, and therefore, changes with respect to bulk could be another reason here. On the other side, the best TMR values in both cases correspond to small resistance values, what reveals the importance of achieving a thin and homogeneous insulating barrier for reliable TMR results.

In conclusion, considerable spin polarization for $Co_2FeAl_{0.3}Si_{0.7}$ was obtained (44 %), although it is clearly lower than the theoretical 100 % predicted. Moreover, no high TMR value for $Co_2MnGa$ was achieved. As can be observed, the complexity of enhancing TMR values does not only include varying barrier parameters and finding best insulating barrier properties which allow optimal tunneling conditions. However, reproducibility is not always possible. Reproducibility problems could be due not only to other internal problems in the junction which contribute to a reduction of the tunneling conductance and are not described within Jullière model, such as interface effects, impurity levels, surface roughness, which differ from one junction to the other, but also external problems, such as etching problems during lithography, bad contacts, broken mesas, flashing during oxidation (it occured only in the first set of samples), etc. Therefore, spin polarization determination via TMR measurements remains rather challenging.

### 6.4.2 Tunneling Spectroscopy

In order to understand better which effects contribute to the tunneling current, the bias voltage dependence of the differential conductivity was investigated.

As already discussed in the theoretical section, the tunneling current in a MTJ is determined by the folded DOS of both electrodes and the tunneling barrier potential, see equation 6.10. Brinkman's model describes the influence of the barrier potential and its deformation on the tunneling current and obtains the differential conductivity as a parabolic function of the bias voltage, eq. 6.13. Such an approximation is able to explain not only the parabolic shape of dI/dV curve but also the asymmetry on the conductance curve for different signs of the bias voltage due to an asymmetrical barrier potential shape (see figure 6.2).

Under ideal conditions, it is expected that deviations from the Brinkman behaviour correspond to band structure effects. Strong changes of the total electron DOS should give an increase in the conductance. However, the possibility of observing DOS contributions in tunneling spectra still remains under doubt. On the other hand, some work on semimetals looks encouraging [193] and it was concluded that when dealing with ferromagnetic or half-metallic ferromagnetic electrodes, the conductance can be significantly affected by band features [194]. Experimental studies of the effects of the density of states on the bias dependence of the conductivity of magnetic tunneling junctions were carried out indicating that a reasonable variation of DOS of the ferromagnetic electrodes makes a considerable contribution to the bias dependent behaviour of MTJ's [195, 196].

Here our goal is to study and analyse the possibility of finding DOS contributions on the dI/dV curves of the prepared junctions. Particularly the DOS of the following two Heusler compounds is under study: $Co_2FeAl_{0.3}Si_{0.7}$ and $Co_2MnGa$. Heusler/$AlO_x$/Au MTJ's are studied. The density of states at low temperatures of the noble metal Au can be assumed to be constant, and therefore, only the Heusler DOS would contribute to the differential conductivity and could be observed in a non-spin dependent measurement. For a Heusler/$AlO_x$/CoFe structure the differential conductivity is proportional to the density of states of both ferromagnets, of the Heusler and of the CoFe. The conductivity is a spin dependent measurement with differences between the parallel and antiparallel

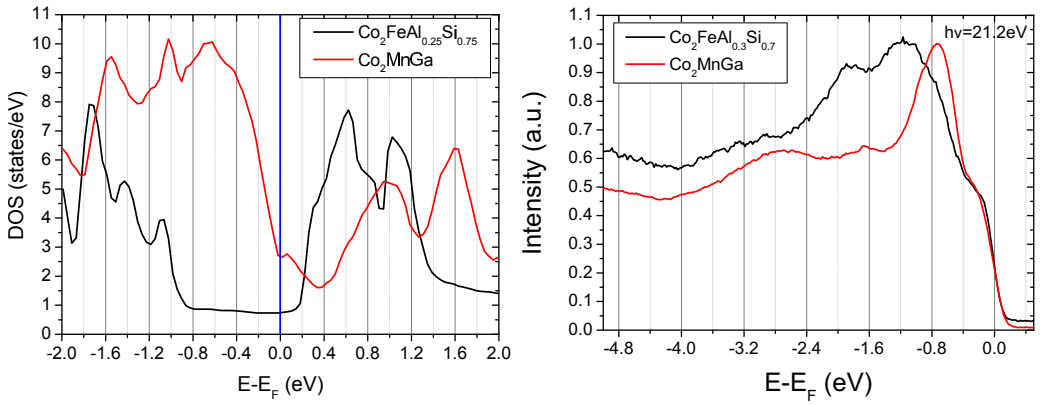


**Figure 6.16:** ***Left:*** *Total density of states of $Co_2FeAl_{0.25}Si_{0.75}$ (black line) and $Co_2MnGa$ (red line) as derived from the digitized graphs calculated by Fecher et al. [85] and Galanakis et al. [81], respectively.* ***Right:*** *UPS comparison between $Co_2FeAl_{0.3}Si_{0.7}$ (black) and $Co_2MnGa$ (red) obtained with a 21.2 eV photon energy.*

configuration. In both cases, barrier contributions become stronger with high bias voltages, thus strong DOS contribution can only be observed at small bias voltages (below 1 eV), i.e. only the states close to the Fermi energy can be investigated.

The theoretical total bulk densities of states for $Co_2FeAl_{0.3}Si_{0.7}$ and $Co_2MnGa$ with the $L2_1$ structure as derived from digitized spin resolved graphs [85, 81], are plotted in figure 6.16 left, black and red curves, respectively. The total DOS close to the Fermi energy differs from one Heusler compound to the other. As can be observed, for $Co_2MnGa$ (red curve) a strong increase of the total DOS occurs at the Fermi energy and the first well defined DOS peak has its maximum at E=-0.7 eV with respect to the Fermi energy. For $Co_2FeAl_{0.3}Si_{0.7}$ however, an increase of the total DOS is observed at E=-1 eV with respect to $E_F$ and the first well defined DOS peak has its maximum at E=-1.1 eV. According to theoretical predictions, the possibility to observe DOS contributions in conductance measurements is more probable for $Co_2MnGa$. DOS features for $Co_2FeAl_{0.3}Si_{0.7}$ would be smeared by the contribution of barrier deformation to the conductance.

Nevertheless, UPS measurements on $Co_2FeAl_{0.3}Si_{0.7}$ thin films reveal something different (black curve in figure 6.16 right). For $Co_2FeAl_{0.3}Si_{0.7}$ a sudden increase of the intensity at the Fermi edge is also observed, as well as for $Co_2MnGa$

(red curve figure 6.16 right). This behaviour was already discussed in chapter 5. Different reasons could explain such a result. One reason is the possibility of measuring surface states, which are not predicted by the theoretical calculations. The contribution of surface states can induce new DOS features and the half metallic properties could even be lost [197]. Second, some degree of disorder in the surface region can contribute to changed DOS features close to $E_F$. Another possibility is that the theoretical calculations fail to take into account strong correlation effects which typically result in a smearing of the DOS features, which would explain the broadening of the intensity peaks at the UPS spectra compared to the narrow and well defined peaks present in band structure calculations. Therefore, a comparison from experimental tunnelling conductivity data with theoretical calculations is not straightforward.

In figure 6.17, the bias voltage dependence of the differential conductivity for a $Co_2FeAl_{0.3}Si_{0.7}/AlO_x/Au$ (black curve) and a $Co_2MnGa/AlO_x/Au$ (red curve) junction measured at T=2 K are plotted. Differences are observed between both compounds. While for $Co_2FeAl_{0.3}Si_{0.7}$ a weak asymmetry between the positive and the negative bias voltage is observed, a very strong one is present on $Co_2MnGa$. The strong asymmetry for $Co_2MnGa$ is produced by the pronounced linear behaviour of the conductance for positive bias voltages, which is not present for $Co_2FeAl_{0.3}Si_{0.7}$. Asymmetry is a common feature for dissimilar electrodes and it is included in Brinkman's model. Near zero bias the shape of the conductance curve is sharp for both compounds (for a better observation see figure 6.18 left for $Co_2MnGa$ and right for $Co_2FeAl_{0.3}Si_{0.7}$). This feature is called the zero bias anomaly and is commonly observed for all junctions with ferromagnetic or transition metal electrodes [198]. Different explanations have been given for its origin: the presence of metal particles in the barrier, magnons, magnetic impurities, localization effects, multi-step tunneling or states in the barrier or at the interface, which would consequently affect the spin polarization of the tunneling electrons by causing spin-flip scattering [167]. Therefore, a combination of these inelastic processes, not included on the theoretical models, influences also the bias voltage dependent conductance.

In order to show how the DOS of the electrodes and the use of different materials for the upper electrode contribute to the junction conductance, the bias voltage dependent conductance for junctions with different upper electrodes, ei-

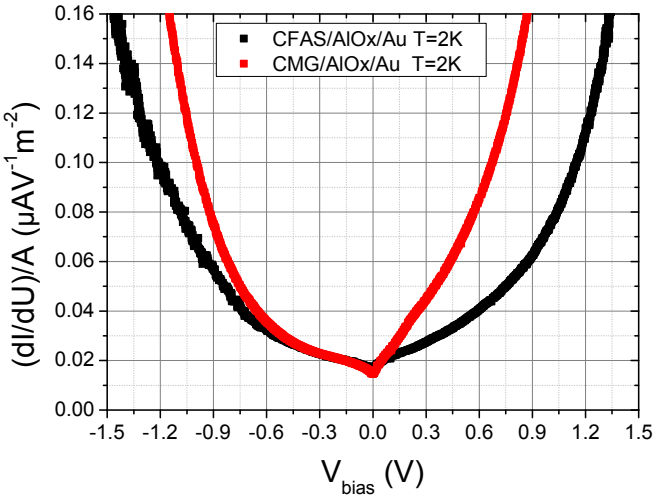


**Figure 6.17:** *Comparison of the differential conductivity $dI/dV(V_{bias})$ of $Co_2FeAl_{0.3}Si_{0.7}$ (black) and $Co_2MnGa$ (red) magnetic tunneling junctions.*

ther Au (top graphs in figure 6.18) or CoFe (bottom graphs in figure 6.18), are shown in figure 6.18, left, for $Co_2MnGa$ and right for $Co_2FeAl_{0.3}Si_{0.7}$. When using CoFe as an upper electrode, tunneling is a spin-dependent process, thus two dI/dV-V curves are measured, one for the parallel configuration (black curves in bottom graphs of figure 6.18) and the other for antiparallel (red curves in bottom graphs of figure 6.18). The difference between them gives the bias voltage dependence on TMR. These curves show clear differences of the parabolic shape and conductance values when compared to the curves obtained with Au as an upper electrode. This is an indication that the conductance is influenced by the properties of the upper electrode, not only due to different interfaces but also due to DOS contributions. Therefore, in order to be able to detect only DOS contributions from the Heusler compound, an upper electrode with no DOS variation should be used. Hence, Au as noble metal is chosen, whose DOS is assumed to be constant. The strong linear behaviour of dI/dV with respect to the bias voltage for the $Co_2MnGa/AlO_x/CoFe$ junctions, resulting in a more V-like than parabolic behaviour, will be discussed later.

The conductance as a function of temperature for a $Co_2MnGa/AlO_x/Au$ junction is shown in figure 6.19. The differential conductivity at different temperatures was measured within a small bias voltage range (-140 mV - 140 mV). The linear behaviour and the strong asymmetry that characterizes the curve at T=2 K

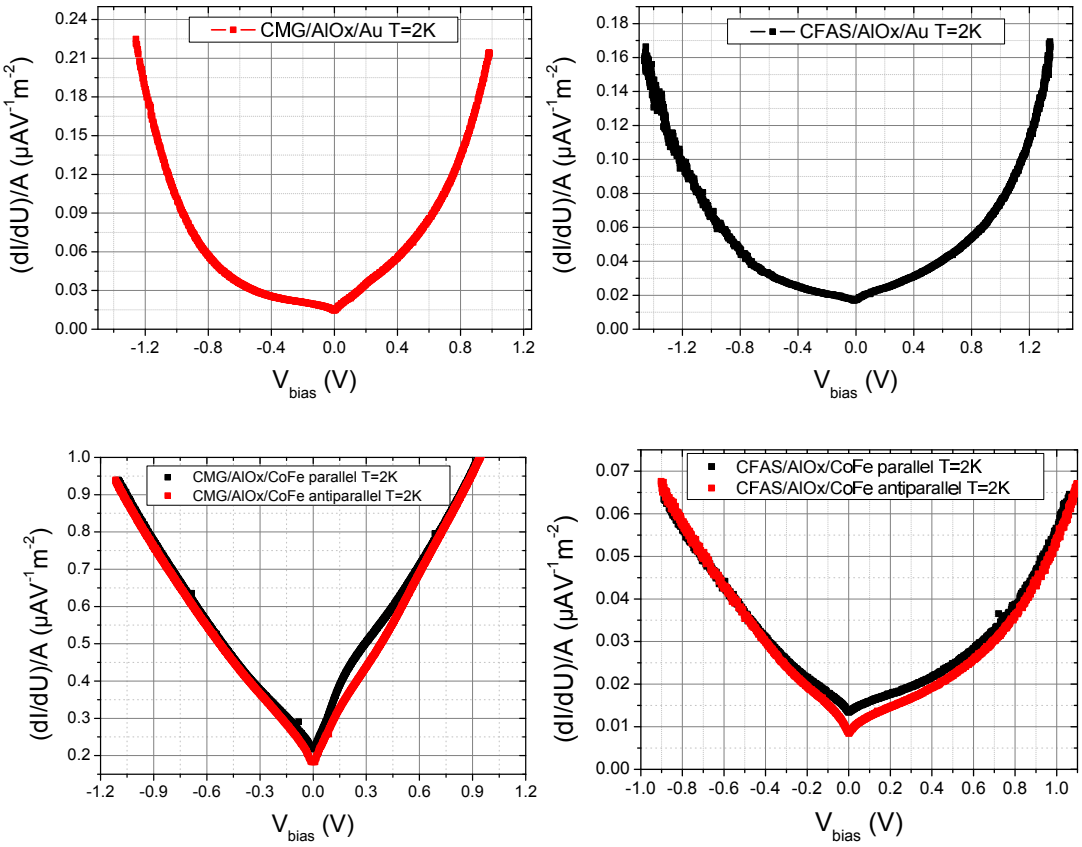


**Figure 6.18:** ***Top:****Comparison of differential conductivity* $dI/dV(V_{bias})$ *of* $Co_2FeAl_{0.3}Si_{0.7}$ *(top right figure) and* $Co_2MnGa$ *(top left figure) based magnetic tunneling junctions with Au as upper electrode.* ***Bottom:*** *Comparison of differential conductivity* $dI/dV(V_{bias})$ *of* $Co_2FeAl_{0.3}Si_{0.7}$ *(bottom right figure) and* $Co_2MnGa$ *(bottom left figure) based magnetic tunneling junctions with CoFe as upper electrode.*

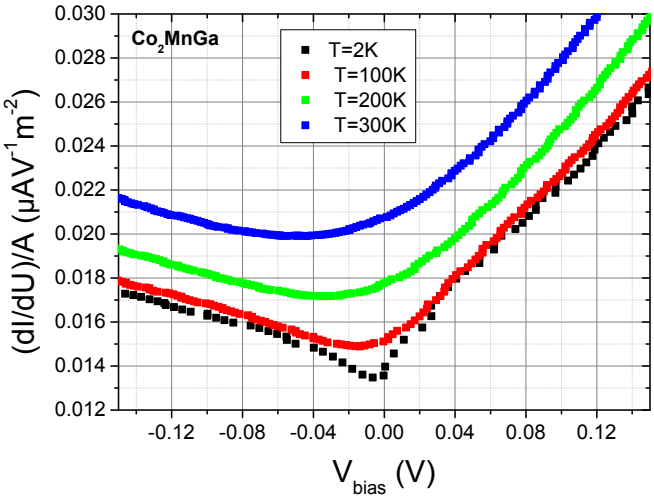


**Figure 6.19:** *Comparison of the differential conductivity $dI/dV(V_{bias})$ of $Co_2MnGa$ based magnetic tunneling junctions with Au as an upper electrode at different temperatures.*

remains with increasing temperature. However, as the temperature raises, an increase of the conductance with bias voltage occurs. The reason for this behaviour was already explained. The conductance is the sum of a polarization dependent direct elastic tunneling part and of a non-polarization dependent part, due to imperfections which provide a noticeable hopping conductance through the associated localized states [190]. This two terms behave differently with temperature and contribute to an increase of the conductance and a decrease of the TMR with temperature.

For the study of the contribution of the barrier potential to the conductance curve for $Co_2MnGa/AlO_x/Au$ junctions, Brinkman's model (eq. 6.13) is applied. After many tries to fit the experimental curve obtained within this model the best fitting possible was achieved and is shown in figure 6.20. The barrier parameters obtained within this fit correspond to a barrier height of $\bar{\varphi}$=2.03 eV, an asymmetry of $\Delta\varphi$=1.25 eV and thickness of d=12.8 eV.

As can be observed, the strong asymmetry of $Co_2MnGa$ can not be simply described by Brinkman's model. While for positive bias voltage a strong linear behaviour of dI/dV with V is seen, a slow and parabolic increase of dI/dV for negative V characterizes the curve. There are other effects appart from the

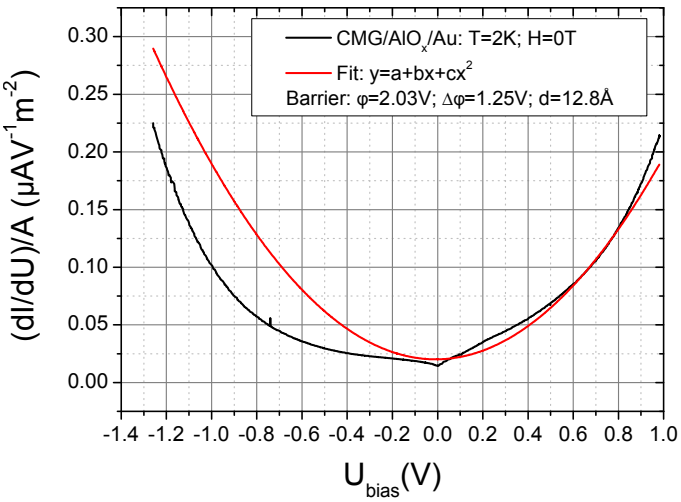


**Figure 6.20:** *Brinkman's model fit of the experimental differential conductivity $dI/dV(V_{bias})$ of a $Co_2MnGa$ magnetic tunneling junctions with Au as upper electrode.*

barrier potential deformation described by Brinkman, which contribute to the asymmetry, like DOS features and inelastic processes. Another possibility could be the presence of a more complicated barrier potential shape, due to a more pronounced difference between the lower and upper interface of the insulating barrier than that described in Brinkman's model.

### 6.4.3 Comparison between Experiment and Numerical Calculations

In order to answer these questions, the decision of calculating numerically the differential conductivity as a function of the bias voltage going beyond the approximation of the Brinkman's model was made. The equations 6.11 and 6.10 were solved numerically by introducing to the tunneling probability, the contribution of different barrier potentials as functions of the bias voltage. The differential conductivity was calculated using the program *"Wolfram Mathematica 8.0"* and it is shown in appendix C.

First, the influence of the potential barrier on the asymmetry of the conductance curve was studied. For that, different barrier potential shapes were defined and the DOS contribution was assumed constant. In order to be able to detect

which type of barrier produces the strongest asymmetry, the parameters were chosen in a way that the integral potential barrier area was the same for the different barrier shapes. The conductance curves obtained numerically are plotted in figure 6.21 together with the conductance curve obtained by applying Simmons' model (eq. 6.12). The barrier parameters taken for the Simmon barrier are height h=2 eV and thickness d=15 Å. When comparing the bias voltage dependence of the differential conductivity applying Simmons' model (green coloured curve in 6.21) with the numerical calculation assuming a Simmons' barrier shape (black coloured curve in 6.21) no difference on the asymmetry is observed, both curves are symmetric and their minimum are located at 0 V. However, the curvatures differ, Simmons' model results in a more open curvature than the numerical calculation. When the barrier shape changes and Simmons' potential barrier with one height and one thickness is replaced by two Simmons' potential barriers (red coloured curve in 6.21) with two heights, $h_1$=2.5 eV and $h_2$=1.5 eV, and two equal thickness, $d_1$=7.5 Å and $d_2$=7.5 Å, an asymmetry appears and the minimum is shifted from zero bias voltage to a negative value. The increase of dI/dV with positive bias voltages is larger than for negative values. If this barrier is compared with a Brinkman's potential barrier with the same parameters (blue coloured curve in 6.21), it is observed that, although for a Brinkman's barrier the minimum in dI/dV is also shifted to the same position, the asymmetry is not as strong as obtained for two Simmons barrier. This analysis indicates that considering more complex potential barrier shapes results on a stronger asymmetry of the differential conductivity curve.

Therefore, by modelling different possible barrier shapes, a better fitting of the experimental results can be achieved, and more accurate barrier parameters values are obtained. These fits were applied to $Co_2MnGa/AlO_x/Au$ and $Co_2FeAl_{0.3}Si_{0.7}/AlO_x/Au$ junctions, in order to evaluate if a more complex barrier shape would be able to explain the conductance curves obtained for these junctions. The results are shown in figure 6.22, left top graph for a $Co_2MnGa/AlO_x/Au$ junction and right top graph for a $Co_2FeAl_{0.3}Si_{0.7}/AlO_x/Au$ junction. The barrier considered is formed by two Brinkman's barrier with different height and thickness, shown at the bottom left in figure 6.22. For the $Co_2MnGa/AlO_x/Au$ junction, the barrier parameters found to be the best fit for the conductance curve are: $h_1$=3 eV; $h_2$=2 eV and $d_1$=12 Å fo the first barrier, and for the second $h_3$=2 eV, $h_4$=1 and $d_2$=3 Å. For the $Co_2FeAl_{0.3}Si_{0.7}/AlO_x/Au$ junction, the barrier

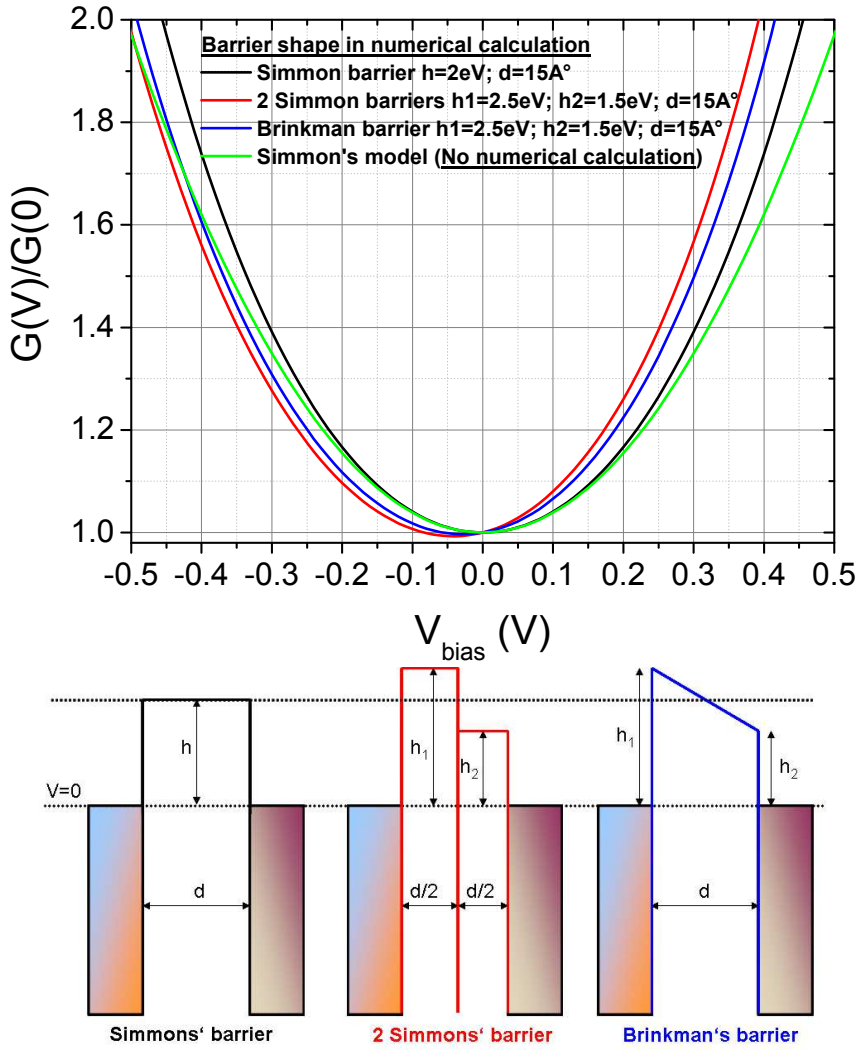


**Figure 6.21:** ***Top:*** *Numerically calculated differential conductivity $dI/dV(V_{bias})$ curves for different barrier potential together with the differential conductivity $dI/dV(V_{bias})$ curve obtained by Simmons' model (green curve).* ***Bottom:*** *Different barrier shapes used for the numerical calculation. The colour of the barrier shape indicates its corresponding differential conductivity in the top graph.*

parameters found to be the best fit for the conductance curve are: $h_1$=2.5 eV; $h_2$=2 eV and d=11 Å (only one barrier was considered for this case and is shown at the bottom right in figure 6.22).

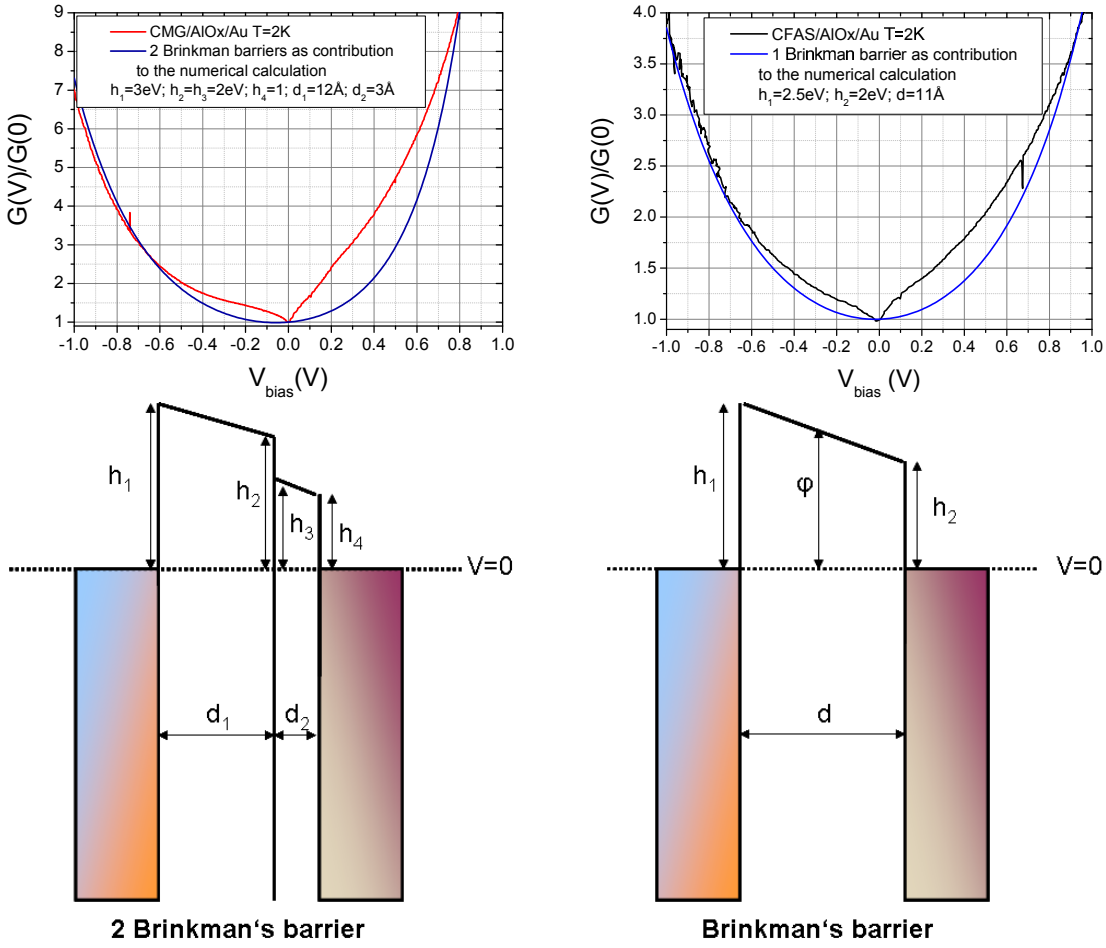


**Figure 6.22:** ***Top:*** *Fit of the experimental differential conductivity $dI/dV(V_{bias})$ of $Co_2MnGa$ (left) and $Co_2FeAl_{0.3}Si_{0.7}$ (right) magnetic tunneling junctions with Au as upper electrode by numerical calculation assuming Brinkman's potential barrier shapes. Bottom: The two different barrier shapes used to fit the experimental conductance curves by numerical calculation, left for $Co_2MnGa$ and right for $Co_2FeAl_{0.3}Si_{0.7}$. Height (h) and thickness (d) were the variable parameters.*

Although some broadening and asymmetry of the experimental curve were reproduced by fitting the barrier potential, there are still contributions to the differential conductivity that the barrier potential is not able to describe. One example is the slow increase of dI/dV with negative bias voltage just near zero

bias for both junctions. For positive bias voltage the linear behaviour of dI/dV for the $Co_2MnGa/AlO_x/Au$ junction can not be described just by a barrier potential contribution. For the $Co_2FeAl_{0.3}Si_{0.7}/AlO_x/Au$ junction the same occurs, although for positive bias voltage dI/dV has a parabolic behaviour.

Other effects which could contribute to the conductance of these two junctions are: DOS features of the Heusler compound close to the Fermi energy, interface states, inelastic processes due to impurities or defects, etc.

The design of this MTJ's, with only the Heusler compound as a ferromagnetic electrode while the other is a noble metal, make the analysis of these contributions more simple. In these junctions magnon excitations can only occur when electrons are tunneling into the ferromagnet. Their contribution can only be observed for one sign of bias voltage. The electrical connections of the junctions were done in a way that a positive bias voltage corresponds to electrons travelling into the Heusler, while for a negative bias voltage the electrons tunnel out of the Heusler. In figure 6.22, the stronger increase of the conductance with bias voltage occurs for positive bias voltages in both Heusler junctions. However, the junction with $Co_2MnGa$ (6.22, left) shows a stronger increase of the conductance which is almost linear compared with the junction with $Co_2FeAl_{0.3}Si_{0.7}$ electrode (6.22, right). This is an indication that the density of excited magnons in $Co_2MnGa$ is higher than in $Co_2FeAl_{0.3}Si_{0.7}$. A possible reason could be the different composition of the compounds. Ga is a heavier element with d-states than Al or Si with no d-states. Thus, $Co_2MnGa$ has a stronger spin orbit coupling contribution than $Co_2FeAl_{0.3}Si_{0.7}$. This, together with the fact that the Fermi energy of this compound is in the proximity of the minority valence band edge [81] (see left graph in figure 6.16), reduces its spin polarization making spin-flip processes, and consequently magnon excitations, more likely to occur in $Co_2MnGa$ than in $Co_2FeAl_{0.3}Si_{0.7}$ [90, 197].

The stronger increase of conductance for positive compared to negative bias can be explained as follows: Assuming that the Heusler compound is 100 % spin polarised, ideally, the electrons which tunnel from the Au into the Heusler have two possibilities: they will tunnel into the Heusler for the same spin and get reflected for the opposite spin. Taking into account the description of Appelbaum and Brinkman [175], magnons can effect this type of junctions in two ways:

(1) The electron tunnels elastically through the $AlO_x$ into the electron states of the Heusler compound, which are renormalized by the electron-magnon interaction in the bulk of the material.
(2) The electron tunnels through the $AlO_x$ into the Heusler and due to magnetic impurities at the interface it flips its spin. The localized spins are coupled to the bulk magnetization of the ferromagnetic material and therefore the magnon DOS will contribute to the tunneling process in the Heusler compound and the spin-flip of electrons which tunnel with opposite spin compared to that of the ferromagnet increase the tunneling conductivity.

This process can not take place for negative bias voltage with the electrons tunneling out of the Heusler and into the noble metal. Thus, the features experimentally observed in the dI/dV curve for this region should be due to characteristic DOS features of the Heusler compound or interface states as already observed by UPS. However, for the case of MTJ's with CoFe as upper electrode, magnon excitations can also take place due to magnetic impurities also in the interface between CoFe and the insulating barrier, thus electrons tunneling into CoFe (negative bias voltage) also can flip their spin and magnons are excited into the bulk ferromagnet. Such an explanation explains the V-like shape of the conductance curve for $Co_2MnGa/AlO_x/CoFe$ junctions (bottom left figure 6.18). For $Co_2FeAl_{0.3}Si_{0.7}/AlO_x/CoFe$ junctions a different behaviour for electrons tunneling into $Co_2FeAl_{0.3}Si_{0.7}$ (positive bias voltage) or into CoFe (negative bias voltage) is observed (bottom right figure 6.18). For negative bias voltage the conductance behaviour is more linear than for positive bias voltage as an indication of a higher density of magnon excitations in the CoFe than in the $Co_2FeAl_{0.3}Si_{0.7}$.

DOS contribution was introduced into the tunneling current numerical calculation by assuming the DOS function as sums of two Gaussian functions close to the Fermi energy.

$$N(E) = 1 + a_1 exp\left[-\left(\frac{E - ep_1}{2e_1}\right)^2\right] + a_2 exp\left[-\left(\frac{E - ep_2}{2e_2}\right)^2\right] \qquad (6.20)$$

where the variable parameters to adjust are the heights $a_1$ and $a_2$, centers $ep_1$ and $ep_2$, and width $e_1$ and $e_2$.

The fit of dI/dV-V with the obtained parameter values for the barrier and the

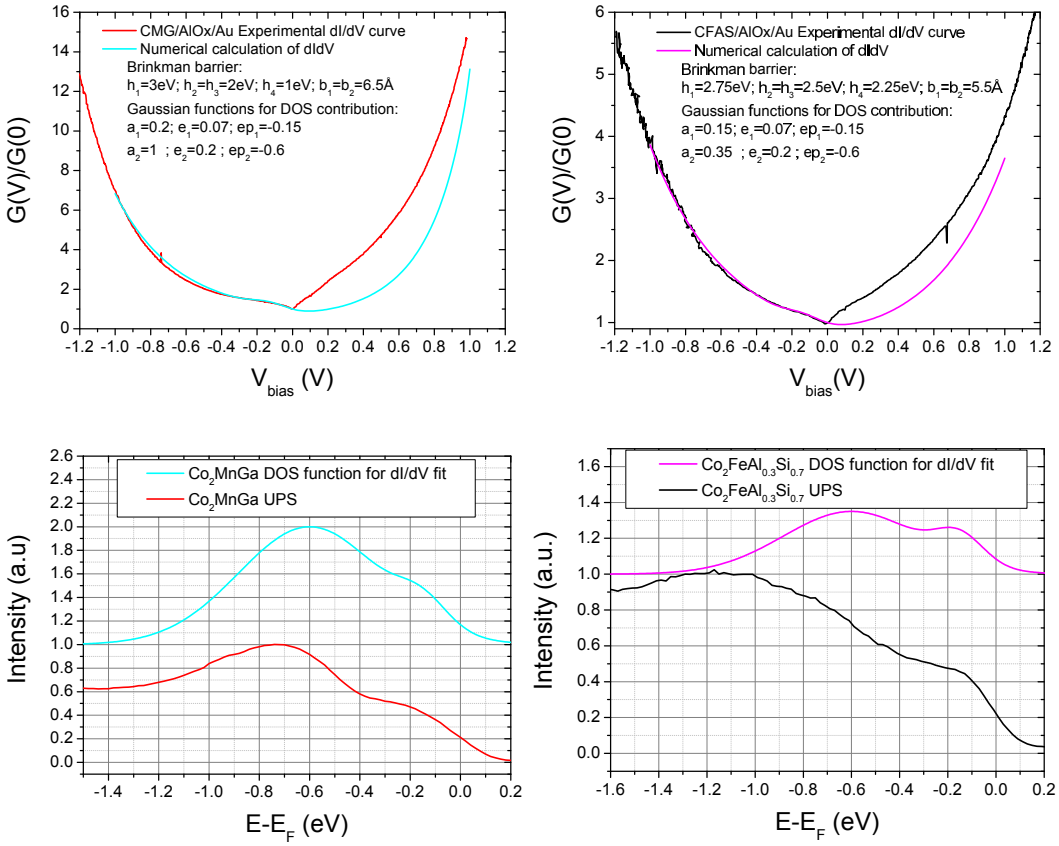


**Figure 6.23:** ***Top:*** *Fit of the experimental differential conductivity $dI/dV(V_{bias})$ of $Co_2MnGa$(left) and $Co_2FeAl_{0.3}Si_{0.7}$ (right) magnetic tunneling junctions with Au as upper electrode by numerical calculation assuming Brinkman's potential barrier shape and contribution of the Heusler DOS as Gaussian functions.* ***Bottom:*** *Comparison between DOS function used on the numerical calculation for fitting the dI/dV curve and the results obtained with UPS measurements for $Co_2MnGa$ left and $Co_2FeAl_{0.3}Si_{0.7}$ right.*

DOS contribution are shown in figure 6.23, top left graph for $Co_2MnGa$ and top right graph for $Co_2FeAl_{0.3}Si_{0.7}$. As can be observed, the dI/dV behaviour with bias voltage could be perfectly fitted for negative bias voltage, in both cases. The parameters of the barrier and the DOS functions are given in the graph of each junction, top left and right in figure 6.23. At the bottom, the two DOS functions used for the fitting in the numerical calculation are shown for the $Co_2MnGa$ junction, left, and for the $Co_2FeAl_{0.3}Si_{0.7}$ junction, right, together with the obtained UPS measurement for comparison.

The first Gaussian function has its center at E=-0.15 eV for both compounds. At this energy no theoretical DOS feature is predicted. However UPS measurement show a small bump at around E=-0.2 eV for both compounds as well. These features, observed with both experimental methods, can be due to non-predicted interface states as it was also discussed for the UPS results. The second Gaussian has its center at E=-0.6 eV for both compounds. Such a contribution fits also with UPS measurement and the theoretical prediction for $Co_2MnGa$. In fact, qualitatively the DOS function used for the fitting of the dI/dV curve matches perfectly with the intensity features observed by UPS for the same compound. Therefore the observation of DOS of the Heusler compound $Co_2MnGa$ at E=-0.6 eV is justified. For $Co_2FeAl_{0.3}Si_{0.7}$, however, the DOS function differs from the UPS results and theoretical predictions concerning the second maximum, which is located at E=-1 eV. Such a mismatch, could be due to the fact that this DOS peak can not be observed by tunneling spectroscopy due to the stronger contribution of the barrier shape and its deformation at higher bias voltages, which smears out DOS features. Therefore, only DOS contributions close to the Fermi energy are observable by tunneling spectroscopy.

The presence of localized interface states has been already discussed by Mavropoulos et al. [197]. They explain how the current in a tunneling process depends only on the tunneling rates of the two spin directions. These tunneling rates depend on numerous factors like insulating barrier, band structure, interface structure, presence of interface disorder, symmetry at the interface, defects, etc. The TMR ratio is always limited by interface states contribution and therefore no high TMR value can be expected unless no interface states are present at all. Due to the difficulty of calculating interface states between a ferromagnet and an insulating amorphous barrier like $AlO_x$, no theoretical information about how

they would effect quantitatively the tunneling current is found. However, calculations of Heusler alloy/semiconductor interfaces [200, 201, 202] reveal how interface states at the Fermi energy result in a loss of half metallicity.

In conclusion, tunneling spectroscopy of $Co_2MnGa/AlO_x/Au$ and $Co_2FeAl_{0.3}Si_{0.7}/AlO_x/Au$ MTJ's was carried out. The results are in agreement with UPS experiments. Both methods are able to demonstrate the validity of band structure calculations for $Co_2MnGa$ Heusler compound. Additionally, interface states close to the Fermi energy are observed experimentally by both methods. Due to the bias voltage limitations for the observation of DOS contributions, tunneling spectroscopy does not allow the observation of DOS features at energies higher than 1 eV, therefore only interface states were observed for the $Co_2FeAl_{0.3}Si_{0.7}$ Heusler compound. Moreover magnetic impurities at the interface between ferromagnet and insulating barrier originate spin flip processes and consequently magnon excitations in the bulk ferromagnet. Thus, more electrons are allowed to tunnel into the ferromagnet and therefore a stronger increase of the tunnel conductance for positive than for negative bias voltage is observed. Due to a stronger spin-orbit coupling in $Co_2MnGa$, the density of spin flip processes is higher than for $Co_2FeAl_{0.3}Si_{0.7}$. Therefore $Co_2MnGa$ presents a more V-like conductance curve than $Co_2FeAl_{0.3}Si_{0.7}$, whose conductance curve is more parabolic-like. The presence of interface states and magnetic impurities can be the reason why it was not possible to obtain a high TMR value and therefore to demonstrate half-metallicity for $Co_2FeAl_{0.3}Si_{0.7}$ and a high spin polarization for $Co_2MnGa$.

# Chapter 7

# Summary

According to band structure calculations, many Heusler compounds are predicted to be potential candidates for showing half metallic properties with a high Curie temperature clearly above room temperature and a relative large band gap at the Fermi energy.

In this work an experimental evaluation of the validity of predictions of half metallicity by band structure calculations for two specific Heusler compounds, $Co_2FeAl_{0.3}Si_{0.7}$ and $Co_2MnGa$, was carried out. For the experimental analysis of the electronic properties two different spectroscopy methods were used: Angular Resolved Ultraviolet Photoemission Spectroscopy (ARUPS) and Tunneling Spectroscopy.

In order to understand the basis of band structure calculations and their limitations, a theoretical introduction to Density Functional Theory and its approximations was given. In particular, theoretical predictions for the electronic and magnetic properties of $Co_2FeAl_{0.3}Si_{0.7}$ and $Co_2MnGa$ are based on LDA+U with the FLAPW (Full-potential LAPW) and on LDA with the FSKKR (Full-potential Screened KKR) approximations, respectively. These approximations are suitable for describing electronic systems with d-electrons like it is the case here. However, they fail on describing strong correlations between electrons, for which LDA+DMFT has demonstrated to be a powerful technique.

Additionally, a review of different properties predicted to reduced the spin polarization of these Heusler compounds, like spin-orbit coupling, temperature,

disorder and defects was presented.

For the experimental analysis, $Co_2FeAl_{0.3}Si_{0.7}$ and $Co_2MnGa$ were grown as thin films. In order to achieve a high quality of the material and, particularly the surface, an optimized preparation method was developed and the bulk and surface properties of the films were analysed. X-ray diffraction analysis revealed that epitaxial growth and high bulk quality of the thin films were achieved. Increasing annealing temperature improves the crystallographic order. With increasing annealing temperature, a crossover from B2 to $L2_1$ was observed for $Co_2FeAl_{0.3}Si_{0.7}$. This crossover of the crystallographic order takes also place in the surface as observed by RHEED. XMCD analysis indicated that the magnetic properties in the surface and bulk are the identical for $Co_2FeAl_{0.3}Si_{0.7}$. Moreover, the magnetic moment remained constant with improving crystallographic order. Experimental values differed from theory in $Co_2FeAl_{0.3}Si_{0.7}$ thin films while for $Co_2MnGa$ thin films the experimental results were in good agreement with theoretical predictions.

ARUPS is an experimental surface sensitivity technique which provided us information about the electronic DOS close to the Fermi energy of $Co_2FeAl_{0.3}Si_{0.7}$ and $Co_2MnGa$ Heusler compounds. Within this technique evidence for the validity of the predicted total bulk DOS was demonstrated for both Heusler compounds. Close to the Fermi energy, the energy position of the ARUPS emission maxima were in agreement with theoretically predicted energy ranges of high DOS. Additional ARUPS intensity contributions and a shoulder-like feature close to the Fermi energy did not correspond to any calculated total bulk DOS. They were concluded to be due to surface states. In addition, it has been demonstrated that crystallographic order plays an important role on broadening effects. The properties could be modified and controlled by sample annealing. Improving order resulted on better defined ARUPS features.

With performing MTJ's based on $Co_2FeAl_{0.3}Si_{0.7}$ or $Co_2MnGa$ Heusler compounds, tunneling magneto resistance (TMR) measurements and tunneling spectroscopy were carried out. A considerable 44 % spin polarization for $Co_2FeAl_{0.3}Si_{0.7}$ was obtained although it is lower than theoretically predicted. This value fits with the values obtained from first spin resolved ultraviolet photoemission spectroscopy (SRUPS) measurements on this compound. However for $Co_2MnGa$ no

high TMR was achieved although with SRUPS a spin polarization of 60 % was obtained. Taking into account the many aspects that affect TMR enhancement in a MTJ device, such as barrier quality, interface effects, impurity levels, surface roughness and reproducibility, the determination of spin polarization remains rather challenging.

Additionally, tunneling spectroscopy results are in agreement with the ARUPS experiments. Both methods are able to demonstrate the validity of band structure calculations for the Heusler compound $Co_2MnGa$. However, tunneling spectroscopy for DOS detection is limited to small bias voltage range. The contribution of interface states close to the Fermi energy are observed experimentally by both methods. Due to the particular behaviour of the differential conductivity with the bias voltage, it has been concluded that the presence of interface states and magnetic impurities can be the reason why it has not been possible to obtain a high TMR value.

Besides these limitations, for $Co_2MnGa$ good agreement of ARUPS and not spin polarized tunneling spectroscopy results with theoretically predicted DOS was observed.

# Appendix A

# General deposition parameters

## MgO buffer layer

- Deposition by electron beam evaporation in the MBE chamber
- Deposition temperature: 400°C
- Thickness: 100 Å
- Deposition rate: 0.5 Å/s
- Chamber pressure during deposition: 2x10$^{-7}$ mbar

## $Co_2FeAl_{0.3}Si_{0.7}$

- Deposition by magnetron rf sputtering in the sputtering chamber A
- Thickness: 303 Å
- Deposition time: 45 min
- Argon pressure: 0.1 mbar
- Power: 25 W / Voltage: 66 V
- Annealing after deposition*: 550°C (in MBE chamber), pressure around 1x10$^{-9}$ mbar

*The annealing temperature of this Heusler was modified to study disorder properties.

## $Co_2MnGa$

- Deposition by magnetron rf sputtering in the sputtering chamber B
- Thickness: 321 Å
- Deposition time: 18 min 31 s
- Argon pressure: 0.1 mbar
- Power: 25 W / Voltage: 93 V
- Annealing after deposition: 550ºC (in MBE chamber), pressure around $1x10^{-9}$ mbar

## Mg

- Deposition by magnetron rf sputtering in the sputtering chamber B
- Thickness[†]: between 2.5 to 7.5 Å
- Deposition time: between 2 s to 7 s
- Argon pressure: 0.05 mbar
- Power: 15 W / Voltage: 59 V

## Al

- Deposition by magnetron rf sputtering in the sputtering chamber B
- Thickness[‡]: between 10 to 22 Å
- Deposition time: between 4 min 17 s to 9 min 26 s
- Argon pressure: 0.05 mbar
- Power: 20 W / Voltage: 61 V

[†]The thickness of the Mg was modified to study its influence on TMR

[‡]The thickness of the tunneling barrier was modified depending on the Heusler to aim the best results concerning resistance, TMR and morphology.

## Al oxidation

- Plasma oxidation by Al oxidation cathode in the sputtering chamber B
- Oxidation time[§]: between 8 to 15 s
- Argon pressure: 0.1 mbar
- Oxygen pressure: 0.1 mbar
- Intensity: 10 mA / Voltage: 500 V

## CoFe

- Deposition by magnetron rf sputtering in the sputtering chamber A
- Thickness: 40 Å
- Deposition time: 3 min 26 s
- Argon pressure: 0.1 mbar
- Power: 25 W / Voltage: 54 V

## MnFe

- Deposition by magnetron rf sputtering in the sputtering chamber A
- Thickness: 150 Å
- Deposition time: 10 min
- Argon pressure: 0.1 mbar
- Power: 25 W / Voltage: 42 V

[§]The oxidation time was modified depending on the barrier thickness.

# Au

- Deposition by magnetron rf sputtering in the sputtering chamber A
- Thickness: 200 Å
- Deposition time: 2 min 15 s
- Argon pressure: 0.1 mbar
- Power: 20 W / Voltage: 75 V

# Appendix B

# Patterning of mesa structures

1. Sample cleaning on the spinner, with isopropanol for 15 s at 300 rpm and then 15 s at 4000 rpm for drying. This will remove particles from silver glue and dust that may be on the film. This process is repeated until no dust (or as little as possible) is observed under the microscope.

2. Cover with positive photoresist ma-P 1215 (micro resist technology GmbH), drop on at 300 rpm 10 s and then 30 s at 3000 rpm.

3. 90 s on the hot plate at 100 $^{o}$C.

4. 40 s UV exposure, mesa mask in contact.

5. Develop with maD-331, drop on without rotation and wait 45 s. Rinse with water for 15 s, 300 rpm and then 15 s, 4000 rpm for drying.

6. Ion etching: First, the sample is etched in an ion beam mixture between Argon and Oxygen in a 4/1 relation alternating between 86 and 50 degrees with respect to the sample surface every 2 minutes while the sample rotates during this process until the substrate of the reference sample is observed. Then, the etching is continued for additional 20 %.

7. Sample cleaning first with rm-Rem 660 developer and later with acetone in a ultrasonic bath, 2 min and 1 min, respectively.

8. After cleaning in the ultrasonic bath, wash the sample with acetone on the spinner for 15 s, 300 rpm and then dry for 15 s, 4000 rpm. The presence of particles must be checked with the microscope. If necessary repeat the acetone step until the sample is free of particles.

9. Cover with photoresist SU-8-2002. Then, spin 5 s at 500 rpm (acceleration factor 9) and 30 s at 3000 rpm.

10. Softbake of the resist on the hot plate. The sample must be heated up to 95 °C in 8 min. Hold for 1.5 min and then take it from the plate and let it cool down.

11. 40 s UV exposure, window mask in contact.

12. Post-exposure bake on the hot plate. The sample must be heated up to 95 °C in 6 min. Hold for 1 min and then take it from the plate and let it cool down.

13. Develop with XPSU-8, 75 s. Rinse with isopropanol, 15 s, 300 rpm and dry for 15 s at 4000 rpm.

14. Check under the microscope if the mesa structures are well prepared and if there are no particles.

# Appendix C

# Numerical calculation of dI/dV($V_{bias}$)

The MATHEMATICA program used for the numerical calculation of the tunneling current and the differential conductivity of a magnetic tunneling junction.

```
an = 10^ - 10;

(*Angström*)
me = 9.10910^ - 31; (*Kg; electronmass*)
hq = 1.0545710^ - 34; (*Js; hquerPlanckconstant*)
ec = 1.610^ - 19; (*C; electroncharge*)
(* Barrieren Height h and Thickness b*)
h1 = 2.75 * ec; h2 = 2.5 * ec; h3 = 2.5 * ec; h4 = 2.25 * ec;
b1 = 5.5 * an; b2 = 5.5 * an; b = b1 + b2;

(*Density of states as a gaussian function*)
(*First Gaussian*)
a1 = 0.15; (*DOS Maximum*)
e1 = 0.07 * ec; (*Energy width in eV*)
ep1 = -0.15 * ec; (*Position of the Gaussian*)
a2 = 0.35; e2 = 0.2 * ec; ep2 = -0.6 * ec; (*Second Gaussian*)
a3 = 0; e3 = 0.4 * ec; ep3 = -1.8 * ec; (*Third Gaussian*)

(*Density of states*)
```

```
dos[en_] = 1 + a1 * Exp[-((en - ep1)^2)/(2 * e1)^2]+
a2 * Exp[-((en - ep2)^2)/(2 * e2)^2]+
a3 * Exp[-((en - ep3)^2)/(2 * e3)^2];
Plot[dos[en], {en, -1 * ec, 1 * ec}]
Plot[dos[-en], {en, -1 * ec, 1 * ec}]

(*Right direction for the current*)
(* Potential barrier*)
bapot1[x_] = h1(UnitStep[x/b1] - UnitStep[x/b1 - 1])+
(h2 - h1)(UnitStep[x/b1] - UnitStep[x/b1 - 1])x/b1+
h3(UnitStep[(x - b1)/b2] - UnitStep[(x - b1)/b2 - 1])+
(h4 - h3)(UnitStep[(x - b1)/b2] - UnitStep[(x - b1)/b2 - 1])(x - b1)/b2;
Plot[bapot1[x], {x, -b, b}]
(* Barrier deformed through a bias voltage ev*)
biasba1[x_, ev_] = bapot1[x] - (UnitStep[x/b] - UnitStep[x/b - 1])(x/b)ev * ec;
Plot[biasba1[x, 0.5], {x, -b, b}]
(*Tunnelingprobability, replaced1/hqund1me*)
tprob1[en_, ev_] = Exp[-(2/hq)NIntegrate[(2me(biasba1[x, ev] - en))^0.5, {x, 0, b}]];
tcurrent1[ev_] = NIntegrate[tprob1[en, ev] * dos[-en], {en, -ev * ec, 0}];

(*Left direction for the current*)
(* Potential barrier*)
bapot2[x_] = (h4(UnitStep[x/b2] - UnitStep[x/b2 - 1])+
(h3 - h4)(UnitStep[x/b2] - UnitStep[x/b2 - 1])(x/b2)+
h2(UnitStep[(x - b2)/b1] - UnitStep[(x - b2)/b1 - 1])+
(h1 - h2)(UnitStep[(x - b2)/b1] - UnitStep[(x - b2)/b1 - 1])((x - b2)/b1));
Plot[bapot2[x], {x, -b, b}]
(* Barrier deformed through a bias voltage ev*)
biasba2[x_, ev_] = bapot2[x] - (UnitStep[x/b] - UnitStep[x/b - 1])(x/b)ev * ec;
Plot[biasba2[x, 0.5], {x, -10 * an, 60 * an}]
(*Tunnelingprobability, replaced1/hqund1me*)
tprob2[en_, ev_] = Exp[-(2/hq)NIntegrate[(2me(biasba2[x, ev] - en))^0.5, {x, 0, b}]];
(*Tunneling current*)
tcurrent2[ev_] = NIntegrate[tprob2[en, ev] * dos[en], {en, -ev * ec, 0}];

(*Open data right direction*)
```

```
OpenWrite["u:\Tunneling1.dat"]
(*Savedata; differentialconductivity*)
Do[Write["u:\Tunneling1.dat", tcurrent1'[ev]], {ev, 0, 1, 0.01}]
Close["u:\Tunneling1.dat"]
FilePrint["u:\Tunneling1.dat"]

(*Open data left direction*)
OpenWrite["u:\Tunneling2.dat"]
(*Savedata; differentialconductivity*)
Do[Write["u:\Tunneling2.dat", tcurrent2'[ev]], {ev, 0, 1, 0.01}]
Close["u:\Tunneling2.dat"]
FilePrint["u:\Tunneling2.dat"]
```

# Bibliography


[1] M. N. Baibich, J. M. Broto, A. Fert, F. N. V. Dau, F. Petroff, P. Etienne, G. Creuzet, A. Friederich, and J. Chazelas,*Phys. Rev. Lett.*, **61**, 2472 (1988).

[2] G. Binasch, P. Grünberg, F. Saurenbach, and W. Zinn, *Phys. Rev. B*, **39**, 4828 (1989).

[3] P. M. Tedrow, and M. Meservey, *Phys. Rev. Lett.*, **26**, 192 (1971).

[4] M. Jullière, *Phys. Lett.*, **54A**, 225 (1975).

[5] B. Dieny, V. S. Speriosu, S. Metin, S. S. P. Parkin, B. A. Gurney, P. Baumgart, and D. R. Wilhoit., *J. App. Phys.*, **69**, 4774 (1991).

[6] J. S. Moodera, L. R. Kinder, T. M. Wong, and R. Meservey, *Phys. Rev. Lett.*, **74**, 3273 (1995).

[7] T. Miyazaki, and N. Tezuka, *J. Magn. Magn. Mater.*, **139**, 231 (1995).

[8] J. M. Daughton, Thin Solid Films, **216**, 162 (1992).

[9] W. C. Black Jr, and B. Das., *J. App. Phys.*, **87**, 6674 (2000).

[10] A. Ney, C. Pampuch, R. Koch, and K. Ploog., *Nature*, **418**, 509 (2002).

[11] T. Jungwirth, J. Sinova, J. Masěc, J. Kučera, and A. H. MacDonald, *Rev. Mod. Phys.*, **78**, 809 (2006).

[12] M. I. Katsnelson, V. Yu. Irkhin, L. Chioncel, A. I. Lichtenstein, and R. A. de Groot, *Rev. Mod. Phys.*, **80**, 315 (2008).

[13] S. Ishida, T. Masaki, S. Fujii, and S. Asano, *Physica B*, **245**, 1 (1998).

[14] A. Ayuela, J. Enkovaara, K. Ullakko, and R. M. Nieminen,*J. Phys.: Condens. Matter*, **11**, 2017 (1999).

[15] I. Galanakis, and P. H. Dederichs, *Phys. Rev. B*, **66**, 134428 (2002).

[16] H. F. Kino, F. Aryasetiawanb, I. Solovyevc, T. Miyaked, T. Ohnoa, K. Terakurab, *Physica B*, **329**, 858 (2003).

[17] K. E. H. M. Hanssen, and P. E. Mijnarends, *Phys. Rev. B*, **34**, 5009 (1986).

[18] S. Okamura, A. Miyazaki, and S. Sugimoto, N. Tezuka, K. Inomata, *App. Phys. Lett.*, **86**, 232503 (2005).

[19] Y. Sakuraba, J. Nakata, M. Oogane, Y. Ando, H. Kato, A. Sakuma, T. Miyazaki, and H. Kubota, *App. Phys. Lett.*, **88**, 022503 (2006).

[20] B. S. D. Ch. S. Varaprasad, A. Rajanikanth, Y. K. Takahashi, and K. Hono, *Acta Materialia*, **57**, 2702 (2009).

[21] Y. K. Takahashi, A. Srinivasan, B. Varaprasad, A. Rajanikanth, N. Hase, T. M. Nakatani, S. Kasai, T. Furubayashi, and K. Hono, *App. Phys. Lett.*, **98**, 152501 (2011).

[22] J. Y. T. Wei, N.-C. Yeh, and R. P. Vasquez, *Phys. Rev. Lett.*, **79**, 5150 (1997).

[23] J.-H. Park, E. Vescovo, H.-J. Kim, C. Kwon, R. Ramesh, and T. Venkatesan, *Nature*, **392**, 794 (1998).

[24] K. P. Kämper, W. Schmitt, G. Guntherodt, R. J. Gambino, and R. Ruf, *Phys. Rev. Lett.*, **59**, 2788 (1987).

[25] M. Cinchetti, J.-P. Wüstenberg, M. Sánchez Albaneda, F. Steeb, A. Conca, M. Jourdan, and M. Aeschlimann, *J. Phys. D: Appl. Phys.*, **40**, 1544 (2007).

[26] R. Bertacco, M. Portalupi, M. Marcon, L. Duò, F. Ciccacci, M. Bowen, J.P. Contour, A. Barthélémy, *J. Magn. Magn. Mat.*, **242**, 710 (2002).

[27] I. Galanakis, and Ph. Mavropoulos, *J. Phys.: Condens. Matter*, **19**, 315213 (2007).

[28] V. Yu. Irkhin, M. I. Katsnelson, and A. I. Lichtenstein, *J. Phys.: Condens. Matter*, **19**, 315201 (2007).

[29] I. Galanakis, *J. Phys.: Condens. Matter*, **14**, 6329 (2002).

[30] S.J. Jenkins, and D.A. King, *Surf. Science*, **501**, 185 (2002).

[31] A. Sakuma, Y. Toga, and H. Tsuchiura, *J. App. Phys.*, **105**, 07C910 (2009).

[32] K. Capelle, *Braz. J. Phys.*, **36**, nº. 4A, (2006).

[33] P. Fulde, "Correlations in Molecules and Solids", *3 ed. Springer* (1995).

[34] J. P. Perdew and S. Kurth, "Density Functionals for Non-relativistic Coulomb Systems in the New Century", Free Online Books.
*URL: http://training.nigc.ir/files/files/chemist book 5/Physical Chemistry/Quantum chemistry/Density Functional Theory/density functional theoryJohn P. Perdew.pdf.*

[35] R. Dreizler, "Relativistic Density Functional Theory", Free Online Books.
*URL: http://training.nigc.ir/files/files/chemist book 5/Physical Chemistry/Quantum chemistry/Density Functional Theory/density functional theoryJohn P. Perdew.pdf.*

[36] P. Hohenberg and W. Kohn, *Phys. Rev.*, **136**, B864 (1964).

[37] W. Kohn and L. J. Sham, *Phys. Rev.*, **140**, A1133 (1965).

[38] R. D. Meade, A. M. Rappe, K. D. Brommer, J. D. Joannopoulos, and O. L. Alerhand, *Phys. Rev. B*, **48**, 8434 (1993).

[39] http://www.ece.nus.edu.sg/stfpage/eleadj/planewave.htm

[40] R. Haydock, V. Heine, and M. J. Kelly, *J. Phys. C: Solid State Phys.*, **8**, 2591 (1975).

[41] A. Zunger and A. J. Freeman, *Phys. Rev. B*, **15**, 4716 (1977).

[42] C. Herring, *Phys. Rev.*, **57**, 1169 (1940).

[43] R. S. Leigh, *Proc. Phys. Soc. A*, **69**, 388 (1956).

[44] P. Mavropoulos and N. Papanikolaou, "The Korringa-Kohn-Rostoker (KKR) Green Function Method *I. Electronic Structure of Periodic Systems*", published in Computational Nanoscience: Do It Yourself!, J. Grotendorst, S. Blügel, D. Marx (Eds.), John von Neumann Institute for Computing, Julich, NIC Series, Vol. 31, ISBN 3-00-017350-1, pp. 131-158, 2006.

[45] O. K. Andersen, *Phys. Rev. B*, **12**, 3060 (1975).

[46] E. H. Lieb, *Rev. Mod. Phys.* , **53**, 603 (1981).

[47] M. Levy and J. P. Perdew, *Phys. Rev. A*, **32**, 2010 (1985).

[48] V. I. Anisimovy, F. Aryasetiawanz, and A. I. Lichtenstein, *J. Phys.: Condens. Matter*, **9**, 767 (1997).

[49] J. Hubbard, *Prec. Roy. Soc. (London)*, **A276**, 238 (1963).

[50] A. Georges, G. Kotliar, W. Krauth, and M. J. Rozenberg, *Rev. Mod. Phys.*, **68**, 13 (1996).

[51] K. Held, I. A. Nekrasov, G. Keller, V. Eyert, N. Blümer, A. K. McMahan, R. T. Scalettar, T. Pruschke, V. I. Anisimov, and D. Vollhardt, *arXiv:cond-mat/0112079v1 [cond-mat.str-el]* (2001).

[52] G. Kotliar, D. Vollhardt, "Strongly Correlated Materials: Insights From Dynamical Mean-Field Theory", *Physics today*, 53 (2004).

[53] J. P. Perdew and W. Yue, *Phys. Rev. B*, **33**, 8800 (1986).

[54] J. P. Perdew, K. Burke, M. Ernzerhof, *Phys. Rev. Lett.*, **77**, 3865 (1996).

[55] A. D. Becke, J. Chem. Phys., 98, 7 (1993).

[56] J. P. Perdew, S. Kurth, A. Zupan, P. Blaha, *Phys. Rev. Lett.*, **82**, 2544 (1999); E. Ibid **82**, 5179 (1999).

[57] J. P. Perdew, A. Zunger, *Phys. Rev. B*, **23**, 5048 (1981).

[58] J. B. Krieger, Y. Li, and G. J. Iafrate, *Phys. Rev. A*, **45**, 101 (1992).

[59] E. Engel and S. H. Vosko, *Phys. Rev. A*, **47**, 2800 (1993).

[60] K. Held, *Advances in Physics*, **56**, 829 (2007).

[61] L. Chioncel, L. Vitos, I. A. Abrikosov, J. Kollár, M. I. Katsnelson, and A. I. Lichtenstein, *Phys. Rev. B*, **67**, 235106 (2003).

[62] F. Heusler, *Verh. Deutsch. Phys. Ges.*, **5**, 219 (1903).

[63] http://www.nims.go.jp/apfim/halfmetal.html

[64] R. A. de Groot, F. M. Mueller, P. G. van Engen, and K. H. J. Buschow, *Phys. Rev. Lett.*, **50**, 2024 (1983).

[65] S. Ishida, S.Fujii, S. Kashiwagi, S. Asano, *J. Phys. Soc. Jap.*, **64**, 2152 (1995).

[66] J. Tobołla, and J. Pierre, *J. All. Comp.*, **296**, 243 (2000).

[67] Y. Miura, K. Nagao, and M. Shirai, *Phys. Rev. B*, **69**, 144413 (2004).

[68] K. Schwarz, *J. Phys. F: Met. Phys.*, **16**, L211 (1986).

[69] W. E. Pickett and D. J. Singh, *Phys. Rev. B*, **53**, 1146 (1996).

[70] M. Shirai, T. Ogawa, I. Kitagawa, N. Suzuki, *J. Magn. Magn. Mat.*, **177**, 1383 (1998).

[71] L. Chioncel, M. I. Katsnelson, R. A. de Groot, and A. I. Lichtenstein, *Phys. Rev. B*, **68**, 144425 (2003).

[72] V. Yu. Irkhin, M. I. Katsnelson, and A. I. Lichtenstein, *J. Phys.: Condens. Matter*, **19**, 315201 (2007).

[73] V. Yu. Irkhin and M. I. Katsnelson, *Eur. Phys. J. B.*, **43**, 479 (2005).

[74] L. Chioncel, Y. Sakuraba, E. Arrigoni, M. I. Katsnelson, M. Oogane, Y. Ando, T. Miyazaki, E. Burzo, and A. I. Lichtenstein, *Phys. Rev. Lett.*, **100**, 086402 (2008).

[75] L. Chioncel, E. Arrigoni, M. I. Katsnelson, and A. I. Lichtenstein, *Phys. Rev. Lett.*, **96**, 137203 (2006).

[76] P. Klaer, E. Arbelo Jorge, M. Jourdan, W. H. Wang, H. Sukegawa, K. Inomata, and H. J. Elmers, *Phys. Rev. B*, **82**, 024418 (2010).

[77] S. Fujii, S. Sugimura, S. Ishida, and S. Asano, **J. Phys.: Condens. Matter**, **2**, 8583 (1990).

[78] H. C. Kandpal, G. H. Fecher and C. Felser, *J. Phys. D: Appl. Phys.*, **40**, 1507 (2007).

[79] S. Fujii, S. Ishida, and S. Asano, *J. Phys. Soc. Jpn.*, **64**, 185 (1995).

[80] I. Galanakis and P. H. Dederichs, *Phys. Rev. B*, **66**, 174429 (2002).

[81] I. Galanakis, Ph. Mavropoulos and P. H. Dederichs, *J. Phys. D: Appl. Phys.*, **39**, 765 (2006).

[82] http://www.riken.jp/lab-www/nanomag/research/heusler_e.html

[83] J. C. Slater, *Phys. Rev.*, **49**, 537 (1936).

[84] L. Pauling, *Phys. Rev.*, **54**, 899 (1938).

[85] G. H. Fecher and C.Felser, *J. Phys. D: Appl. Phys.*, **40**, 1582 (2007).

[86] S. Picozzi, A. Continenza, and A. J. Freeman, *Phys. Rev. B*, **66**, 094421 (2002).

[87] S. Kämmerer, A. Thomas, A. Hütten, and G. Reiss, *Appl. Phys. Lett.*, **85**, 79 (2004).

[88] Y. Sakuraba, M. Hattori, M. Oogane, Y. Ando, H. Kato, A. Sakuma, T. Miyazaki, H. Kubota, *Appl. Phys. Lett*, **88**, 192508 (2006).

[89] M. Jourdan, E. Arbelo Jorge, C. Herbort, M. Kallmayer, P. Klaer, H. J. Elmers, *Appl. Phys. Lett*, **95**, 172504 (2009).

[90] Ph. Mavropoulos, K. Sato, R. Zeller, P. H. Dederichs, V. Popescu, and H. Ebert, *Phys. Rev. B*, **69**, 054424 (2004).

[91] Ph. Mavropoulos, I. Galanakis, V. Popescu, and P. H. Dederichs, J. Phys.: Condens. Matter, **16**, S5759 (2004).

[92] Z. Gercsi and K. Hono, *J. Phys.: Condens. Matter*, **19**, 326216 (2007).

[93] K. Özdoğan, E. Şaşoğlu, B. Aktaş, and I. Galanakis, *Phys. Rev. B*, **74**, 172412 (2006).

[94] A. Vedyayev, N. Ryzhanova, R. Vlutters, and B. Dieny, *Europhys. Lett.*, **46**, 808 (1999).

[95] K. E. H. M. Hanssen and P. E. Mijnarends, *Phys. Rev. B*, **34**, 5009 (1986).

[96] K. E. H. M. Hanssen, P. E. Mijnarends, L. P. L. M. Rabou, and K. H. J. Buschow, *Phys. Rev. B*, **42**, 1533 (1990).

[97] www.positronannihilation.net

[98] B. Feuerbacher and R. F. Willis, *J. Phys. C: Solid State Phys.*, **9**, 169 (1976).

[99] S. Hüfner: *Photoelectron Spectroscopy - Principles and Applications.* Third Edition, Springer (2003).

[100] P. D. Johnson, *Rep. Prog. Phys.*, **60**, 1217 (1997).

[101] J. B. Pendry, *Phys. Rev. Lett.*, **45**, 1356 (1980).

[102] J. Unguris, A. Seiler, R. J. Celotta, D. T. Pierre, P. D. Johnson and N. V. Smith, *Phys. Rev. Lett.*, **49**, 1047 (1982).

[103] G. Onida, L. Reining, A. Rubio, *Rev. Mod. Phys.*, **74**, 601 (2002).

[104] R. J. Soulen Jr, J. M. Byers, M. S. Osofsky, B. Nadgorny, T. Ambrose, S. F. Cheng, P. R. Broussard, C. T. Tanaka, J. Nowak, J. S. Moodera, A. Barry, and J. M. D. Coey, *Science*, **282**, 85 (1998).

[105] G. J. Strijkers, Y. Ji, F. Y. Yang, C. L. Chien, and J. M. Byers, *Phys. Rev. B*, **63**, 104510 (2001).

[106] C. Jurecka, *"Punktkontaktspectroscopie zur Bestimmung magnetischer und supraleitender Eigenschaften von Festkörpern"*, **Diplomarbeit**, Johannes Gutenberg Universität, Mainz (2007).

[107] R. M. Feenstra, *Surface Science*, **299/300**, 965 (1994).

[108] C. Herbort, Dissertation: *"Tunnelkontakte mit Heusler-Elektrode: Spinpolarisation von $Co_2Cr_{0.6}Fe_{0.4}Al$ und Einfluss der Barriere"*, Johannes Gutenberg University Mainz, (2010).

[109] N. N. Ledentsov (ed.), *"Growth Processes and Surface Phase Equilibria in Molecular Beam Epitaxy"*, STMP **156**, Springer (1999).

[110] http://wwwold.ece.utep.edu/research/webedl/cdte/Fabrication/index.htm

[111] M. Ziese and M. J. Thornton (eds), *"Spin Electronics"*, LNP **569**, Springer (2001).

[112] R. Behrisch and W. Eckstein (eds.), *"Sputtering by Particle bombardment"*, TAP **110**, Springer (1981).

[113] http://www.arzuffisrl.it/eng/images/sputtering1.jpg

[114] H. Zabel and S. D. Bader (eds), *"Magnetic Heterostructures"*, STMP **227**, Springer (2008).

[115] W. Braun, Applied RHEED, *"Reflection High-Energy Electron Difraction During Crystal Growth"*, STMP **154**, Springer (1999).

[116] M. A. Van Hove, W. H. Weinberg, and C. M. Chan, *"Low-Energy Electron Diffraction"*, SSSS **6**, Springer (1986).

[117] N. W. Ashcroft and N. D. Mermin, *"Solid State Physics"*, (Harcourt Brace & Company), $1^{st}$ edition (1976).

[118] A. Guinier, *"X-Ray Diffraction in Crystals, Imperfect Crystals, and Amorphous Bodies"*, Dover Publications, New York (1994).

[119] P. J. Webster, Contemp. Phys., 10, 559 (1969).

[120] V. Holý, U. Pietsch, and T. Baumbach (eds.), *"High-Resolution X-Ray Scattering from Thin Films and Multilayers"*, STMP **149**, Springer (1999).

[121] J. Brentano, *Proc. Phys. Soc. London*, **37**, 184 (1924).

[122] P. Colombi, D. K. Agnihotri, V. E. Asadchikov, E. Bontempi, D. K. Bowen, C. H. Chang, L. E. Depero, M. Farnworth, T. Fujimoto, A. Gibaud, M. Jergel, M. Krumrey, T. A. Lafford, A. Lamperti, T. Ma, R. J. Matyi, M. Meduna, S. Milita, K. Sakurai, L. Shabel'nikov, A. Ulyanenkov, A. Van der Lees, and C. Wiemert, *J. Phys. Cryst.*, **41**, 143 (2008).

[123] C. Braun, Parrat32 Software for reflectivity, HMI Berlin (1999).

[124] M. Jourdan, A. Zakharov, A. Hiess, T. Charlton, N. Bernhoeft, and D. Mannix, *Eur. Phys. J. B*, **48**, 445 (2005).

[125] Description and download of the Powder-Cell program in the webpage of the Bundesanstalt für Materialforschung und Prüfung Berlin: http://www.bam.de/de/service/publikationen/powder-cell.htm.

[126] S. Foner, *Rev. Sci. Inst.*, **30**, 548 (1959).

[127] N. W. Aschcroft and N. D. Mermin, *"Solid State Physics"*. International Edition (1976).

[128] J- Stöhr, *J. Magn. Magn. Mat*, **200**, 470, (1999).

[129] K. Urban, C. M. Schneider, T. Brückel, S. Blügel, K. Tillmann, W. Schweika, M. Lentzen, and L. Baumgarten (eds), *"Probing the Nanoworld"*, Lecture Manuscripts of the **38th** Spring School 2007.

[130] W. Kuch, *"Abbildende magnetische Mikrospektroscopie, Habilitation"*, Martin-Luther-Universität Halle-Wittenberg (2002).

[131] B. T. Thole, P. Carra, F. Sette, and G. van der Laan, *Phys. Rev. Lett.*, **68**, 1943 (1992).

[132] P. Carra, B. T. Thole, M. Altarelli, and X. Wang, *Phys. Rev. Lett*, **70**, 694 (1993).

[133] H. J. Elmers, G. H. Fecher, D. Valdaitsev, S. A. Nepijko, A. Gloskovskii, G. Jakob, and G. Schönhense, *Phys. Rev. B*, **67**, 104412 (2003).

[134] M. Kallmayer, H. Schneider, G. Jakob, H. J. Elmers, B. Balke, and S. Cramm, *J. Phys. D: Appl. Phys.*, **40**, 1552 (2007).

[135] M. Kallmayer, P. Klaer, H. Schneider, G. Jakob, H. J. Elmers, D. Legut, and P. M. Oppeneer, *Phys. Rev. B*, **84**, 054448 (2011).

[136] http://en.wikipedia.org/wiki/Photoemission_spectroscopy

[137] C. N. Berglund, W. E. Spicer, *Phys. Rev. A*, **13**6, 1030 and 1044 (1964).

[138] M. P. Seah and W. Dench, *"Surface and Interface analysis"*, Vol. **1(1)** (1979).

[139] G. D. Mahan, *Phys. Rev.*, **163**, 612 (1967).

[140] S. Wurmehl, G. H. Fecher, K. Kroth, F. Kronast, H. A Dürr, Y. Takeda, Y. Saitoh, K. Kobayashi, H-J. Lin, G. Schönhense, and C. Felser, *J. Phys. D: Appl. Phys.*, **39**, 803 (2006).

[141] H. Miyazaki, K. Soda, M. Kato, S. Yagi, T. Takeuchi, and Y. Nishino, *J. Electron Spectrosc. Relat. Phenom.*, **347**, 156 (2007).

[142] S. Imada, A. Yamasaki, K. Kusuda, A. Higashiya, A. Irizawa, A. Sekiyama, T. Kanomatae, and S. Suga, *J. Electron Spectrosc. Relat. Phenom.*, **433**, 156 (2007).

[143] J. S. Correa, C. Eibl, G. Rangelov, J. Braun, and M. Donath, *Phys. Rev. B*, **73**, 125316 (2006).

[144] K. Miyamoto, A. Kimura, Y. Miura, M. Shirai, M. Ye, Y. Cui, K. Shimada, H. Namatame, M. Taniguchi, Y. Takeda, Y. Saitoh, E. Ikenaga, S. Ueda, K. Kobayashi, and T. Kanomata, *Phys. Rev. B*, **79**, 100405 (2009).

[145] S. Ouardi, B. Balke, A. Gloskovskii, G. H. Fecher, C. Felser, G. Schönhense, T. Ishikawa, T. Uemura, M. Yamamoto, H. Sukegawa, W. Wang, K. Inomata, Y. Yamashita, H. Yoshikawa, S. Ueda, and K. Kobayashi, *J. Phys. D: Appl. Phys.*, **42**, 084010 (2009).

[146] W. H. Wang, M. Przybylski, W. Kuch, L. I. Chelaru, J. Wang, Y. F. Lu, J. Barthel, H. L. Meyerheim, and J. Kirschner, *Phys. Rev. B*, **71**, 144416 (2005).

[147] M. Jourdan, F. Grosse-Schulte, M. Hahn, and G. Schönhense, *J. Phys. D: Appl. Phys.*, **44**, 155001 (2011).

[148] F. Grosse-Schulte, Diplomarbeit: *"Untersuchung der elektronischen Eigenschaften von Heusler-Verbindungen mit Ultraviolett-Photoelektronen-Spektroskopie"*, Johannes Gutenberg Universität Mainz (2010).

[149] M. Hahn, G. Schönhense, E. Arbelo Jorge, and M. Jourdan, *Appl. Phys. Lett.*, **98**, 232503 (2011).

[150] J. J. Yeh and I. Lindau, *At. Data Nucl. Data Tables*, **32**, 1 (1985).

[151] M. Jourdan and M. Kolbe, *Private communication*, (September 2011).

[152] R. Meservey, and P. M. Tedrow, *Phys. Rev. Lett.*, **25**, 1270 (1970).

[153] P. M. Tedrow, and R. Meservey, *Phys. Rev. Lett.*, **26**, 192 (1971).

[154] J. Bardeen, *Phys. Rev. Lett.*, **6**, 57 (1961).

[155] E. Yu. Tsymbal, and D. G. Pettifor, *Phys. Rev. B*, **58**, 432 (1998).

[156] Y. Sakuraba, M. Hattori, M. Oogane, Y. Ando, H. Kato, A. Sakuma, and T. Miyazaki, *App. Phys. Lett.*, **88**, 192508 (2006).

[157] N. Tezuka, N. Ikeda, A. Miyazaki, S. Sugimoto, M. Kikuchi, and K. Inomata, *App. Phys. Lett.*, **89**, 112514 (2006).

[158] N. Tezuka, N. Ikeda, S. Sugimoto, and K. Inomata, *Jap. J. App. Phys. Part 2 & Exp. Lett.*, **46**, L454 (2007).

[159] J. Schmalhorst, D. Ebke, M. D. Sacher, N. N. Liu, A. Thomas, G. Reiss, A. Hutten, E. Arenholz, *IEEE Trans. Magn.*, **43**, 2806 (2007).

[160] D. Wang, C. Nordman, J. M. Daughton, Z. Qian, and J. Fink, IEEE Trans. Magn., 40, 2269 (2004).

[161] S. Ikeda, J. Hayakawa, Y. Ashizawa, Y. M. Lee, K. Miura, H. Hasegawa, M. Tsunoda, F. Matsukura, and H. Ohno, App. Phys. Lett., 93, 082508 (2008).

[162] C. Herbort, E. Arbelo Jorge, and M. Jourdan, *App. Phys. Lett*, **94**, 142504 (2009).

[163] V. Heine, *Phys. Rev.*, **138**, A1689 (1965).

[164] Ph. Mavropoulos, N. Papanikolaou, and P. H. Dederichs, *Phys. Rev. Lett.*, **85**, 1088 (2000).

[165] P. H. Dederichs, Ph. Mavropoulos, O. Wunnicke, N. Papanikolaou, V. Bellini, R. Zeller, V. Drchal, and J. Kudrnovský, *J. Magn. Magn. Mat.*, **240**, 108 (2002).

[166] J.M. MacLaren, X.-G. Zhang, W.H. Butler, and X. Wang, *Phys. Rev. B*, **59**, 5470 (1999).

[167] J. Mathon, and A. Umerski, *Phys. Rev. B*, **63**, 220403 (2001).

[168] E. Y. Tsymbal, K. D. Belashchenko, J. P. Velev, S. Jaswal, M. van Schilfgaarde, I. I. Oleynik, and D. A. Stewart, *Prog. Mat. Science*, **52**, 401 (2007).

[169] J. S. Moodera, M. E. Taylor, and R. Meservey, Phys. Rev. B, 40, 11980 (1989).

[170] J. J. Sun, and P. P. Freitas, J. Appl. Phys., 85, 5264 (1999).

[171] P. LeClair, H. J. M. Swagten, J. T. Kohlhepp, R. J. M. van de Veerdonk, and W. J. M. de Jonge, *Phys. Rev. Lett*, **84**, 2933 (2000).

[172] L. Nèel, *Comptes-rendus de l'Académie des Sciences*, A122:521 (1963).

[173] F. Guinea, *Phys. Rev. B*, **58**, 9212 (1998).

[174] R. Jansen and J. S. Moodera, *J. App. Phys.*, **83**, 6682 (1998).

[175] J. A. Appelbaum and W. F. Brinkman, *Phys. Rev.*, **183**, 553 (1969).

[176] A. H. Davis and J. M. MacLaren, *J. App. Phys.*, **87**, 5224 (2000).

[177] W. A. Harrison, *Phys. Rev.*, **123**, 85 (1961).

[178] J. G. Simmons, *J. App. Phys.*, **34**, 1793 (1963).

[179] W. F. Brinkman, R. C. Dynes, and J. M. Rowell, *J. App. Phys.*, **41**, 1915 (1970).

[180] B. Oliver, Q. He, X. Tang, and J. Nowak, *J. App. Phys.*, **91**, 4348 (2002).

[181] C. Shang, Y. Chen, and K. Moon, *J. App. Phys.*, **93**, 7017 (2003).

[182] http://en.wikipedia.org/wiki/File:ScanningTunnelingMicroscope_schematic.png

[183] A. Conca, PhD Thesis: *"Magnetic Tunneling Junctions with the Heusler compound* $Co_2Cr_{0.6}Fe_{0.4}Al$*"*, Johannes Gutenberg Universität Mainz (2007).

[184] J. Nogués, and I. K. Schuller, *J. Magn. Magn. Mat.*, **192**, 203 (1999).

[185] M. D. Stiles, and R. D. McMichael, *Phys. Rev. B*, **60**, 12950 (1999).

[186] T. C. Schulthess, and W. H. Butler, *Phys. Rev. Lett.*, **81**, 4516 (1998).

[187] E. Burstein and S. Lundquist, *"Tunneling Phenomena in Solids"*, Plenum New York (1969).

[188] B. Oliver, Q. He, X. Tang, and J. Nowak, *J. App. Phys.*, **94**, 1783 (2003).

[189] J. J. Åkerman, J. M. Slaughter, R. W. Dave, and I. K. Schuller, *App. Phys. Lett*, **79**, 3104 (2001).

[190] C. H. Shang, J. Nowak, R. Jansen, and J. S. Moodera, *Phys. Rev. B*, **58**, R2917 (1998).

[191] L. I. Glazman and K. A. Matveev, *Zh. Eksp. Teor. Fiz.*, **94**, 332 (1998) [*Sov. Phys. Semicond.*, **22**, 401 (1988)]; N. F. Mott, *Philos. Mag.*, **19**, 835 (1969).

[192] D. J. Monsma, and S. S. P. Parkin, *Appl. Phys. Lett.*, **77**, 720 (2000).

[193] J. J. Hauser and L. R. Testardi, *App. Phys. Lett.*, **20**, 12 (1968).

[194] J. S. Moodera, J. Nassar, and G. Mathon, *Annu. Rev. Sci.*, **29**, 381 (1999).

[195] X. H. Xiang, T. Zhu, J. Du, G. Landry, and J. Q. Xiao, *Phys. Rev. B*, **66**, 174407 (2002).

[196] X. H. Xiang, T. Zhu, G. Landry, J. Du, , Y. Zhao, and J. Q. Xiao, *Appl. Phys. Lett.*, **83**, 2826 (2003).

[197] Ph. Mavropoulos, M. Ležaić, S. Blügel, *Phys. Rev. B*, **72**, 174428 (2005).

[198] X-F. Han, A. C. C. Yu, M. Oogane, J. Murai, T. Daibou, and T. Miyazaki, *Phys. Rev. B*, **63**, 224404 (2001).

[199] V. Y. Irkhin, M. I. Katsnelson, *Phys. Rev. B*, **73**, 104429 (2006).

[200] S. Picozzi, A. Continenza, and A. J. Freeman, *J. Phys. Chem. Solids*, **64**, 1697 (2003).

[201] I. Galanakis, M. Ležaić, Gustav Bihlmayer, and Stefan Blügel, *Phys. Rev. B*, **71**, 214431 (2005).

[202] G. A. de Wijs and R. A. de Groot, *Phys. Rev. B*, **64**, 020402(R) (2001).

# Acknowledgement

First, I would like to thank my tutor XXX for giving me the opportunity to join this group and work on this researching project. I am very grateful to him for his good leading, patience, advise and help, and for the fruitful cooperation and discussions.
I thank all my colleagues for giving a hand every time it was needed and for the good times we also spent together, not only during work, but also during our spare time.
Furthermore, I would also like to thank the members of external groups whose collaboration was of great importance to make this work possible. In particular, to XXX, XXX and XXX for their collaboration with XMCD measurements and the nice time we spent together working at BESSY. To XXX and XXX for their knowledge, advice and help with photoemission spectroscopy technique.
Enormous thanks goes to XXX and XXX for their great job with the maintenance of the laboratories and technical devices, and for their help with technical problems.
Special gratitude goes to my family and friends who, although they did not take direct part on this work, they support me unconditionally.

# List of publications

1. P. Haro González, I. R. Martín, E. Arbelo Jorge, S. González Pérez, J. M. Cáceres, and P. Núñez:
   *Laser irradiation in $Nd^{3+}$ doped strontium barium niobate glass*
   Journal of Applied Physics **104**, 013112 (2008).

2. M. Jourdan, E. Arbelo Jorge, C. Herbort, M. Kallmayer, P. Klaer, and H. J. Elmers:
   *Interface and bulk magnetism of $Co_2Cr_{0.6}Fe_{0.4}Al$ and $Co_2CrAl$ thin films*
   Applied Physics Letters **95**, 172504 (2009).

3. O. Gaier, J. Hamrle, S, Trudel, A. Conca Parra, B. Hillebrands, E. Arbelo, C. Herbort, and M. Jourdan:
   *Brillouin light scattering study of $Co_2Cr_{0.6}Fe_{0.4}Al$ and $Co_2FeAl$ Heusler compounds*
   Journal of Physics D: Applied Physics **42**, 084004 (2009).

4. C. Herbort, E. Arbelo, and M. Jourdan:
   *Morphology and magnetoresistance of $Co_2Cr_{0.6}Fe_{0.4}$ Al-based tunnelling junctions*
   Journal of Physics D: Applied Physics **42**, 084006 (2009).

5. C. Herbort, E. Arbelo Jorge, and M. Jourdan:
   *Morphology induced magnetoresistance enhancement of tunneling junctions with the Heusler electrode $Co_2Cr_{0.6}Fe_{0.4}Al$*
   Applied Physic Letters **94**, 142504 (2009).

6. M. Kallmayer, P. Klaer, H. Schneider, E. Arbelo Jorge, C. Herbort, G. Jakob, M. Jourdan, and H. J. Elmers:
*Spin-resolved unoccupied density of states in epitaxial Heusler-alloy films*
Physical Review B **80**, 020406R (2009).

7. E. Arbelo Jorge, M. Jourdan, M. Kallmayer, P. Klaer, and H. J. Elmers:
*Magnetic and structural properties of $Co_2FeAl_{1-x}Si_x$ thin films*
chapter Journal of Physics: Conference Series **200**, 072006 (2010).

8. P. Klaer, E. Arbelo Jorge, M. Jourdan, W. H. Wang, H. Sukegawa, K. Inomata, and H. J. Elmers:
*Temperature dependence of X-ray absorption spectra in the ferromagnetic Heusler alloys $Mn_2VAl$ and $Co_2FeAl$*
Physical Review B **82**, 024418 (2010).

9. M. Hahn, G. Schönhense, E. Arbelo Jorge, and M. Jourdan:
*Significant spin polarization of $Co_2MnGa$ Heusler thin films on MgO (100) measured by ultraviolet photoemission spectroscopy*
Applied Physics Letters **98**, 232503 (2011).

10. P. Klaer, F. Hoffmann, G. Woltersdorf, E. Arbelo Jorge, M. Jourdan, C. H. Back and H. J. Elmers:
*Element-specific ferromagnetic resonance in epitaxial Heusler spin valve systems*
Journal of Physics D: Applied Physics **44**, 425004 (2011).